Development of Photo- and Thermo-Induced Mechanical Crystals

光と熱によって動くメカニカル結晶の創製

February 2019

Takuya TANIGUCHI

谷口卓也

Development of Photo- and Thermo-Induced Mechanical Crystals

光と熱によって動くメカニカル結晶の創製

February 2019

Waseda University

Graduate School of Advanced Science and Engineering

Department of Advanced Science and Engineering

Research on Life Science and Medical Bioscience

Takuya TANIGUCHI

谷口卓也

Contents

Chapter 1

General Introduction

1.1 Mechanical motion of materials

1.1.1 The importance of motion

The conversion of energy into mechanical motion has essential roles in nature. All living organisms use energy to grow, move, and locomote for their reproduction and survival. The human being has developed various systems to create motion such as steam engine, combustion engine, hydraulic pump, and electromagnetic motor. The evolution of these mechanical systems always coincides with the industrial revolution, which has changed how to live a human life.

1.1.2 Actuation materials

With the progress of material science, the human has developed metal and ceramic materials that can deform responding to external stimuli. For example, shape memory alloys are well known to recover their own shape from deformed shape by heating to their transition temperature. Piezoelectric materials convert alternating current voltage into oscillation, which is utilized in our watches. Besides them, thermal expansion, electrostriction, and magnetostriction and so on are utilized to actuate materials.

Owing to the development of chemistry, nanotechnology, and analytical technique, organic actuation materials are being developed based on molecular-level understanding. Organic materials are generally softer, lighter, and cheaper than inorganic materials. Thus, mechanically responsive organic materials are expected as next-generation smart actuators. The prospects of future application include sensing, optics, data storage, bio-tissues, aerospace, drug delivery, mechanical devices, soft robotics, automotive, tactile devices, printers, valves, active catheters, and so on.[1]

1.2 Mechanically responsive polymers and gels

1.2.1 Photo-responsive polymers and gels

Photomechanical polymers have been well developed by crosslinking main chain with photochromic compounds.[2–4] The typical photochromic compound is azobenzene, which undergoes *trans–cis* photoisomerization and back-isomerization reversibly. The photoreaction occurs most on the irradiated surface and decreases according to the penetration depth of the light. The molecular shape changes due to photochromic reaction form bilayer-like structure, inducing macroscopic motion such as bending, twisting, and helicoidal motion of the photo-responsive polymers (Figure 1.1).

Another useful material is gels, which is generally much softer than polymers due to the existence of solvents. Photo-responsive gels are also able to deform due to molecular shape change via photoisomerization.[5,6]

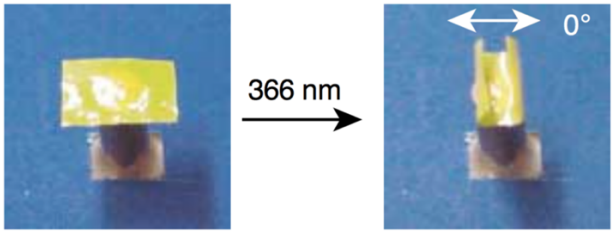

Figure 1.1 Photomechanical bending of an azobenzene-containing polymer film by a polarized light. Reprinted in part from Yu, Y., Nakano, M. Ikeda, T. Directed bending of a polymer film by light. *Nature* **425**, 145 (2003).[2] Copyright 2003 Springer Nature.

1.2.2 Thermo-responsive polymers

Thermo-responsive polymers mostly utilize shape memory effect.[7–9] Shape memory polymers actuate responding to temperature change (Figure 1.2). The actuation mechanism is based on the change of elasticity due to the glass transition of cross-linked polymers. Shape memory polymers

become much softer due to the decrease of elasticity above the glass transition temperature. Once the polymers are deformed at a temperature higher than the glass transition temperature, the deformed shape is maintained after cooling. The deformed polymers return to the initial shape upon next heating up to the glass transition temperature. Thus, thermomechanical motion can be achieved by shape recovery effect by temperature change.

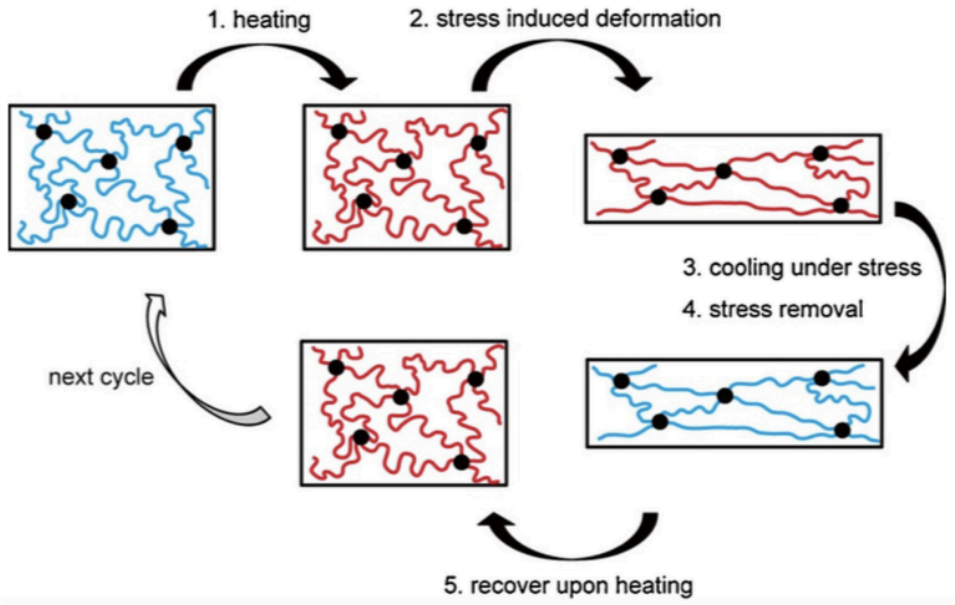

Figure 1.2 Schematic illustration of actuation mechanism of a shape memory polymer. Reprinted in part from Zhao, Q., Qi, H. J., Xie, T. Recent progress in shape memory polymer: New behavior, enabling materials, and mechanistic understanding. *Prog. Polym. Sci.* **49**, 79–120 (2015).[9] Copyright 2015 Elsevier.

1.2.3 Other external stimuli

Active polymers and gels responding to other external stimuli such as humidity, voltage, and magnetic field have also been researched and developed extensively by many research groups.[10–15] The actuation mechanisms are based on adsorption/desorption of molecules, mass transportation, piezoelectricity, electro-/magneto-striction, and so on.

1.3 Mechanically responsive crystals

1.3.1 Photomechanical crystals

In spite of their appearance of solid and fragile features, molecular crystals have been constructing a foundation of mechanically responsive materials in the past decade. An epoch-making report was that a diarylethene crystal deformed upon UV light irradiation and returned by visible light due to a reversible photochromic reaction (Figure 1.3).[16] The actuation mechanism is similar to photo-responsive polymers. Photoisomerization undergoes most at the irradiated surface, and decreases depending on light penetration depth. Due to the generated stress of photoproducts, the crystal can deform. The report broke up the established concept that molecular crystals cannot deform due to their own solid but fragile features. Following the publication, typical photoreactive crystals such as diarylethene, anthracene, azobenzene (the bending is shown in Figure 1.4), and so on as shown in Figure 1.5 have exhibited several types of motion such as bending,[16–36] twisting,[37–40] rotation,[41] and hopping.[42,43] Recent advances on photomechanical crystals are reviewed in several publications.[44–49]

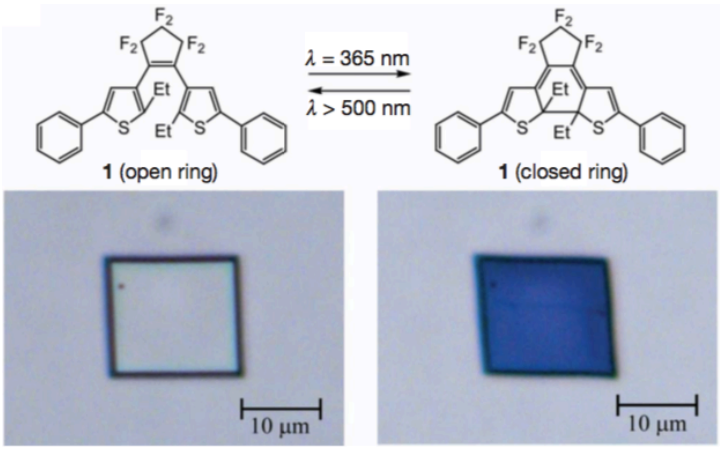

Figure 1.3 Photoinduced shape change of a diarylethene crystal. Reprinted from Kobatake, S., Takami, S., Muto, H., Ishikawa, T., Irie, M. Rapid and reversible shape changes of molecular crystals on photoirradiation. *Nature* **446**, 778–781 (2007).[16] Copyright 2007 Springer Nature.

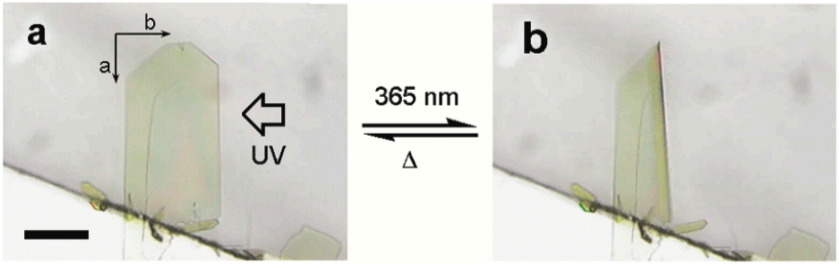

Figure 1.4 Photomechanical bending of a 4-dimethylaminoazobenzene crystal. Reprinted with permission from Koshima, H., Ojima, N., Uchimoto, H. Mechanical motion of azobenzene crystals upon photoirradiation. *J. Am. Chem. Soc.* **131**, 6890–6891 (2009).[18] Copyright 2009 American Chemical Society.

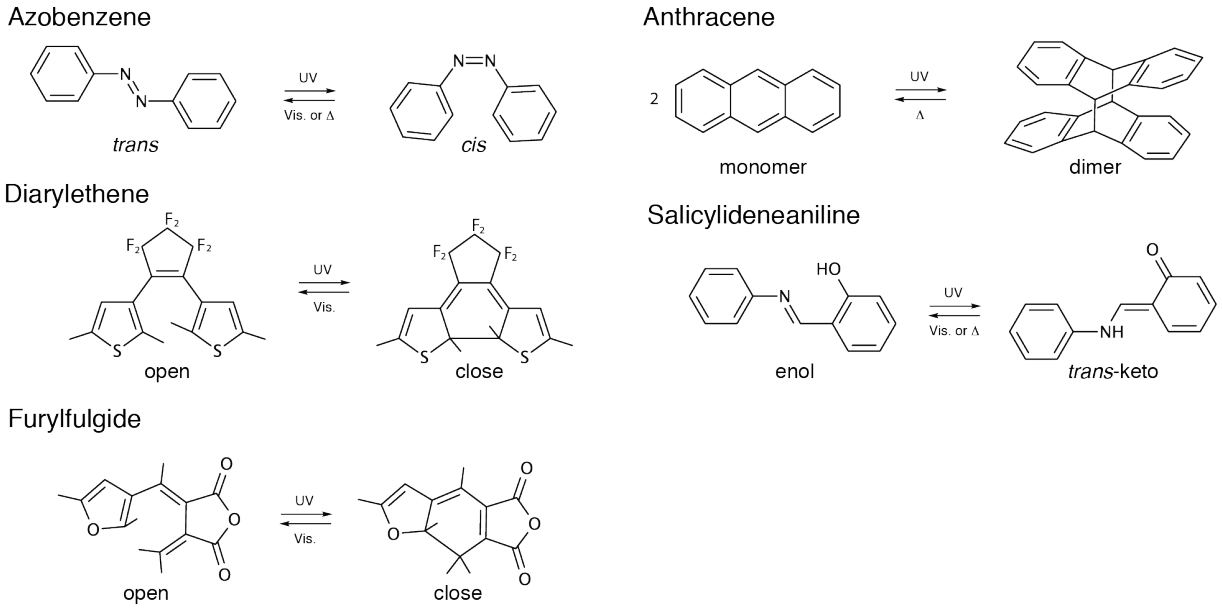

Figure 1.5 Typical photochromic reactions to achieve photomechanical motion.

1.3.2 Structural phase transition

A structural phase transition is a type of phase transition undergoing in the solid state, in most cases, induced by temperature change. The crystals deform without any disintegration due to the

similarity of crystal structures before and after the structural phase transition (Figure 1.6). The structural phase transition is a relatively rare phenomenon because the manifestation of the phase transition is unpredictable even for the current computational chemistry. In spite of the difficulty to find the structural phase transition, various kinds of molecular crystals have been reported to exhibit structural phase transition, inducing mechanical motion such as bending,[50,51] expansion/contraction,[52–58] and jumping.[59–60]

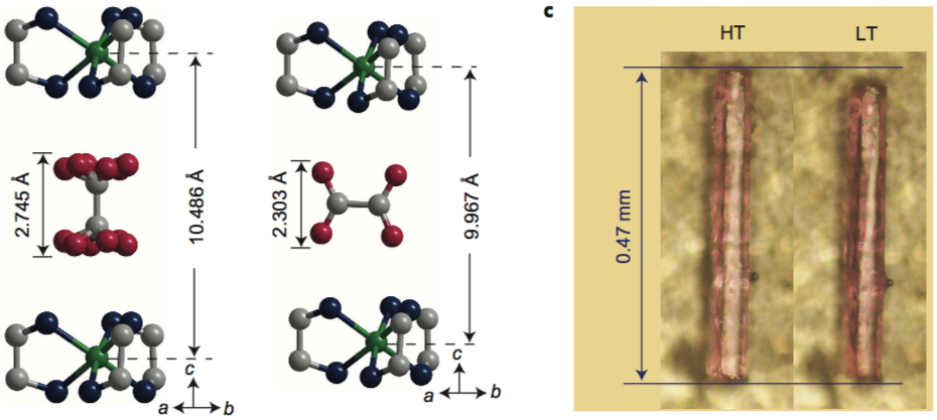

Figure 1.6 Crystal deformation induced by molecular reorientation. Reprinted with permission from Yao, Z. S., Mito, M., Kamachi, T., Shiota, Y., Yoshizawa, K., Azuma, N., Miyazaki, Y., Takahashi, K., Zhang, K., Nakanishi, T., Kang, S., Kanegawa, S., Sato, O. Molecular motor-driven abrupt anisotropic shape change in a single crystal of a Ni complex. *Nat. Chem.* **6**, 1079–1083 (2014).[52] Copyright 2014 Springer Nature.

1.3.3 Elastic and plastic deformation

Besides photo- and thermo-responsive crystals, molecular crystals can bend elastically by manually applying stress.[61–63] Elastic bending occurs due to expansion on a convex side and compression on a concave side of the bending through slight displacements of molecules (Figure

1.7). The elastic bending returns to the initial shape by excluding the applied stress. The elastic property of crystals is characterized by Young's modulus and strain.

Some crystals can bend plastically (Figure 1.7).[64–66] The plastic bending occurs due to sliding of molecular layers along the bending and rehabilitation of intermolecular interactions between layers. Therefore, plastic bending does not change the length of convex and concave sides, and the angle of the crystal edge decreases from the initial angle.

Recently, superelastic and ferroelastic molecular crystals have attracted attention beyond known bending properties of molecular crystals.[67–73] These crystals deform by manually applying shear stress accompanied with the creation of new crystal phase or twin domain. Superelasticity is termed when the new domain spontaneously returns to the initial domain, and ferroelasticity is used when the new domain maintains even after excluding shear stress. Thus, deformable crystals with plasticity, superelasticity, and ferroelasticity are a candidate of damping materials rather than actuation materials.

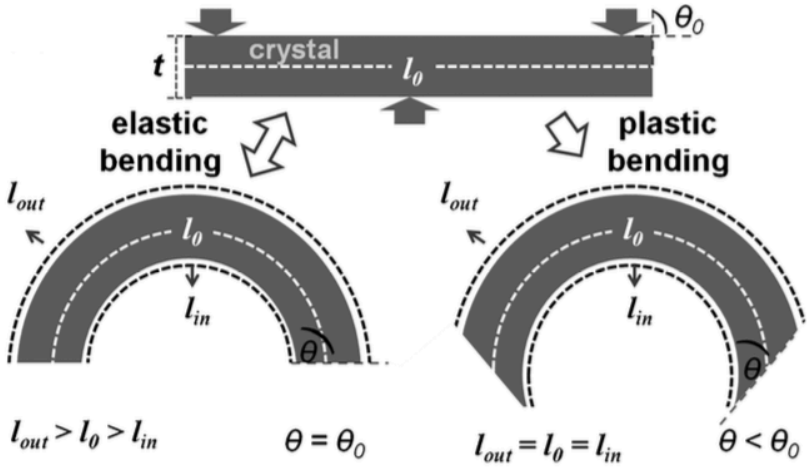

Figure 1.7 Schematic representation of elastic and plastic bending by three points bending. Reprinted with permission from Ghosh, S., Reddy, C. M. Elastic and bendable caffeine cocrystals: implications for the design of flexible organic materials. *Angew. Chem. Int. Ed.* **51**, 10319–10323 (2012).[61] Copyright 2012 John Wiley and Sons.

1.4 Mechanical properties

1.4.1 Young's modulus and strain

Materials are evaluated with several mechanical properties: Young's modulus (elastic modulus), strain, maximum stress, force, speed of response, reversibility, energy efficiency, displacement, and type of motion *i.e.* expansion, contraction, bending, twisting, and so on (Figure 1.8). In addition, applications to some devices require other specifications such as cost, ease of processing, environmental effects, and integration with current technologies. The required mechanical properties and specifications depend on the targeted application.

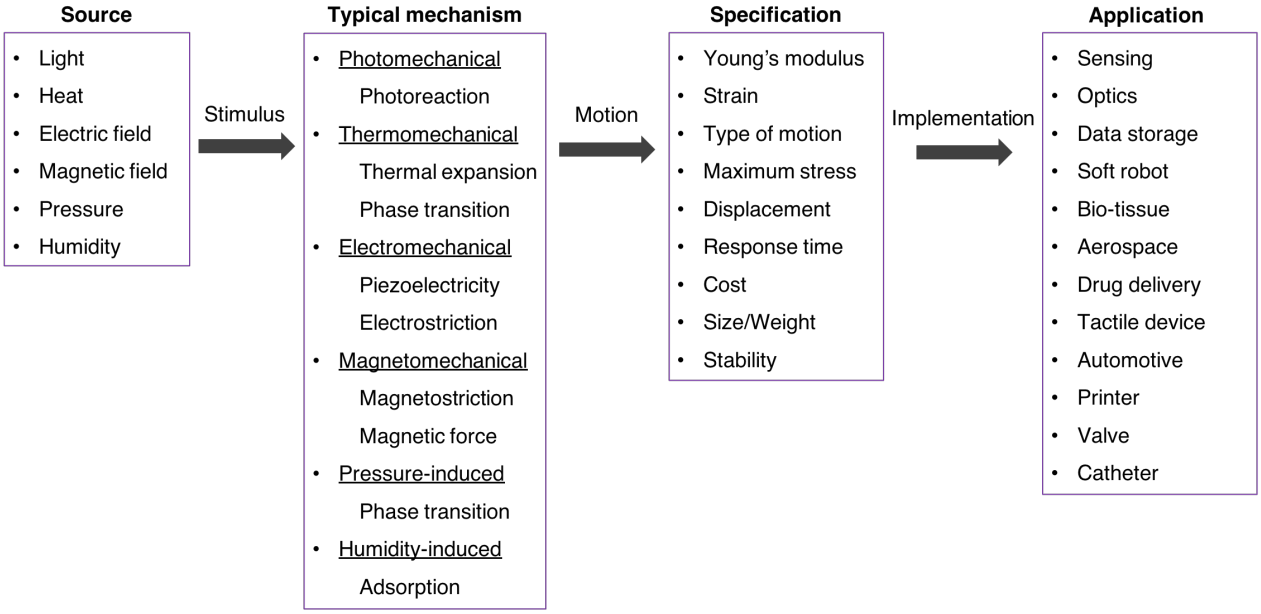

Figure 1.8 Scheme and lists of typical actuation mechanism, specification, and possible application.

Among mechanical properties, Young's modulus and strain are fundamental material-specific properties to correlate between motion and force of actuation materials. Strain (ε) indicates

the amplitude of motion of a given material. On the other hand, Young's modulus (E) determines the magnitude of applied force to achieve the strain. These two values are correlated with the volume work density $W/V = E\varepsilon^2/2$, that is, the maximum mechanical work output per unit volume of the actuation material. For example, a large force with a small displacement can be obtained from a piezoelectric material. In contrast, a large displacement by a small load is expected from polymers and gels.

In the case of bending motion, maximum force F can be calculated from Young's modulus E and deflection δ (equivalent to strain ε) according to the following equation.

$$F = \frac{3\delta EI}{l^3}$$

Here, l is the length of material, and I $(= bh^3/12)$ is the moment of inertia (b: width, h: thickness of the material). Thus, when a material size is defined, a material with larger Young's modulus and deflection generates higher maximum force at the actuation.

1.4.2 Location of molecular crystals

Strain and Young's modulus of actuation materials including molecular crystals is shown in Figure 1.9. Metals and alloys actuating by thermal expansion, piezoelectricity, magnetostriction, and shape memory effect have relatively large Young's modulus in the range of 10–500 GPa. The strain of these materials ranges 0.01–10%.

Mechanically responsive polymers are typically located on smaller Young's modulus of 1–100 MPa and larger strain, sometimes more than 100%. The mechanical properties of polymers are the most similar to those of human skeletal muscle. In the case of gels, the Young's modulus is much smaller (~50 kPa) than that of polymers. Rubbers also have small Young's modulus (~100 kPa) comparable with gels and soft polymers.

Photo- and thermo-mechanical molecular crystals generally have the Young's modulus of 1–10 GPa and the strain of 0.1–1%. The mechanical property of mechanically responsive molecular crystals is located between metallic inorganic materials and organic polymers with respect to Young's modulus and strain. This location indicates that mechanically responsive molecular crystals fill the gap between inorganic materials and organic polymers and that have the potential to broaden new applications in the future. This character is the motivation to develop new mechanically responsive crystals.

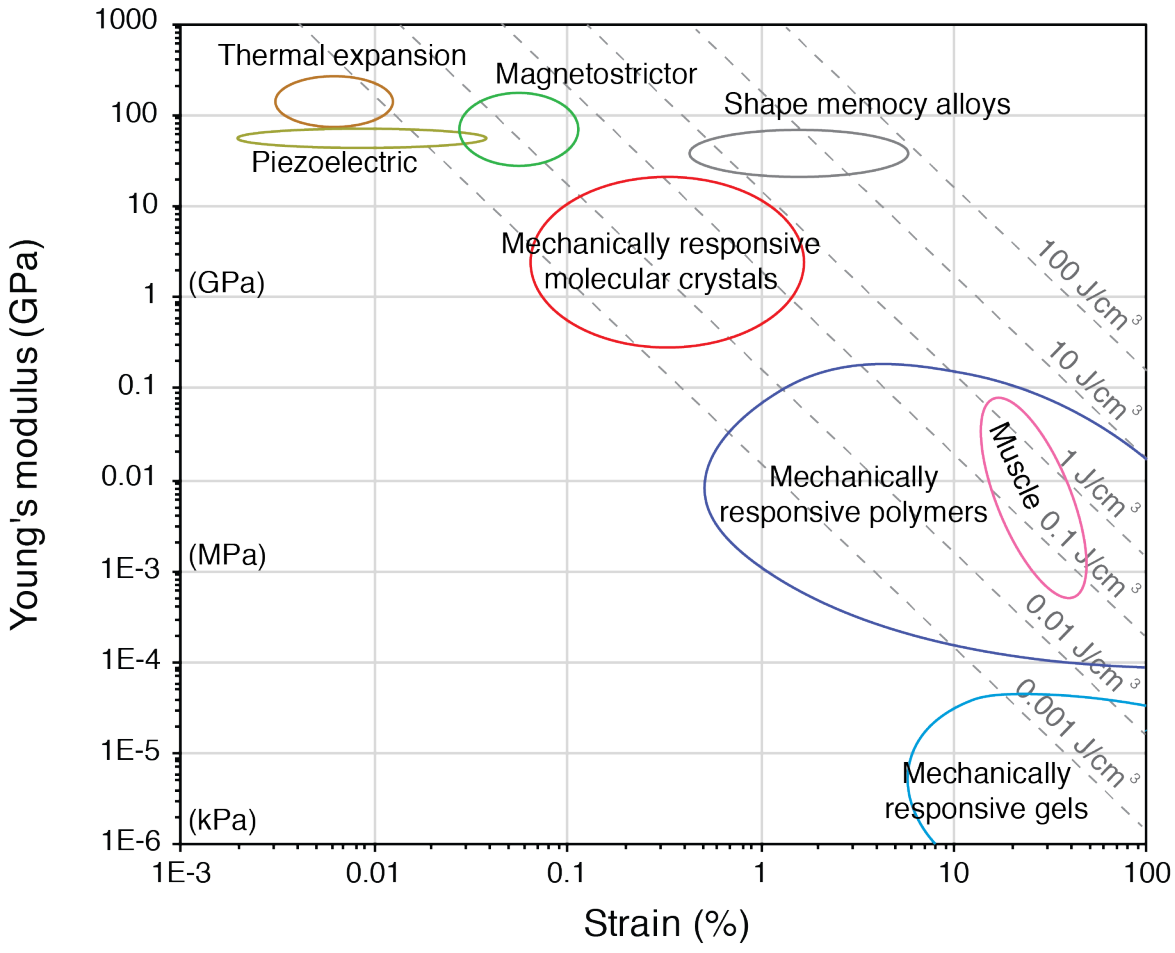

Figure 1.9 Relationship between Young's modulus and strain of actuation materials.[1] Dashed lines indicate the contours of equal volumetric work density W/V.

1.5 Scope of this thesis

This doctoral thesis composed of 5 chapters focuses on the development of photo- and thermo-mechanical crystals. In chapter 1, I have introduced the history and mechanical properties of mechanically responsive materials. The position and the potential of molecular crystals are clarified by comparing mechanical properties with other actuation materials.

In chapter 2, I describe photomechanical bending with a twisting of chiral azobenzene crystals. The chiral azobenzene is designed based on the concept of electron-donor substituent and chiral induction. Thin crystals of the compound bend with a small twist upon photoirradiation. The bending behavior is explained based on photochromic behavior, crystal structure before irradiation, and molecular conformation change obtained by theoretical calculation.

In chapter 3, I describe walking and rolling locomotion of chiral azobenzene crystals induced by a structural phase transition. The phase transition occurs at 145 °C reversibly, and crystals bend at the transition temperature. The bending motion leads to a walking or rolling locomotion depending on crystal shape. The locomotion mechanism is elucidated by careful observation of locomotion, and temperature measurements by thermography camera.

In chapter 4, I describe photo-triggered phase transition and stepwise bending. The photo-triggered phase transition is unexpectedly discovered in a photochromic crystal, which exhibits thermal structural phase transition near room temperature. The photo-triggered phase transition achieves unique molecular conformation, which cannot be achieved by heating. The photo-triggered phase transition broadens the ability of photomechanical crystal; thin crystals bend in stepwise only by light irradiation.

In chapter 5, I summarize this thesis and mention future prospects of mechanically responsive molecular crystals.

1.6 References

1. Manrique-Juarez, M. D., Rat, S., Salmon, L., Molnár, G., Quintero, C. M., Nicu, L., Shepherd, H. J., Bousseksou, A. Switchable molecule-based materials for micro-and nanoscale actuating applications: achievements and prospects. *Coord. Chem. Rev.* **308**, 395–408 (2016).
2. Yu, Y., Nakano, M., Ikeda, T. Directed bending of a polymer film by light. *Nature* **425**, 145 (2003).
3. Ikeda, T., Mamiya, J., Yu, Y. Photomechanics of liquid - crystalline elastomers and other polymers. *Angew. Chem. Int. Ed.* **46**, 506−528 (2007).
4. Wei, J., Yu, Y. Photodeformable polymer gels and crosslinked liquid-crystalline polymers. *Soft Matter* **8**, 8050–8059 (2012).
5. Takashima, Y., Hatanaka, S., Otsubo, M., Nakahata, M., Kakuta, T., Hashidzume, A., Yamaguchi, H., Harada, A. Expansion-contraction of photoresponsive artificial muscle regulated by host-guest interactions. *Nat. Commun.* **3**, 1270 (2012).
6. Iwaso, K., Takashima, Y., Harada, A. Fast response dry-type artificial molecular muscles with [c2]daisy chains. *Nat. Chem*. **8**, 625–632 (2016).
7. Lendlein, A., Kelch, S. Shape-memory polymers. *Angew. Chem. Int. Ed.* **41**, 2034−2057 (2002).
8. Liu, C., Qin, H., Mather, P. T. Review of progress in shape-memory polymers. *J. Mater. Chem.* **17**, 1543–1558 (2007).
9. Zhao, Q., Qi, H. J., Xie, T. Recent progress in shape memory polymer: new behavior, enabling materials, and mechanistic understanding. *Prog. Polym. Sci.* **49**, 79–120 (2015).
10. Osada, Y., Okuzaki, H., Hori, H. A polymer gel with electrically driven motility. *Nature* **355**, 242–244 (1992).

11. Fukushima, T., Asaka, K., Kosaka, A., Aida, T. Fully plastic actuator through layer-by-layer casting with ionic-liquid-based bucky gel. *Angew. Chem. Int. Ed.* **44**, 2410−2413 (2005).

12. Zhang, L., Liang, H., Jacob, J., Naumov, P. Photogated humidity-driven motility. *Nat. Commun.* **6**, 7429 (2015).

13. Arazoe, H., Miyajima, D., Akaike, K., Araoka, F., Sato, E., Hikima, T., Kawamoto, M., Aida, T. An autonomous actuator driven by fluctuations in ambient humidity. *Nat. Mater*. **15**, 1084–1089 (2016).

14. Hu, W., Lum, G. Z., Mastrangeli, M., Sitti, M. Small-scale soft-bodied robot with multimodal locomotion. *Nature* **554**, 81–85 (2018).

15. Kim, Y., Yuk, H., Zhao, R., Chester, S. A., Zhao, X. Printing ferromagnetic domains for untethered fast-transforming soft materials. *Nature* **558**, 274–279 (2018).

16. Kobatake, S., Takami, S., Muto, H., Ishikawa, T., Irie, M. Rapid and reversible shape changes of molecular crystals on photoirradiation. *Nature* **446**, 778–781 (2007).

17. Morimoto, M., Irie, M. A diarylethene cocrystal that converts light into mechanical work. *J. Am. Chem. Soc.* **132**, 14172–14178 (2010).

18. Terao, F., Morimoto, M., Irie, M. Light-driven molecular-crystal actuators: rapid and reversible bending of rodlike mixed crystals of diarylethene derivatives. *Angew. Chem. Int. Ed.* **51**, 901−904 (2012).

19. Al-Kaysi, R. O., Bardeen, C. J. Reversible photoinduced shape changes of crystalline organic nanorods. *Adv. Mater.* **19**, 1276−1280 (2007).

20. Kim, T., Al-Muhanna, M. K., Al-Suwaidan, S. D., Al-Kaysi, R. O., Bardeen, C. J. Photoinduced curling of organic molecular crystal nanowires. *Angew. Chem. Int. Ed.* **52**, 6889−6893 (2013).

21. Kitagawa, D., Kobatake, S. Crystal thickness dependence of the photoinduced crystal bending of 1-(5-methyl-2-(4-(*p*-vinylbenzoyloxymethyl) phenyl)-4-thiazolyl)-2-(5-methyl-2-phenyl-4-thiazolyl) perfluorocyclopentene. *Photochem. Photobiol. Sci.* **13**, 764–769 (2014).

22. Kitagawa, D., Tanaka, R., Kobatake, S. Dependence of photoinduced bending behavior of diarylethene crystals on irradiation wavelength of ultraviolet light. *Phys. Chem. Chem. Phys.* **17**, 27300–27305 (2015).

23. Koshima, H., Ojima, N., Uchimoto, H. Mechanical motion of azobenzene crystals upon photoirradiation. *J. Am. Chem. Soc.* **131**, 6890–6891 (2009).

24. Koshima, H., Takechi, K., Uchimoto, H., Shiro, M., Hashizume, D. Photomechanical bending of salicylideneaniline crystals. *Chem. Commun.* **47**, 11423–11425 (2011).

25. Koshima, H., Ojima, N. Photomechanical bending of 4-aminoazobenzene crystals. *Dyes Pigm.* **92**, 798–801 (2012).

26. Koshima, H., Nakaya, H., Uchimoto, H., Ojima, N. Photomechanical motion of furylfulgide crystals. *Chem. Lett.* **41**, 107–109 (2012).

27. Koshima, H., Matsuo, R., Matsudomi, M., Uemura, Y., Shiro, M. Light-driven bending crystals of salicylidenephenylethylamines in enantiomeric and racemic forms. *Cryst. Growth Des.* **13**, 4330–4337 (2013).

28. Koshima, H., Uchimoto, H., Taniguchi, T., Nakamura, J., Asahi, T., Asahi, T. Mechanical motion of molecular crystals induced by [4+4] photodimerisation. *CrystEngComm.* **18**, 7305–7310 (2016).

29. Taniguchi, T., Kubota, A., Moritoki, T., Asahi, T., Koshima, H. Two-step photomechanical motion of a dibenzobarrelene crystal. *RSC Adv*. **8**, 34314–34320 (2018).

30. Naumov, P., Kowalik, J., Solntsev, K. M., Baldridge, A., Moon, J. S., Kranz, C., Tolbert, L.

M. Topochemistry and photomechanical effects in crystals of green fluorescent protein-like chromophores: effects of hydrogen bonding and crystal packing. *J. Am. Chem. Soc*. **132**, 5845–5857 (2010).

31. Nath, N. K., Pejov, L., Nichols, S. M., Hu, C., Saleh, N. I., Kahr, B., Naumov, P. Model for photoinduced bending of slender molecular crystals. *J. Am. Chem. Soc*. **136**, 2757–2766 (2014).
32. Chizhik, S., Sidelnikov, A., Zakharov, B., Naumov, P., Boldyreva, E. Quantification of photoinduced bending of dynamic molecular crystals: from macroscopic strain to kinetic constants and activation energies. *Chem. Sci*. **9**, 2319–2335 (2018).
33. Bushuyev, O. S., Tomberg, A., Vinden, J. R., Moitessier, N., Barrett, C. J., Friščić, T. Azo··· phenyl stacking: a persistent self-assembly motif guides the assembly of fluorinated *cis*-azobenzenes into photo-mechanical needle crystals. *Chem. Commun.* **52**, 2103–2106 (2016).
34. Bushuyev, O. S., Singleton, T. A., Barrett, C. J. Fast, reversible, and general photomechanical motion in single crystals of various azo compounds using visible light. *Adv. Mater.* **25**, 1796–1800 (2013).
35. Matsunaga, Y., Goto, K., Kubono, K., Sako, K., Shinmyozu, T. Photoinduced color change and photomechanical effect of naphthalene diimides bearing alkylamine moieties in the solid state. *Chem. Eur. J.* **20**, 7309–7316 (2014).
36. Cheng, S. C., Chen, K. J., Suzaki, Y., Tsuchido, Y., Kuo, T. S., Osakada, K., Horie, M. Reversible laser-induced bending of pseudorotaxane crystals. *J. Am. Chem. Soc.* **140**, 90–93 (2017).
37. Zhu, L., Al-Kaysi, R. O., Bardeen, C. J. Reversible photoinduced twisting of molecular crystal microribbons. *J. Am. Chem. Soc.* **133**, 12569–12575 (2011).

38. Kim, T., Zhu, L., Mueller, L. J., Bardeen, C. J. Mechanism of photoinduced bending and twisting in crystalline microneedles and microribbons composed of 9-methylanthracene. *J. Am. Chem. Soc.* **136**, 6617–6625 (2014).

39. Kitagawa, D., Nishi, H., Kobatake, S. Photoinduced twisting of a photochromic diarylethene crystal. *Angew. Chem. Int. Ed.* **52**, 9320–9322 (2013).

40. Kitagawa, D., Tsujioka, H., Tong, F., Dong, X., Bardeen, C. J., Kobatake, S. Control of photomechanical crystal twisting by illumination direction. *J. Am. Chem. Soc.* **140**, 4208–4212 (2018).

41. Zhu, L., Al-Kaysi, R. O., Bardeen, C. J. Photoinduced ratchet-like rotational motion of branched molecular crystals. *Angew. Chem. Int. Ed.* **55**, 7073–7076 (2016).

42. Naumov, P., Sahoo, S. C., Zakharov, B. A., Boldyreva, E. V. Dynamic single crystals: kinematic analysis of photoinduced crystal jumping (the photosalient effect). *Angew. Chem. Int. Ed.* **52**, 9990–9995 (2013).

43. Seki, T., Sakurada, K., Muromoto, M., Ito, H. Photoinduced single-crystal-to-single-crystal phase transition and photosalient effect of a gold(I) isocyanide complex with shortening of intermolecular aurophilic bonds. *Chem. Sci.* **6**, 1491–1497 (2015).

44. Irie, M., Yokoyama, Y., Seki, T. (eds) *New Frontiers in Photochromism*. Ch. 1, 2 (Springer, Tokyo, 2013).

45. Irie, M., Fukaminato, T., Matsuda, K., Kobatake, S. Photochromism of diarylethene molecules and crystals: memories, switches, and actuators. *Chem. Rev.* **114**, 12174–12277 (2014).

46. Kim, T., Zhu, L., Al-Kaysi, R. O., Bardeen, C. J. Organic photomechanical materials. *ChemPhysChem* **15**, 400–414 (2014).

47. Naumov, P., Chizhik, S., Panda, M. K., Nath, N. K., Boldyreva, E. Mechanically responsive molecular crystals. *Chem. Rev.* **115**, 12440–12490 (2015).

48. Abendroth, J. M., Bushuyev, O. S., Weiss, P. S. & Barrett, C. J. Controlling motion at the nanoscale: rise of the molecular machines. *ACS Nano* **9**, 7746–7768 (2015).

49. Commins, P., Desta, I. T., Karothu, D. P., Panda, M. K., Naumov, P. Crystals on the move: mechanical effects in dynamic solids. *Chem. Commun.* **52**, 13941–13954 (2016).

50. Shima, T., Muraoka, T., Hoshino, N., Akutagawa, T., Kobayashi, Y., Kinbara, K. Thermally driven polymorphic transition prompting a naked-eye-detectable bending and straightening motion of single crystals. *Angew. Chem. Int. Ed.* **53**, 7173–7178 (2014).

51. Dharmarwardana, M., Welch, R. P., Kwon, S., Nguyen, V. K., McCandless, G. T., Omary, M. A., Gassensmith, J. J. Thermo-mechanically responsive crystalline organic cantilever. *Chem. Commun*. **53**, 9890–9893 (2017).

52. Yao, Z. S., Mito, M., Kamachi, T., Shiota, Y., Yoshizawa, K., Azuma, N., Miyazaki, Y., Takahashi, K., Zhang, K., Nakanishi, T., Kang, S., Kanegawa, S., Sato, O. Molecular motor-driven abrupt anisotropic shape change in a single crystal of a Ni complex. *Nat. Chem.* **6**, 1079–1083 (2014).

53. Horie, M., Suzaki, Y., Hashizume, D., Abe, T., Wu, T., Sassa, T., Hosokai, T., Osakada, K. Thermally-induced phase transition of pseudorotaxane crystals: changes in conformation and interaction of the molecules and optical properties of the crystals. *J. Am. Chem. Soc.* **134**, 17932–17944 (2012).

54. Liu, G., Liu, J., Liu, Y., Tao, X., Oriented single-crystal-to-single-crystal phase transition with drastic changes in the dimensions of crystals. *J. Am. Chem. Soc.* **136**, 590–593 (2014).

55. Minami, T., Sato, H., Matsumoto, S. Macroscopic crystalline deformation in an organic dye

during reversible phase transition caused by alkyl disorder. *CrystEngComm*. **20**, 2644–2647 (2018).

56. Centore, R., Causà, M. Translating microscopic molecular motion into macroscopic body motion: reversible self-reshaping in the solid state transition of an organic crystal. *Cryst. Growth Des.* **18**, 3535–3543 (2018).

57. Donoshita, M., Hayashi, M., Ikeda, R., Yoshida, Y., Morikawa, S., Sugimoto, K., Kitagawa, H. Drastic rearrangement of self-assembled hydrogen-bonded tapes in a molecular crystal. *Chem. Commun*. **54**, 8571–8574 (2018).

58. Sahoo, S. C., Panda, M. K., Nath, N. K., Naumov, P. Biomimetic crystalline actuators: structure–kinematic aspects of the self-actuation and motility of thermosalient crystals. *J. Am. Chem. Soc.* **135**, 12241–12251 (2013).

59. Panda, M. K., Runčevski, T., Sahoo, S. C., Belik, A. A., Nath, N. K., Dinnebier, R. E., Naumov, P. Colossal positive and negative thermal expansion and thermosalient effect in a pentamorphic organometallic martensite. *Nat. Commun*. **5**, 4811 (2014).

60. Panda, M. K., Runčevski, T., Husain, A., Dinnebier, R. E., Naumov, P. Perpetually self-propelling chiral single crystals. *J. Am. Chem. Soc.* **137**, 1895–1902 (2015).

61. Ghosh, S., Reddy, C. M. Elastic and bendable caffeine cocrystals: implications for the design of flexible organic materials. *Angew. Chem. Int. Ed.* **51**, 10319–10323 (2012).

62. Ghosh, S., Mishra, M. K., Kadambi, S. B., Ramamurty, U., Desiraju, G. R. Designing elastic organic crystals: highly flexible polyhalogenated *N*-benzylideneanilines. *Angew. Chem. Int. Ed.* **54**, 2674–2678 (2015).

63. Hayashi, S., Koizumi, T. Elastic organic crystals of a fluorescent π-conjugated molecule. *Angew. Chem. Int. Ed.* **55**, 2701–2704 (2016).

64. Reddy, C. M., Gundakaram, R. C., Basavoju, S., Kirchner, M. T., Padmanabhan, K. A., Desiraju, G. R. Structural basis for bending of organic crystals. *Chem. Commun*. **0**, 3945–3947 (2005).

65. Panda, M. K., Ghosh, S., Yasuda, N., Moriwaki, T., Mukherjee, G. D., Reddy, C. M., Naumov, P. Spatially resolved analysis of short-range structure perturbations in a plastically bent molecular crystal. *Nat. Chem*. **7**, 65–72 (2015).

66. Krishna, G. R., Devarapalli, R., Lal, G., Reddy, C. M. Mechanically flexible organic crystals achieved by introducing weak interactions in structure: supramolecular shape synthons. *J. Am. Chem. Soc.* **138**, 13561–13567 (2016).

67. Takamizawa, S., Miyamoto, Y. Superelastic organic crystals. *Angew. Chem. Int. Ed.* **53**, 6970–6973 (2014).

68. Takamizawa, S., Takasaki, Y. Superelastic shape recovery of mechanically twinned 3,5-difluorobenzoic acid crystals. *Angew. Chem. Int. Ed.* **54**, 4815−4817 (2015).

69. Takamizawa, S., Takasaki, Y. Shape-memory effect in an organosuperelastic crystal. *Chem. Sci.* **7**, 1527–1534 (2016).

70. Mir, S. H., Takasaki, Y., Engel, E. R., Takamizawa, S. Ferroelasticity in an organic crystal: a macroscopic and molecular level study. *Angew. Chem. Int. Ed.* **56**, 15882–15885 (2017).

71. Mir, S. H., Takasaki, Y., Takamizawa, S. An organoferroelasticity driven by molecular conformational change. *Phys. Chem. Chem. Phys.* **20**, 4631–4635 (2018).

72. Engel, E. R., Takamizawa, S. Versatile ferroelastic deformability in an organic single crystal by twinning about a molecular zone axis. *Angew. Chem. Int. Ed.* **57**, 11888–11892 (2018).

73. Takamizawa, S., Takasaki, Y., Sasaki, T., Ozaki, N. Superplasticity in an organic crystal. *Nat. Commun.* **9**, 3984 (2018).

Chapter 2

Photomechanical bending with twisting

2.1 Introduction

As described in chapter 1, photomechanical crystals have the potential to find new applications because such crystals convert light energy into mechanical motion directly. Although dozens of photomechanical crystals have been developed in the past decade, the photomechanical motion has been limited to simple bending in most cases. Therefore, photomechanical crystals should be explored to exhibit more variety of motion.

Chiral molecules would work effectively for the diversification of photomechanical motion. It is well known that photoreactions in chiral crystals undergo with reflecting the chiral environment.[1,2] Thus, chirality may lead to chiral motion such as a twist.

Based on the concept, I have prepared for chiral azobenzene *trans*-(*S*)-**1**, which undergoes *trans–cis* photoisomerization upon UV light irradiation (Scheme 2.1). In this chapter, I describe photomechanical bending with a slight twist of the chiral azobenzene crystals. The bending behavior is discussed based on the *cis*-conformer optimized by theoretical calculation, suggesting that the bending with a twist is caused by elongation along the *b* axis and shrinkage along the *a* axis. This chapter is partly reproduced with a slight modification from "Taniguchi, T., Fujisawa, J., Shiro M., Koshima, H., Asahi, T. Mechanical motion of chiral azobenzene crystals with twisting upon photoirradiation. *Chem. Eur. J.* **22**, 7950–7958 (2016)". Copyright 2016 John Wiley and Sons.

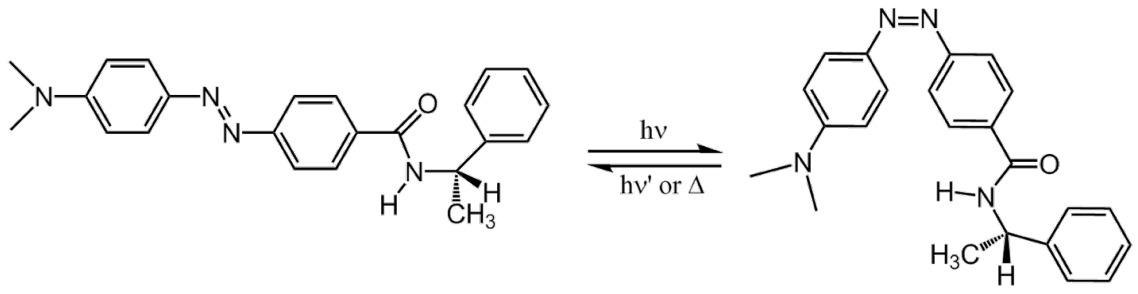

Scheme 2.1 Photoisomerization of chiral azobenzene *trans*-(*S*)-**1**.

2.2 Experimental section

2.2.1 Material preparation

S- and *R*-enantiomers of *N*-[[4-*p*-dimethylaminophenylazo]benzoyl]-1-phenylthylamine (*trans*-(*S*)-**1**, *trans*-(*R*)-**1**) and racemate (*trans*-(*rac*)-**1**) were synthesized as reported previously.[3,4] Single crystals of their compounds were prepared by evaporation of methanol solutions at room temperature.

2.2.2 X-ray crystallographic analysis

Single crystal X-ray diffraction (XRD) data of *trans*-(*S*)-**1**, *trans*-(*R*)-**1**, and *trans*-(*rac*)-**1** crystals were collected using a Rigaku R-AXIS RAPID diffractometer equipped with monochromatic Cu-Kα radiation (λ = 1.54187 Å). The crystal structures were solved using a direct method with SHELXS97[5] or SHELXD2013[5] and refined on F^2 by the full-matrix least-squares method. Calculations were performed using Rigaku crystal structure software packages.[6]

2.2.3 Absorption measurement with an optical waveguide spectrometer

UV-vis absorption spectra of powdered samples were measured with an optical waveguide spectrometer SIS-5000 (System Instruments Co., Ltd.) at the incident angle of 20° as shown in Figure 2.1. A small amount of powdered sample (less than 1 mg) was gently pressed to the waveguide for evanescent waves to reach the sample. The sample was irradiated from the upper side by UV light (UV-LED lamp UV-400, Keyence) or visible light (300 W xenon lamp MAX-303, Asahi Spectra Co., Ltd.) with a 440 nm bandpass filter (Asahi Spectra Co., Ltd.).

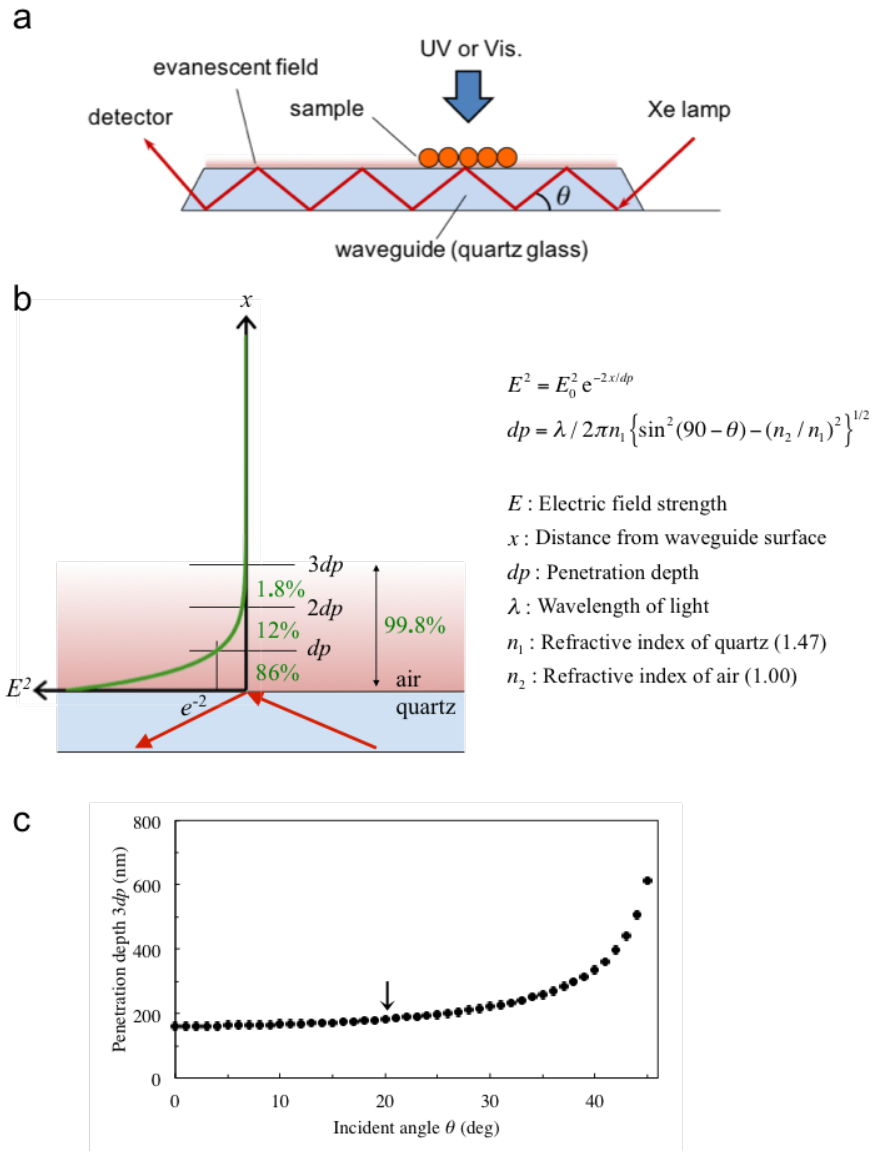

Figure 2.1 (**a**) The optical system of optical waveguide spectrometer and excitation light of UV or visible light. UV-vis absorption spectra of powdered crystals were measured at $\theta = 20°$. (**b**) The relation between the electric field strength of evanescent light and distance from the waveguide surface. (**c**) Penetration depth $2dp$ of evanescent wave depending on incident angle θ. Here, assumptions of $\lambda = 365$ nm, $n_1 = 1.47$ (quartz glass), and $n_2 = 1.00$ (air) were applied for calculation.

2.2.4 Observation of photomechanical motion

Forms α and β of *trans*-(*S*)-**1** and *trans*-(*R*)-**1** powder crystals were sublimated at 190 °C for 5 h in separate aluminum pans covered with glass plates to give thin crystals on glass plates. Thin crystals on glass plates obtained by sublimation were submitted to powder XRD measurements to identify the face index of obtained crystals. Thin *trans*-(*rac*)-**1** crystals were also prepared in the same way. A piece of thin crystal was fixed to the tip of a glass needle. Photomechanical motions upon UV light irradiation were observed with a digital high-speed microscope (VHX-5000; Keyence). Irradiation was performed using a UV-LED lamp UV-400 (365 nm, 40 mW, Keyence).

2.3 Results and Discussion

2.3.1 Crystal structures

By recrystallization, two polymorphisms of *trans*-(*S*)-**1** crystal were obtained (Figure 2.2a, b). One is plate-like (form α) and the other is needle-like (form β). Initially, form β crystals of *trans*-(*S*)-**1** were grown when evaporation was rapid. When the solution was evaporated slowly, form α crystals of *trans*-(*S*)-**1** were obtained. Melting points of form α and form β of *trans*-(*S*)-**1** were found to be 221.0–222.0 °C and 219.5–221.2 °C, respectively. Two polymorphs of *trans*-(*R*)-**1** were also obtained by recrystallization because the *R*-enantiomer is thermodynamically identical to the *S*-enantiomer. *Trans*-(*rac*)-**1** crystals were smaller than that of chiral crystals (Figure 2.2c). The melting point of *trans*-(*rac*)-**1** crystal was 208.7–211.7 °C.

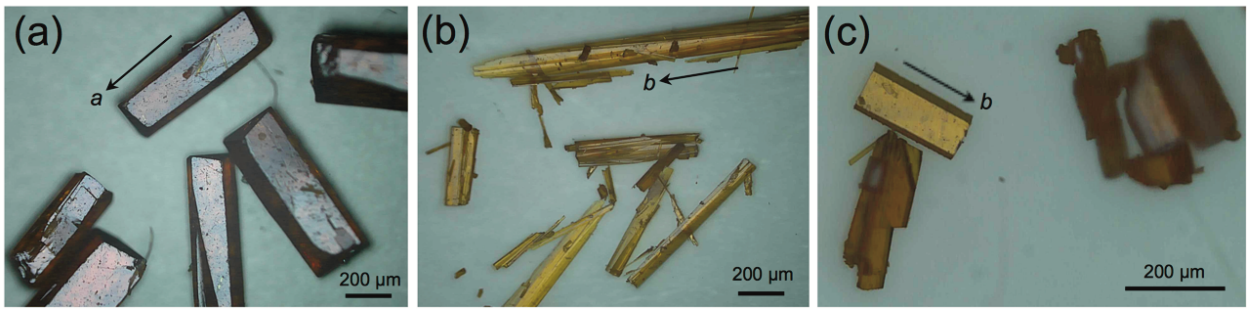

Figure 2.2 Photographs of (**a**) form α and (**b**) β crystals of *trans*-(*S*)-**1**, and (**c**) *trans*-(*rac*)-**1** crystals obtained from methanol solution by solvent evaporation at room temperature.

Crystal structures of *trans*-(*S*)-**1**, *trans*-(*R*)-**1**, and *trans*-(*rac*)-**1** were determined at 20 °C by X-ray crystallographic analysis (Table 2.1). Form α and β of *trans*-(*S*)-**1** belonged to the space groups $P2_12_12_1$ and $P2_1$, respectively. Because the azobenzene skeleton is almost planar, the molecule forms a dihedral angle between the azo plane and phenyl ring of the side chain. In form α of *trans*-(*S*)-**1**, the independent molecule forms 62.3° dihedral angle (Figure 2.3a and Table 2.2).

To understand the molecular packing of form α, the molecular alignment on the (100) face is shown (Figure 2.3b). Viewed from the (001) face, the form α of *trans*-(*S*)-**1** crystal forms herringbone structure with the acute angle of 52.0° (Figure 2.3c). The NH---O distance, which represents the distance between H atom of the amino group and O atom of the carbonyl group of *trans*-(*S*)-**1** molecules along the *a* axis, was 2.7 Å. At this distance, a very weak hydrogen bond is formed.

Table 2.1 X-ray crystallographic data of *trans*-(*S*)-**1**, *trans*-(*R*)-**1**, and *trans*-(*rac*)-**1** crystals measured at 20 °C.

	trans-(*S*)-**1** (α)	*trans*-(*S*)-**1** (β)	*trans*-(*R*)-**1** (α)	*trans*-(*R*)-**1** (β)	*trans*-(*rac*)-**1**-hydrate	*trans*-(*rac*)-**1**
Formula	$C_{23}H_{24}N_4O$	$C_{23}H_{24}N_4O$	$C_{23}H_{24}N_4O$	$C_{23}H_{24}N_4O$	$C_{23}H_{24}N_4O{\cdot}0.2H_2O$	$C_{23}H_{24}N_4O$
M / g mol^{-1}	372.47	372.47	372.47	372.47	376.07	372.47
Crystal system	Orthorhombic	Monoclinic	Orthorhombic	Monoclinic	Monoclinic	Monoclinic
Space group	$P2_12_12_1$	$P2_1$	$P2_12_12_1$	$P2_1$	$C2/c$	$C2/c$
a / Å	5.72324(19)	9.7660(3)	5.72442(16)	9.7709(8)	30.587(5)	30.7026(13)
b / Å	14.8303(5)	5.5160(2)	14.8491(4)	5.5258(5)	5.8683(10)	5.7880(3)
c / Å	23.0909(7)	18.9256(6)	23.1228(6)	18.9383(14)	23.938(4)	24.0419(10)
β / °	90	100.7202(17)	90	100.720(3)	113.802(8)	113.9813(17)
V / Å^3	1959.90(11)	1001.70(6)	1965.49(9)	1004.67(14)	3931.2(11)	3903.6(3)
Z	4	2	4	2	8	8
ρ_{calc} / g cm^{-3}	1.262	1.235	1.259	1.231	1.271	1.267
R_1 [$I > 2(I)$]	0.0452	0.0459	0.0498	0.0721	0.0988	0.0832
wR_2 [$I > 2(I)$]	0.0946	0.1040	0.1114	0.1727	0.2856	0.2142
GOF	1.120	1.177	1.068	0.998	1.127	0.923

Form β of *trans*-(*S*)-**1** crystal was determined as disordered structure (Figure 2.3d–f). The disorder was caused by pedal motion of *trans*-(*S*)-**1** and the occupancy was refined to be molecule A: B = 0.63: 0.37. Disordered molecules had 88.9° and 76.9° dihedral angles between the azo plane and phenyl ring of the side chain (Figure 2.3d). Molecules were related by a two-fold screw axis along the *b* axis and formed a herringbone structure, whose acute angle was 66.4° on $(\bar{1}03)$ plane along the *b* axis (Figure 2.3e). The NH---O distance along the *b* axis was 2.6 Å between H_A---O_A, 2.5 Å between H_B---O_B, 2.7 Å between H_A---O_B, and 2.4 Å between H_B---O_A. Here, subscripts A and B represent molecule A of higher occupancy and molecule B of lower occupancy, respectively. At these distances, hydrogen bonds are formed very weakly. Comparing the calculated density between two polymorphisms of chiral crystals, form α has a larger density than form β. Based on the higher symmetry of the crystal structure and larger density, form α is more stable than form β.

Trans-(*rac*)-**1** crystal belonged to the space group *C*2/*c* and was hydrated. In the hydrate structure, water molecules were located on a two-fold axis. The ratio of azobenzene and water was 5: 1 at 20 °C. The independent molecule of *trans*-(*rac*)-**1**-hydrate had a 68.5° dihedral angle (Figure 2.3g). *S*- and *R*-enantiomers were related by a two-fold axis and two-fold screw axis (Figure 2.3h). Viewed perpendicular to the (104) face, azo planes of *S*- and *R*-enantiomer were aligned in parallel, and a herringbone structure was not observed (Figure 2.3i). The distance between azo planes of two enantiomers was 3.7 Å and the distance between centroids of phenyl rings composed of azobenzene was 3.9 Å. Statistically, the π−π interaction works within this distance.[7,8] In addition, the distance between the oxygen atom of water and the carbonyl group of *trans*-(*rac*)-**1** was 2.6 Å, and the O(H)---O hydrogen bond would be strong. The NH---O distance

between the same enantiomers along the *b* axis was 2.9 Å and the hydrogen bond was formed weakly.

Trans-(*rac*)-**1** crystal without water molecules was obtained by heating *trans*-(*rac*)-**1**-hydrate at about 150 °C for several minutes. *Trans*-(*rac*)-**1** crystal maintained single crystal quality even after excluding water, belonging to the same space group as the hydrate crystal (Table 2.1). By excluding water, the NH---O distance along the *b* axis became 2.8 Å. Therefore, the *b* axis of lattice constants of *trans*-(*rac*)-**1** became smaller than that of the hydrate.

Table 2.2 Intermolecular and intramolecular interaction chiral and racemic crystals.

	trans-(*S*)-**1** (α)	*trans*-(*S*)-**1** (β)	*trans*-(*rac*)-**1**-hydrate	*trans*-(*rac*)-**1**
Dihedral angle / °	62.3	88.9, 76.9	68.5	68.0
Acute angle / °	52.0	66.4	-	-
NH---O distance / Å	2.7	2.4–2.7	2.9	2.8
O(H)---O distance / Å	-	-	2.6	-

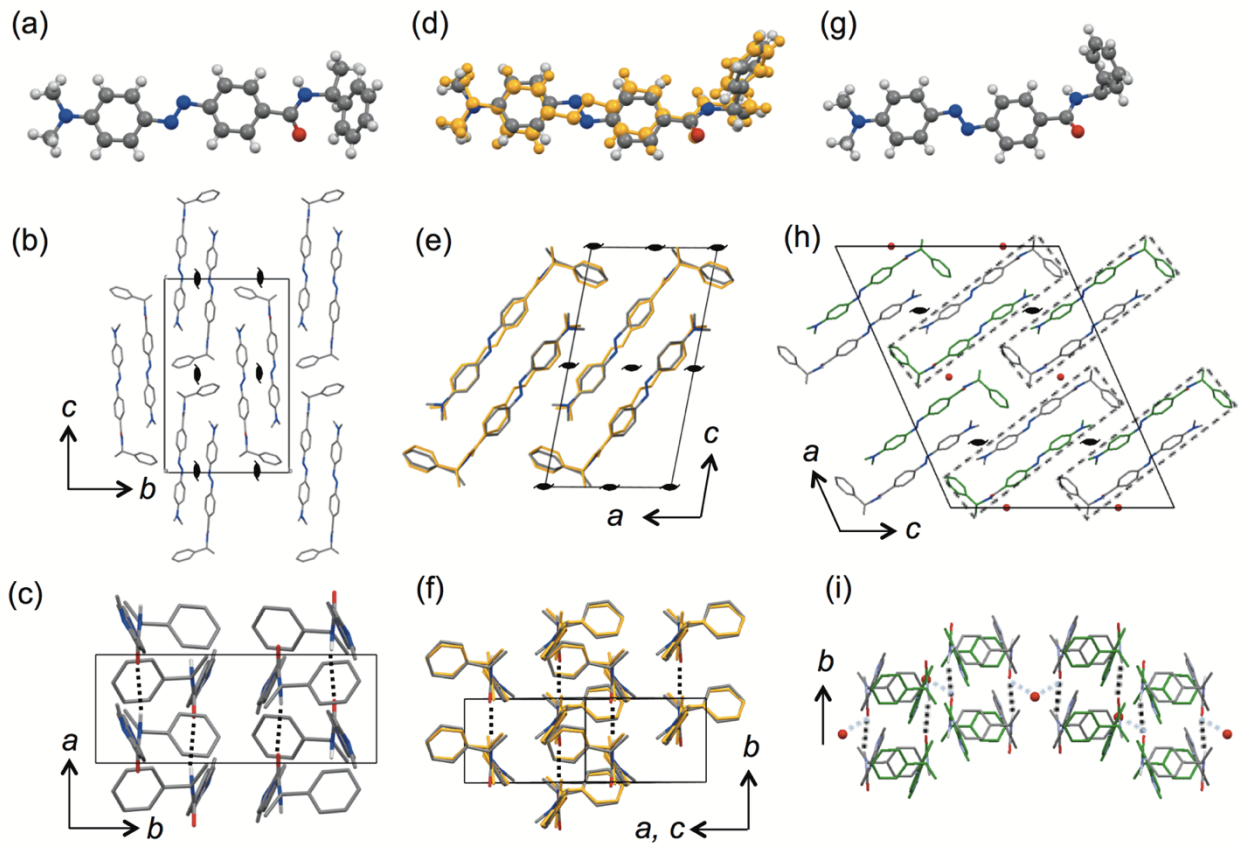

Figure 2.3 Crystal structures of (**a**–**c**) form α and (**d**–**f**) β of *trans*-(*S*)-**1** and (**g**–**i**) *trans*-(*rac*)-**1**-hydrate measured at 20 °C. (**a**) Molecular structure, (**b**) (100) packing, and (**c**) herringbone structure on the (001) face of form α of *trans*-(*S*)-**1**. NH---O interactions are shown as a dotted line. (**d**) Disordered molecule, (**e**) (010) packing, and (**f**) herringbone structure on ($\bar{1}$03) face of form β of *trans*-(*S*)-**1**. Molecules with minor occupancy of disordered molecules are drawn as yellow. NH---O interactions are shown as the dotted line. (**g**) Molecular structure, (**h**) (010) packing, and (**i**) π stacking structure on (104) face of *trans*-(*rac*)-**1**-hydrate. Carbon atoms of (*R*) enantiomer are drawn as green. Four pairs of (*S*) and (*R*) enantiomer surrounded by squares in **h** and one period above molecules are shown in **i**. O(H)---O and NH---O interactions are shown as blue dotted lines and black dotted lines, respectively. In these packing figures, hydrogen atoms are omitted for clarity.

2.3.2 *Trans-cis* photoisomerization

Measurement of UV-vis absorption spectra of the powdered samples before and after UV irradiation was first attempted by using transmittance spectrometry, as well as by diffuse reflectance spectrometry. However, any spectral change upon UV irradiation was not observed, probably because the photoisomerization occurred only near the crystal surface. Therefore, optical waveguide spectrometry was employed, which is used to measure absorption of the evanescent wave emerging from the waveguide surface based on the total internal reflection.[9,10] The measurement was conducted at 20 °C under three different conditions, that is, 1) during UV light (365 nm, 40 mW) irradiation, 2) after stopping UV light irradiation, and 3) during visible light (440 nm, 40 mW) irradiation just after stopping UV light.

The UV-vis absorption spectra of α-crystals of *trans*-(*S*)-**1** revealed an absorption peak at 460 nm derived from an n–π* transition; the peak intensity increased upon UV irradiation due to *trans*-to-*cis* photoisomerization (Figure 2.4a). The spectral change reached the steady state within 5 s after UV irradiation. The appearance of an isosbestic point at 395 nm verified the *trans*-to-*cis* isomerization. The apparent half-life $\tau_{1/2UV}$ of *trans*-to-*cis* photoisomerization was estimated to be 0.83 s (Table 2.3). Here, $\tau_{1/2UV}$ represents the apparent half-life because the half-life depends on the wavelength and the intensity of the UV light. In general, the absorption intensity is very weak because n–π* transition is prohibited due to the orthogonality of the n and π* orbitals.[11] However, azobenzene derivatives with an electron donor substituent, such as an amino group, exhibit a larger n–π* absorption due to overlapping of the wave functions of the n and π* orbitals.

When UV light irradiation was stopped, the peak at 460 nm decreased gradually due to *cis*-to-*trans* thermal back-isomerization and reached the steady state after about 1 min (Figure 2.4b). The half-life $\tau_{1/2}$ was estimated to be 22.8 s. Visible light irradiation just after stopping UV light

rapidly decreased the peak intensity at 460 nm due to *cis*-to-*trans* back-photoisomerization (Figure 2.4c). Half-life $\tau_{1/2vis}$ was estimated to be 1.91 s, although this half-life was also dependent on the wavelength and the intensity of the visible light.

In the same way, UV-vis absorption spectra of β-crystals of *trans*-(*S*)-**1** were measured (Figure 2.4d–f). The half-lives $\tau_{1/2UV}$, $\tau_{1/2}$, and $\tau_{1/2vis}$ were estimated to be 0.55, 12.4, and 1.14 s, respectively, which were almost half smaller than those of α-crystals (Table 2.3). The difference of half-lives suggested that the molecular motion of *trans*-(*S*)-**1** molecules is less restricted in the β-crystal than in the α-crystal. This is consistent with the crystallographic results showing a smaller density for the form β (1.235 g cm^{-3}) than for the form α (1.262 g cm^{-3}).

In the case of *trans*-(*rac*)-**1**-hydrate and *trans*-(*rac*)-**1** crystals, the absorption spectra also had n–π* peaks and isosbestic points, and the peak height changed in the same way as for the chiral crystals under the same irradiation conditions. The half-life values $\tau_{1/2UV}$, $\tau_{1/2}$, and $\tau_{1/2vis}$ of *trans*-(*rac*)-**1**-hydrate were 1.09, 21.4, and 1.67 s, respectively, which were slightly longer than those of the anhydrous *trans*-(*rac*)-**1** (i.e., 0.92, 18.7, and 1.39 s, respectively). The difference is related to the presence of water. As explained in the crystal structure section, *trans*-(*rac*)-**1**-hydrate forms an OH•••O=C hydrogen bond between water molecules and *trans*-(*rac*)-**1** in the crystal to tightly fix the azobenzene molecules. This is why the half-live values of *trans*-(*rac*)-**1**-hydrate were longer than those of anhydrous *trans*-(*rac*)-**1**. Furthermore, the half-life values of *trans*-(*rac*)-**1** were longer than those of form β of *trans*-(*S*)-**1**. In *trans*-(*rac*)-**1** crystal, two molecules of *S*- and *R*-enantiomer form a pair through the π–π interactions and the molecules are more tightly packed (density = 1.267 g cm^{-3}) than in form β of *trans*-(*S*)-**1** (density = 1.235 g cm^{-3}). Therefore, isomerization in *trans*-(*rac*)-**1** crystal took longer than in form β crystals of *trans*-(*S*)-**1**.

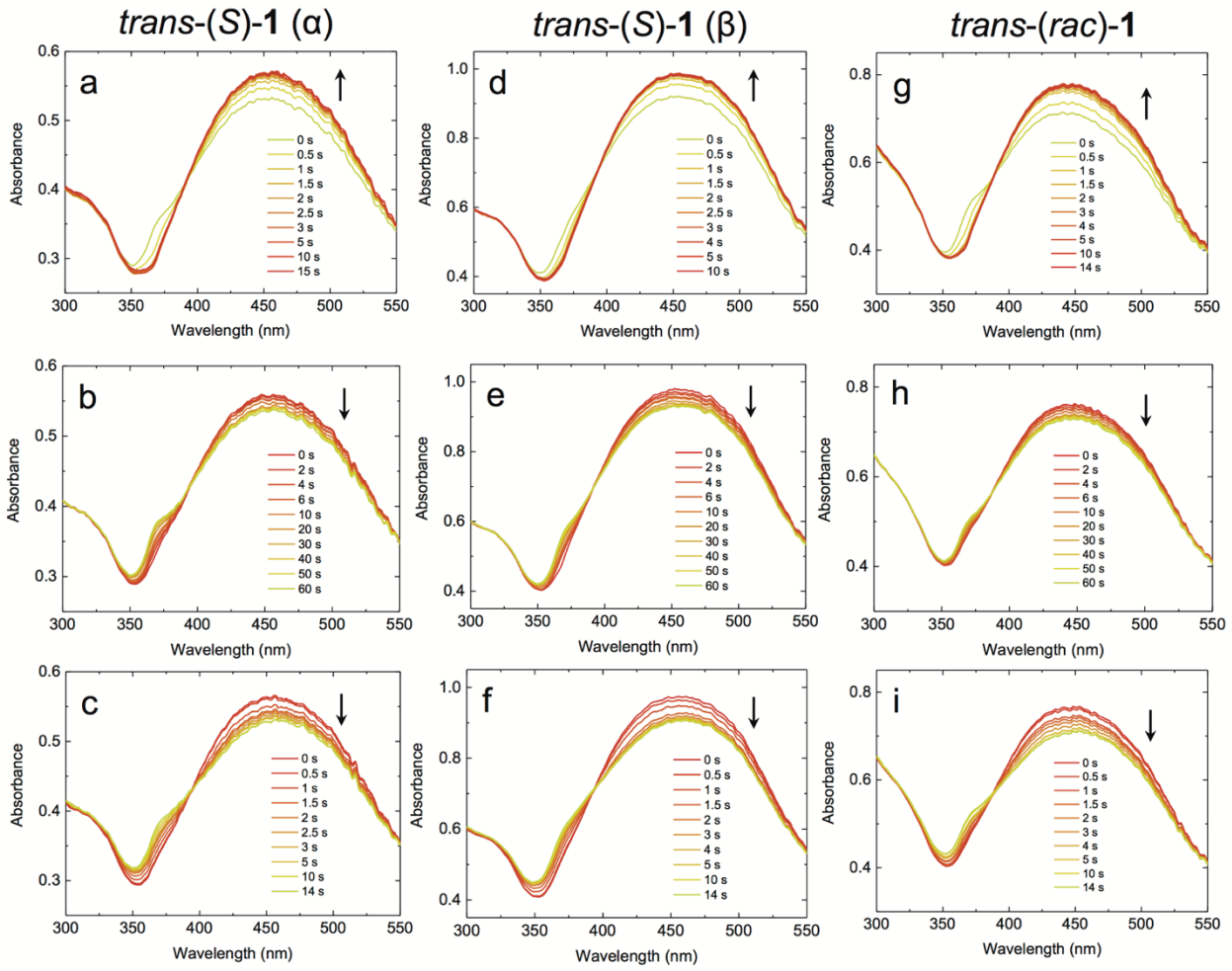

Figure 2.4 UV-vis absorption spectra of (**a**–**c**) form α and (**d**–**f**) form β of *trans*-(*S*)-**1** and (**g**–**i**) *trans*-(*rac*)-**1**-hydrate crystals measured at 20 °C using an optical waveguide spectrometer. In each compound, top, middle, and bottom panels show spectra (**a**, **d**, **g**) under UV light, (**b**, **e**, **h**) after stopping UV light, and (**c**, **f**, **i**) under visible light, respectively.

Table 2.3 Spectral information of chiral and racemic crystals.

	trans-(*S*)-**1** (α)	*trans*-(*S*)-**1** (β)	*trans*-(*rac*)-**1**-hydrate	*trans*-(*rac*)-**1**
λ_{max} / nm	460	450	440	440
Isosbestic point / nm	395	390	390	390
$\tau_{1/2UV}$ (*trans–cis*) / s	0.83	0.55	1.09	0.92
$\tau_{1/2}$ (*cis–trans*) / s	22.8	12.4	21.4	18.7
$\tau_{1/2vis}$ (*trans–cis*) / s	1.91	1.14	1.67	1.39

2.3.3 Photomechanical bending with twisting

Microcrystals of form β of *trans*-(*S*)-**1** grown on glass plates prepared by sublimation at 190 °C for 5 h (Figure 2.5a). However, microcrystals of form α of *trans*-(*S*)-**1** could not be obtained by sublimation. XRD measurements of the microcrystals of form β revealed six sharp peaks (Figure 2.5b), which were assigned to 001, 002, 003, 004, 005, and 007 reflections based on comparison with crystallographic data. The top surface of the plate-like microcrystals was identified as the (001) face with its longitudinal direction along the *b* axis based on comparison with plate-like bulk crystals. Microcrystals of form β of *trans*-(*R*)-**1** were also prepared in the same way.

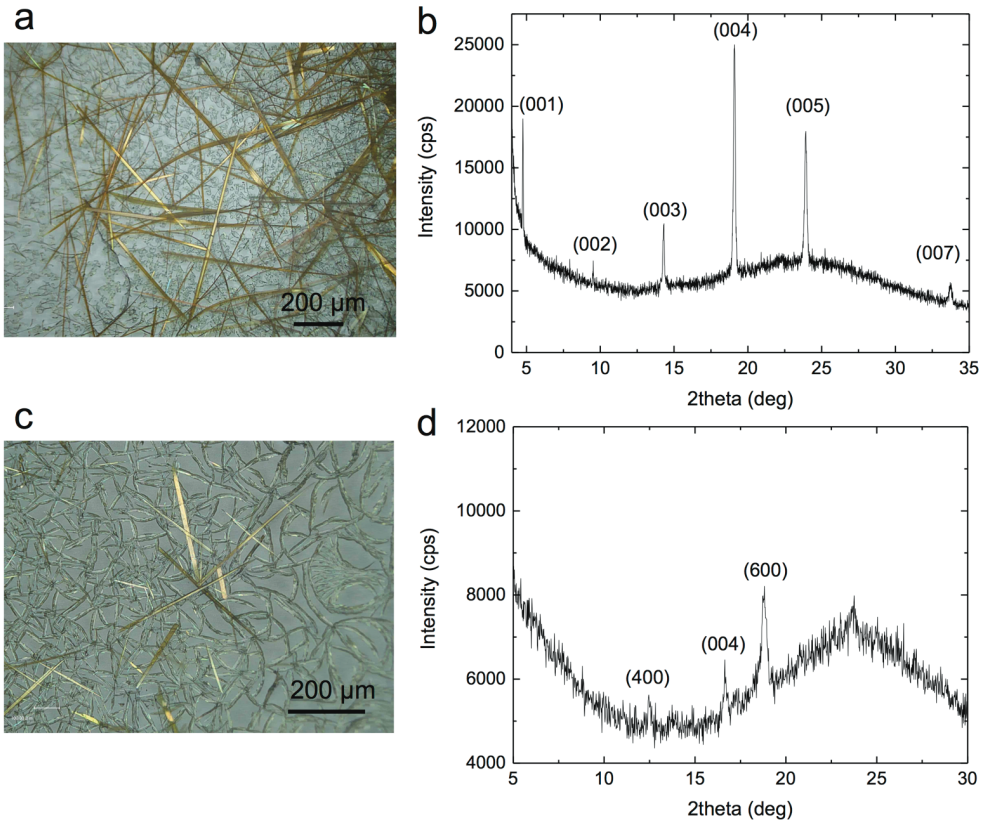

Figure 2.5 Photographs of (**a**) *trans*-(*S*)-**1** and (**c**) *trans*-(*rac*)-**1** microcrystals prepared by sublimation on glass plates, and the XRD patterns of (**b**) *trans*-(*S*)-**1** and (**d**) *trans*-(*rac*)-**1** microcrystals.

A piece of a long plate-like microcrystal (670 μm long × 52 μm wide × 2 μm thick) of form β of *trans*-(*S*)-**1** was manually picked, and the lower portion was fixed to a glass needle. The (001) top surface was identified based on the similarity of the tip form of the plate-like bulk crystal (Figure 2.6); that is. the back surface is the (00$\bar{1}$) face. When the (00$\bar{1}$) surface was irradiated by UV light (365 nm, 40 mW cm^{-2}) from the rear, the crystal bent away from the light source with a small left-handed twist, reaching maximum deflection after 5 s (Figure 2.7b–d). Stopping UV irradiation returned the bent crystal to the initial straight shape after 2 min. Irradiation of the (001) top face from the front induced backward bending with a small left-handed twist, demonstrating that both bending directions were possible, but the twisting direction was only left-handed (Figure 2.7e–g).

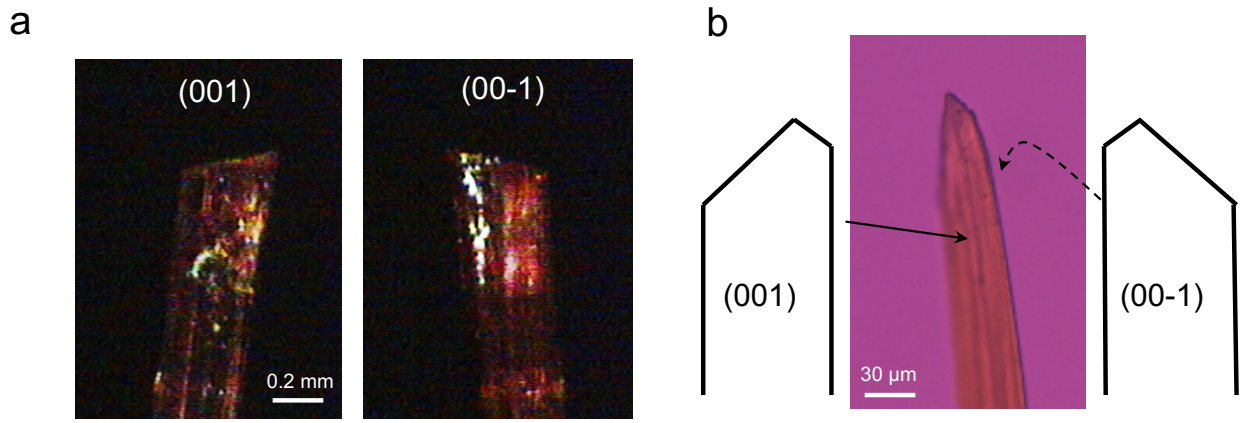

Figure 2.6 (**a**) (001) and (00$\bar{1}$) faces of *trans*-(*S*)-**1** crystal determined by X-ray crystallographic analysis. (**b**) (001) and (00$\bar{1}$) faces of *trans*-(*S*)-**1** plate-like microcrystal prepared by sublimation.

For comparison, the photomechanical motion of the opposite-handed β-form crystal of *trans*-(*R*)-**1** (435 × 47 × 1 μm^3) was examined (Figure 2.7h). When the rear (001) surface was illuminated from the back side at 365 nm, the crystal bent away from the light source with a small right-handed twist (Figure 2.7i–k). Upon UV irradiation of the (00$\bar{1}$) face from the front side, the

crystal bent away from the light source with a right-handed twist (Figure 2.7l–n), showing that both bending directions were possible, and the twisting direction was limited to right-handed, which was opposite to that of *trans*-(*S*)-**1**.

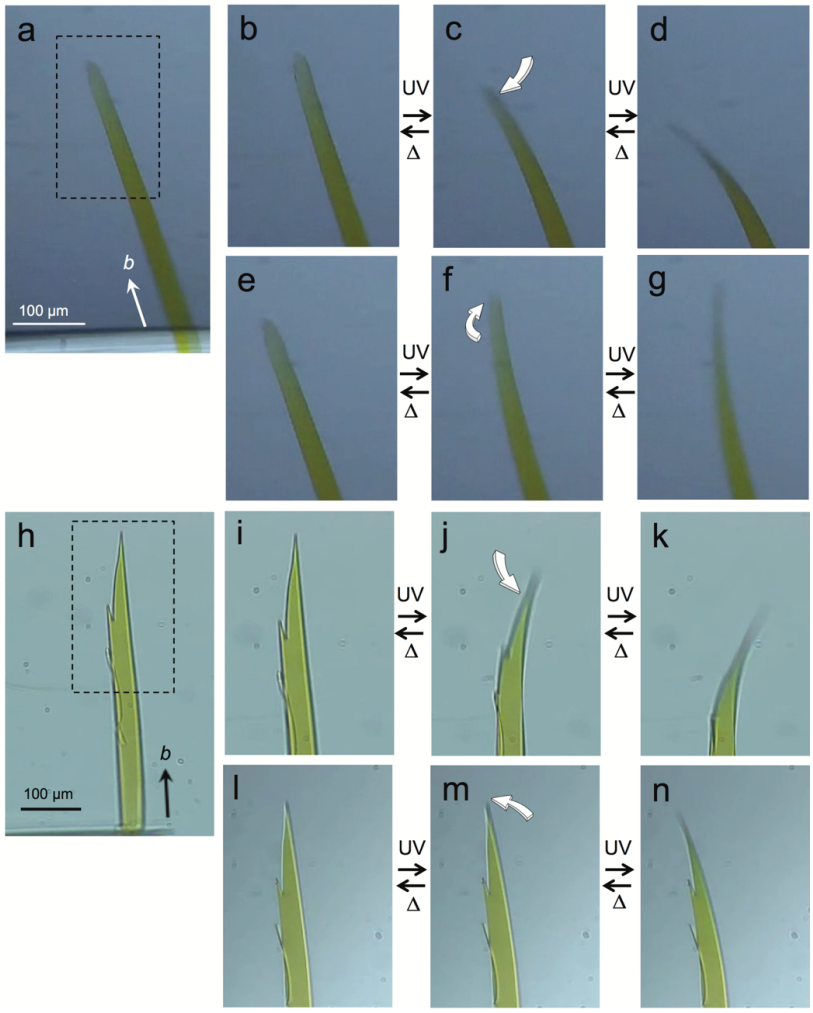

Figure 2.7 Photomechanical motions of plate-like β-form microcrystals of *trans*-(*S*)-**1** and *trans*-(*R*)-**1**. (**a**) Plate-like crystal of *trans*-(*S*)-**1**. Dotted square indicates an enlarged area in (**b**–**g**). (**b**–**d**) $(00\bar{1})$ face and (**e**–**g**) (001) face of *trans*-(*S*)-**1** crystal were irradiated by UV light. (**h**) Plate-like crystal of *trans*-(*R*)-**1**. The dotted square represents an enlarged area in (**i**–**n**). (**i**–**k**) (001) face and (**l**–**n**) $(00\bar{1})$ face of *trans*-(*R*)-**1** crystal were irradiated by UV light.

A rod-like (narrow plate-like) microcrystal (238 × 5 × 3 μm^3) of *trans*-(*R*)-**1** with one end fixed to a glass needle was exposed to repeated UV irradiation. The longitudinal direction was identified as the *b* axis by comparing with bulk crystals. Upon UV irradiation on the (001) or (00$\bar{1}$) face from the left side, the crystal bent away from the light source without twisting, reaching a maximum tip displacement angle of 5.5° after 6 s (Figure 2.8a, b). The bent crystal returned to the straight form 3 min after the irradiation was stopped. In contrast, visible light irradiation at 440 nm led to a faster recovery (2 min) due to the faster *cis*-to-*trans* back-photoisomerization than the thermal back-isomerization. This reversible bending was repeatable for at least 25 cycles of alternating UV irradiation (10 s) and darkness (5 min) (Figure 2.8c). The tip displacement angle of microcrystals decreased with increasing thickness. Microcrystals thicker than 7 μm did not exhibit any noticeable photomechanical response.

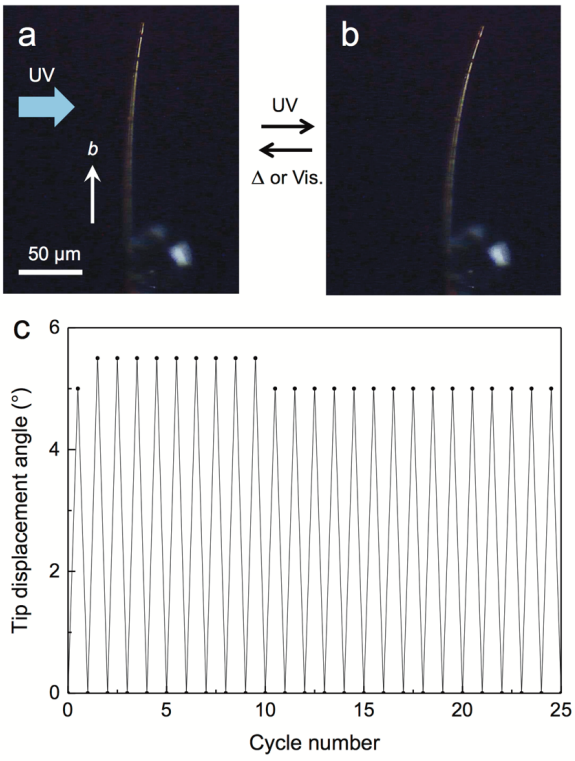

Figure 2.8 Photomechanical bending of rod-like β-form microcrystal of *trans*-(*R*)-**1**. (**a**) Before and (**b**) after UV light irradiation. (**c**) Repeatability of the reversible bending over 25 cycles.

Next, the photomechanical motion of a square-like (wide plate-like) microcrystal (187 × 135 × 1 μm^3) of compound *trans*-(*S*)-**1** with the lower corner fixed to a metal needle was observed (Figure 2.9). The longitudinal direction was identified to be the *b* axis. However, whether the top surface was (001) or $(00\bar{1})$ could not be determined. When the rear surface was irradiated from the back side by UV light (365 nm), the crystal curled toward the light source with a right-handed twist. The maximum bending angle was quite large to reach an acute angle along the *a* axis.

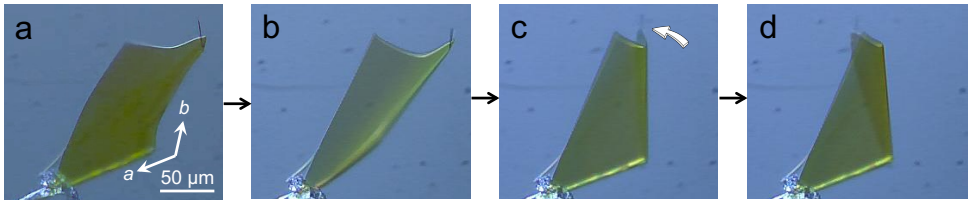

Figure 2.9 Top surface of a square-like β-form microcrystal of compound *trans*-(*S*)-**1**. (**a**) Before and (**b–d**) during UV light irradiation from the rear.

For comparison, the photomechanical motion of the racemic crystal of *trans*-(*rac*)-**1** was also investigated. The microcrystals were prepared by sublimation of the powdered *trans*-(*rac*)-**1**-hydrate crystals at 190 °C. Long plate-like microcrystals mainly grew on the glass plates (Figure 2.5c). However, the crystals changed to the anhydrous *trans*-(*rac*)-**1** crystals due to vaporization of water molecules during sublimation. XRD measurements revealed three peaks, which were assigned to 400, 004, and 600 reflections based on comparison with the XRD pattern calculated from single crystal data. The peak intensity of 600 reflection was the strongest of the three peaks. Hence, the top surface of most of the plate-like microcrystals was identified to be (100) face with the longitudinal direction along the *b* axis based on comparisons with plate-like bulk crystals of *trans*-(*rac*)-**1**-hydrate crystals.

Figure 2.10a shows the frontal (100) face of a long plate-like *trans*-(*rac*)-**1** crystal (320 × 34 × 2 μm^3) with one end fixed to a glass needle with glue. When the (100) face was irradiated from the left side by UV light (365 nm), the crystals quickly bent away from the light source without twisting to reach maximum bending after 3 s, but the displacement angle was small (Figure 2.10b, c). Irradiation from the right side also caused slight bending away from the light (Figure 2.10b, d).

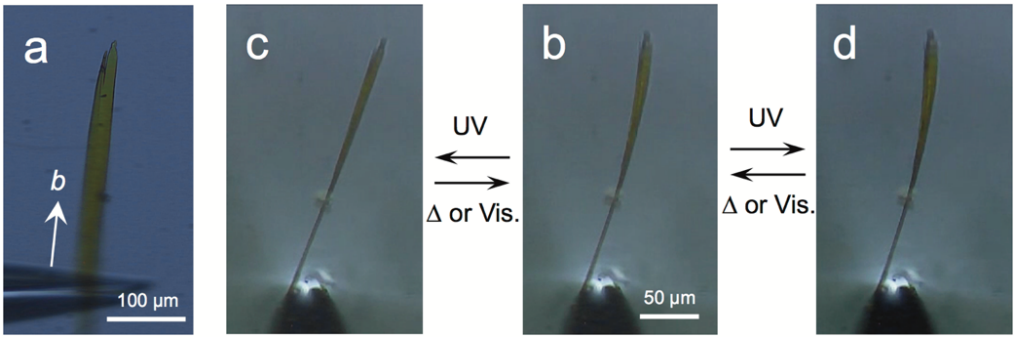

Figure 2.10 A long plate-like racemic microcrystal of *trans*-(*rac*)-**1** is shown (**a**) at the front (100) face, and the side view (**b**) before and (**c**) upon UV irradiation from the left side and (**d**) the right side.

2.3.4 Correlation of the mechanical motion with the crystal structures

Crystallographic analyses of form β of *trans*-(*S*)-**1** or *trans*-(*R*)-**1** before and after photoirradiation are required to elucidate the mechanism of photomechanical bending and twisting at the molecular level. The first trial was to measure changes in XRD patterns of the sublimated *trans*-(*S*)-**1** microcrystals before, during, and after UV light irradiation (Figure 2.11). The peak intensity decreased very little during UV light irradiation due to the *trans*-to-*cis* photoisomerization near the crystal surface. Furthermore, a shift in diffraction angles (2θ) was not observed, and a new peak did not appear. This diffraction behavior suggested that crystallographic analysis under UV irradiation was not possible. For an alternative way, molecular geometries of *cis*-(*S*)-**1** and *cis*-(*R*)-**1** were optimized by molecular mechanics using the universal force field algorithm in Avogadro.[12] To optimize the structure, the C-N=N-C torsion angle was constrained as −7.68° for *cis*-(*S*)-**1** and 7.68° for *cis*-(*R*)-**1** based on the reported crystal structure of *cis*-azobenzene.[13]

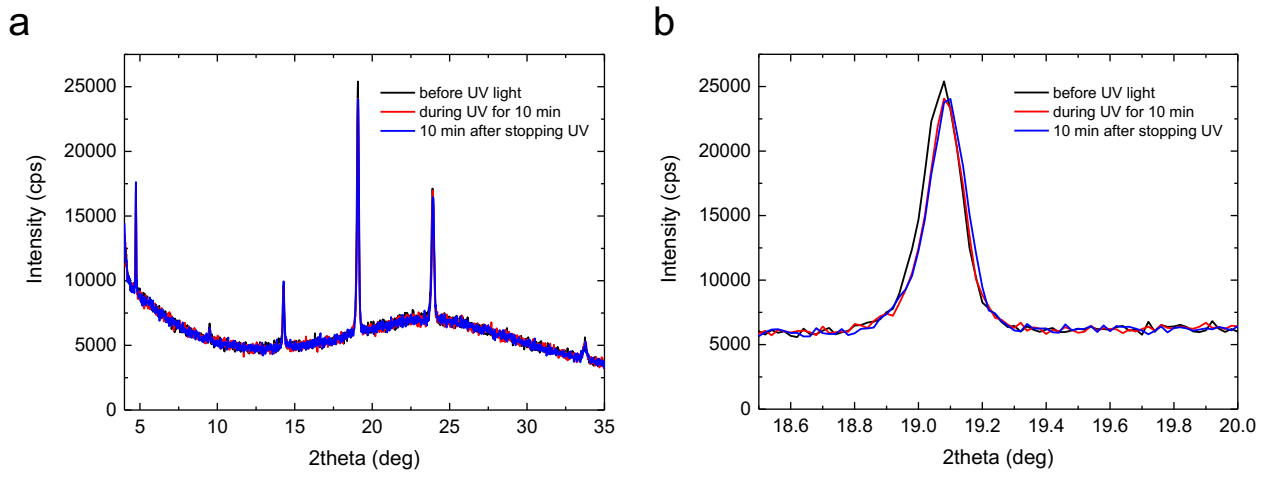

Figure 2.11 Changes of (**a**) powder XRD patterns and (**b**) the peak at 2θ = 19.1° of *trans*-(*S*)-**1** microcrystals before, during, and after UV irradiation.

Possible changes in molecular geometry accompanied by photoisomerization in *trans*-(*S*)-**1** crystal was only considered because *trans*-(*R*)-**1** crystal should be the mirror image of *trans*-(*S*)-**1** crystal. *Trans*-(*S*)-**1** molecule from the crystal structure and optimized *cis*-(*S*)-**1** molecule are shown in Figure 2.12. The length and width of *trans*-(*S*)-**1** molecule on the (010) face are 16.2 and 5.8 Å, respectively; those of *cis*-(*S*)-**1** molecule were 11.7 and 7.8 Å, respectively, showing that the length of the *cis* molecule shrinks and the width elongates (Figure 2.12a). On the (001) face, the length and width of a *trans*-(*S*)-**1** molecule were 11.6 and 3.8 Å, respectively, whereas those of a *cis*-(*S*)-**1** were 8.2 and 6.8 Å, respectively (Figure 2.12b). This suggests that the crystal length elongates along the *b* axis and shrinks along the *a* axis due to the *trans*-to-*cis* photoisomerization.

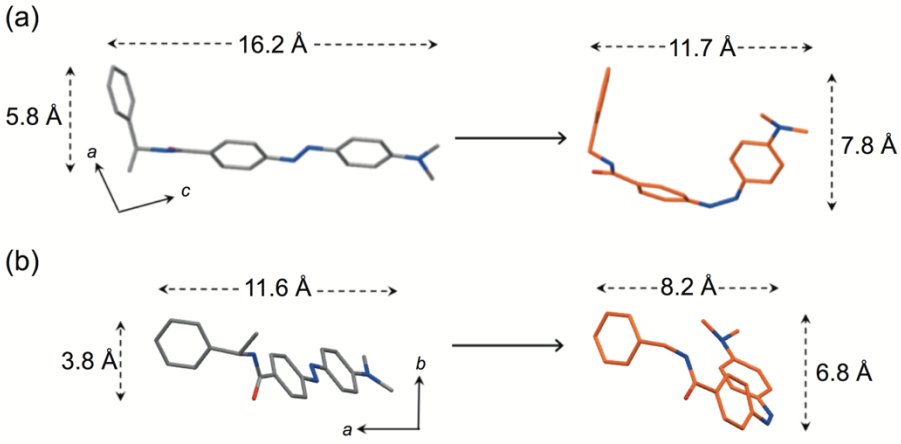

Figure 2.12 Molecular conformations of *trans*-(*S*)-**1** (grey) and optimized *cis*-(*S*)-**1** (orange) on (**a**) (010) face and (**b**) $(00\bar{1})$ face. The structure of *trans*-(*S*)-**1** was obtained based on the crystallographic results. Molecules with higher occupancies are only shown. Length shown in this figure represents the rectangular length, which can surround a molecule. Direction of the *cis*-(*S*)-**1** molecule was also optimized by least-squares for minimizing atom displacement accompanied by *trans–cis* isomerization.

Figure 2.13 shows the possible mechanism of bending and twisting of the *trans*-(*S*)-**1** crystal. On the (001) face, the *trans*-(*S*)-**1** molecules were arranged with intermolecular hydrogen bonding along the *b* axis to form a columnar structure (Figure 2.13a). The unit cell of *cis*-(*S*)-**1** was estimated based on molecular conformational changes, although *cis*-(*S*)-**1** might not form a new crystalline state. Based on the molecular conformational change, isomerization from *trans* to *cis* should increase the length of the *b* axis and contract the *a* axis of the unit cell. The overlay of packing arrangements of the *cis*-(*S*)-**1** and *trans*-(*S*)-**1** is shown in Figure 2.13b.

When the (001) face of a rod-like (narrow plate-like) crystal was irradiated with UV light, the length along the *b* axis should elongate near the surface, but the opposite surface should not change due to the lack of light penetration. This induces bending away from the light source (Figure 2.13c). In case of a long plate-like crystal, the length along the *b* axis elongates, and width along the *a* axis shrinks toward the light source to induce bending with a twisting motion (Figure 2.13d).

However, for the case of a square-like (wide plate-like) crystal, a curling motion along the *a* axis was observed (Figure 2.9), which differs from the bending motion of rod-like and plate-like crystals along the *b* axis. The molecules of *trans*-(*S*)-**1** are connected with intermolecular hydrogen bonding to form a columnar structure along the *b* axis on the (001) face, suggesting that the molecules are relatively difficult to move for the *trans*-to-*cis* photoisomerization. In contrast, the molecular interaction between the columns is weak van der Waals forces; the molecules can move easily due to photoisomerization. Hence, the square-like crystal can curl to an acute angle along the *a* axis. In addition, elongation of the length along the b axis induces some twisting motion (Figure 2.13e).

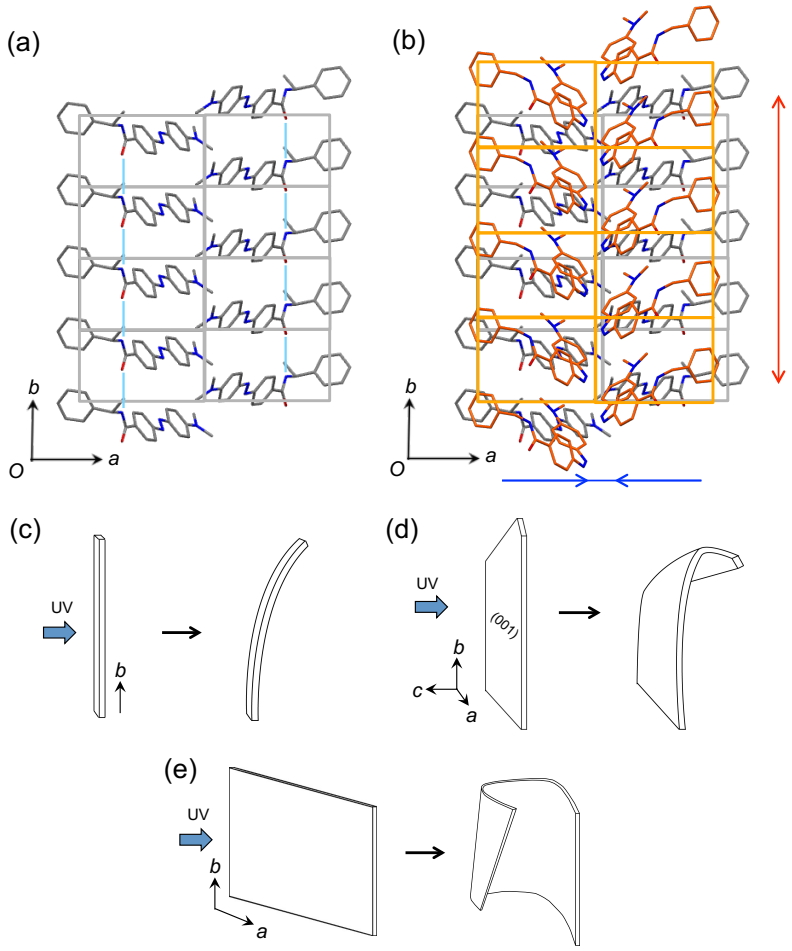

Figure 2.13 Possible mechanism of bending and twisting of the *trans*-(*S*)-**1** crystal. (a) Molecular packing on the (001) face of *trans*-(*S*)-**1** crystal (grey), and (b) the overlaid packing arrangements with *cis*-(*S*)-**1** crystal (orange). (**c**) Bending of rod-like crystal, (**d**) bending with twisting of plate-like crystal, and (**e**) curling with twisting of a square-like crystal of *trans*-(*S*)-**1** upon UV irradiation.

Figure 2.14 shows the possible mechanism of photomechanical motion of the racemic crystal of *trans*-(*rac*)-**1**. On the $(\bar{1}00)$ face, enantiomeric molecules of *trans*-(*S*)-**1** (gray) and *trans*-(*R*)-**1** (green) are alternately arranged in an almost parallel manner along the *c* axis, and further *trans*-(*S*)-**1** or *trans*-(*R*)-**1** molecules are connected through intermolecular hydrogen bonding to form an independent columnar structure along the *b* axis (Figure 2.14a). When *trans*-(*S*)-**1** and

trans-(*R*)-**1** isomerize to *cis*-(*S*)-**1** and *cis*-(*R*)-**1**, the optimized *cis* molecules elongate along the *b* axis and contract along the *c* axis. The molecular arrangement of *cis*-(*S*)-**1** (orange) and *cis*-(*R*)-**1** (purple) is overlaid in Figure 2.14a.

Upon UV irradiation of the $(\bar{1}00)$ face of plate-like *trans*-(*rac*)-**1** crystal, the length elongates along the *b* axis, and the width shrinks along the *c* axis near the irradiated surface. Because isomerization does not occur at the back surface due to a lack of penetration of irradiated light, the crystal should bend away from the light source (Figure 2.14b). In contrast to chiral crystal, the bending of *trans*-(*rac*)-**1** crystal was small and twisting was not observed (Figure 2.11). This may be due to the higher density (1.267 g cm^{-3}) of *trans*-(*rac*)-**1** crystal than that (1.235 g cm^{-3}) of chiral β-crystal. Thus, molecular motion in the *trans*-(*rac*)-**1** crystal is more restricted due to the dense packing; the process of *trans-cis* isomerization is more difficult in the racemic crystal, which explains the small bending of the *trans*-(*rac*)-**1** crystal.

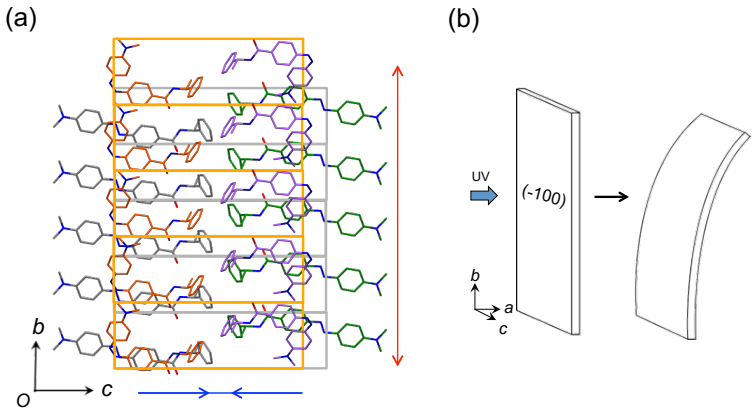

Figure 2.14 Possible mechanism of bending of *trans*-(*rac*)-**1** crystal. (**a**) Overlaid molecular packings of *trans*-(*rac*)-**1** and *cis*-(*rac*)-**1** crystals on the $(\bar{1}00)$ face; *trans*-(*S*)-**1** (gray), *trans*-(*R*)-**1** (green), *cis*-(*S*)-**1** (orange), and *cis*-(*R*)-**1** (purple). Unit cell of the *cis*-(*rac*)-**1** was estimated based on molecular conformational changes. (**b**) Bending of *trans*-(*rac*)-**1** crystal when the $(\bar{1}00)$ face was irradiated with UV light.

2.4 Conclusion

The photomechanical motion of chiral crystals of *trans*-azobenzene derivatives with *S*- and *R*-phenylethylamide group was investigated and compared with that of the racemic crystal. Changes in the UV-vis absorption spectra of the powdered crystals before and after UV irradiation were measured using an optical waveguide spectrometer, showing that the lifetimes of *cis*-to-*trans* thermal back-isomerization of the chiral crystals were faster than that of racemic crystals. Upon UV irradiation, a long plate-like chiral microcrystal bent away from the light source with some twisting motion. In contrast, the bending of the racemic microcrystal was smaller than that of chiral crystals, possibly due to the larger density of molecular packing. The possible mechanism of bending and twisting motion was discussed based on the *cis*-conformer optimized by theoretical calculation, because crystallographic analysis under UV irradiation was not possible, probably due to photoisomerization near the surface. Thus, the bending motion with twisting was caused by elongation along the *b* axis and shrinkage along the *a* axis. However, the relationship between the left- and right-handed twisting and the crystal structures requires further study.

2.5 References

1. Tanaka, K., Toda, F. Solvent-free organic synthesis. *Chem. Rev*. **100**, 1025–1074 (2000).
2. Sakamoto, M. Absolute asymmetric synthesis from achiral molecules in the chiral crystalline environment. *Chem. Eur. J.* **3**, 684–689 (1997).
3. Katritzky, A. R., He, H. Y., Suzuki, K. *N*-Acylbenzotriazoles: neutral acylating reagents for the preparation of primary, secondary, and tertiary amides. *J. Org. Chem*. **65**, 8210–8213 (2000).
4. Katritzky, A. R., Chen, Q. Y., Tala, S. R. Convenient preparations of azo-dye labeled amino acids and amines. *Org. Biomol. Chem.* **6**, 2400–2404 (2008).
5. Sheldrick, G. M. A short history of SHELX. *Acta Crystallogr. A* **64**, 112-122 (2008).
6. *CrystalStructure*, *version 4. 2. 2.*, Rigaku Corporation, Tokyo, Japan (2016).
7. Hunter, C. A., Sanders, J. K. The nature of π–π interactions. *J. Am. Chem. Soc.* **112**, 5525–5534 (1990).
8. Janiak, C. A critical account on π–π stacking in metal complexes with aromatic nitrogen-containing ligands. *J. Chem. Soc. Dalton Trans.* **0**, 3885–3896 (2000).
9. Mitsuishi, M., Tanuma, T., Matsui, J., Chen, J., Miyashita, T. In situ monitoring of photo-cross-linking reaction of anthracene chromophores in polymer Langmuir−Blodgett films by an integrated optical waveguide technique. *Langmuir* **17**, 7449–7451 (2001).
10. Takahashi, H., Fujita, K., Ohno, H. Direct visible spectral analysis of solid samples by optical waveguide spectroscopy due to adsorbed sample molecules after sublimation. *Chem. Lett.* **36**, 116–117 (2006).
11. Bandara, H. D., Burdette, S. C. Photoisomerization in different classes of azobenzene. *Chem. Soc. Rev.* **41**, 1809–1825 (2012).

12. Hanwell, M. D., Curtis, D. E., Lonie, D. C., Vandermeersch, T., Zurek, E., Hutchison, G. R. Avogadro: an advanced semantic chemical editor, visualization, and analysis platform. *J. Cheminf.* **4**, 17 (2012).

13. Mostad, A., Rømming, C. A refinement of the crystal structure of cis-azobenzene. *Acta Chem. Scand*. **25**, 3561–3568 (1971).

Chapter 3

Thermal locomotion of walking and rolling

3.1 Introduction

Mechanically responsive crystals have exhibited bending, twisting, jumping, and rotation in the past decade as described in previous chapters. However, the locomotion of materials has been limited. Several polymers and gels have shown locomotive features, and recent studies are increasing the examples.[1–8] In the case of a crystal, one molecular crystal has been reported to show slow crawling due to repeated crystallization and melting under light irradiation.[9] Despite present limitations, molecular crystals are expected to play important roles as locomotive materials and are being researched especially in the field of soft robotics.[10]

In chapter 2, I described that the chiral azobenzene *trans*-(*S*)-**1** is crystallized to form two polymorphs—an α phase (space group: $P2_12_12_1$) and a β phase (space group: $P2_1$)—and thin, plate-like crystals of the β phase bend with twisting under ultraviolet (UV) light irradiation.[11] In the course of the experiments, I found that the β-phase crystal exhibits a reversible structural phase transition to a γ phase at 145 °C.

In chapter 3, I describe that the β crystals walk slowly, like an inchworm, by repeating its shape change when alternately heated and cooled near the transition temperature. More surprisingly, thin, long crystals roll very fast by repeated bending and then flipping under only one process of heating or cooling. The driving force of both directional locomotion is generated from the unsymmetrical shape of the crystal. This walking and rolling crystal can be a beginning to the research and development of crystal robotics. This chapter is partly reproduced with a slight modification from "Taniguchi, T., Sugiyama, H., Uekusa, H., Shiro M., Asahi, T., Koshima, H. Walking and rolling of crystals induced thermally by phase transition. *Nat. Commun.* **9**, 538 (2018)". Copyright 2018 Springer Nature.

3.2 Experimental section

3.2.1 Material preparation and characterization

The *S*-enantiomer of chiral azobenzene, *trans*-(*S*)-**1** shown in Figure 3.1 was prepared according to a previously published procedure.[12,13] Single crystals of the β form of *trans*-(*S*)-**1** were recrystallized by slow evaporation from methanol or ethyl acetate at ambient temperature. Thermal analysis of *trans*-(*S*)-**1** crystals were performed with a differential scanning calorimeter (DSC 8500, Perkin Elmer) by using *ca*. 3 mg of the samples and empty aluminum pan as a reference, at a speed of 10 °C min^{-1} for heating and cooling.

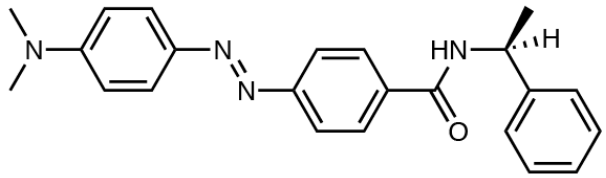

trans-(*S*)-**1**

Figure 3.1 Molecular structure of chiral azobenzene *trans*-(*S*)-**1**

Powder X-ray diffraction (XRD) measurements were performed with a SmartLab system (Rigaku), equipped with monochromatic Cu-Kα radiation (λ = 1.54187 Å) at 40 kV and 40 mA. A powdered sample of the β-crystal of *trans*-(*S*)-**1** was put on sample holder attached to a thermo-controller. Powder XRD data were collected at 25 °C and over the temperature range of 100–180 °C at intervals of 10 °C on heating and cooling. To allow for temperature stabilization, the interval was set at 1 min after reaching each temperature setting.

Single-crystal XRD data of β crystals of *trans*-(*S*)-**1** were collected using an R-AXIS RAPID diffractometer (Rigaku) equipped with monochromatic Cu-Kα radiation (λ = 1.54187 Å) at 50 kV and 100 mA. The temperature of the sample was regulated using an N_2 gas flow cryostat

and calibrated with a thermocouple. Because the temperature fluctuated in a range of approximately ±3 °C, the average value was chosen for plotting graphs. The sample was set in a glass capillary to prevent oscillation by the N_2 gas flow and sublimation at high temperatures. The crystal structures were solved using a direct method with SHELXS2013[14] or SHELXD2013,[14] and then refined on F^2 using the full-matrix least-squares method of SHELXL.[14] Calculations were performed using the Rigaku crystal structure software package[15] and a graphical interface, ShelXle.[16] Images of crystal structures were rendered with POV-Ray.[17]

3.2.2 Observation of shape change and locomotion of crystals

Shape change of a β-crystal of *trans*-(*S*)-**1**, at the phase transition, was observed on a glass plate using a polarized optical microscope (BX51, Olympus) with a microscopic thermo-controller (LMF-600S, Collet). The crystal was heated and then cooled in the temperature range of 120–160 °C at a rate of 20 °C min^{-1}. Locomotion of crystal under the repeated cycles of heating and cooling was observed on a silanized glass (Hampton Research, HR3-239) under a digital high-speed microscope (VHX-500, Keyence). The temperature was regulated with a glass hotplate (Tokai Hit). Temperature distribution during heating and cooling was measured with infrared (IR) thermography (FSV-2000, Apiste) from the top of the crystal (resolution: 25 μm^2 per pixel). Crystal motion was recorded simultaneously with a microscope from the side of the crystal for synchronization with thermography measurements; the periods of heating and cooling were modified to allow for simultaneous observation.

3.3 Results and Discussion

3.3.1 Phase transition

Differential scanning calorimetry (DSC) measurements of β crystals of *trans*-(*S*)-**1** were performed in the temperature range of 60–160 °C at a rate of 10 °C min^{-1} with heating and then cooling (Figure 3.2a). On heating, the DSC curve showed an endothermic peak at 145.2 °C. On subsequent cooling, the DSC curve had an exothermic peak at 143.0 °C, showing the small thermal hysteresis, of 2.2 °C. The enthalpies at these endothermic and exothermic peaks were small, 1.31 and −1.29 kJ mol^{-1}, respectively. The transition peak was also observed even after melt and crystallization (Figure 3.2b).

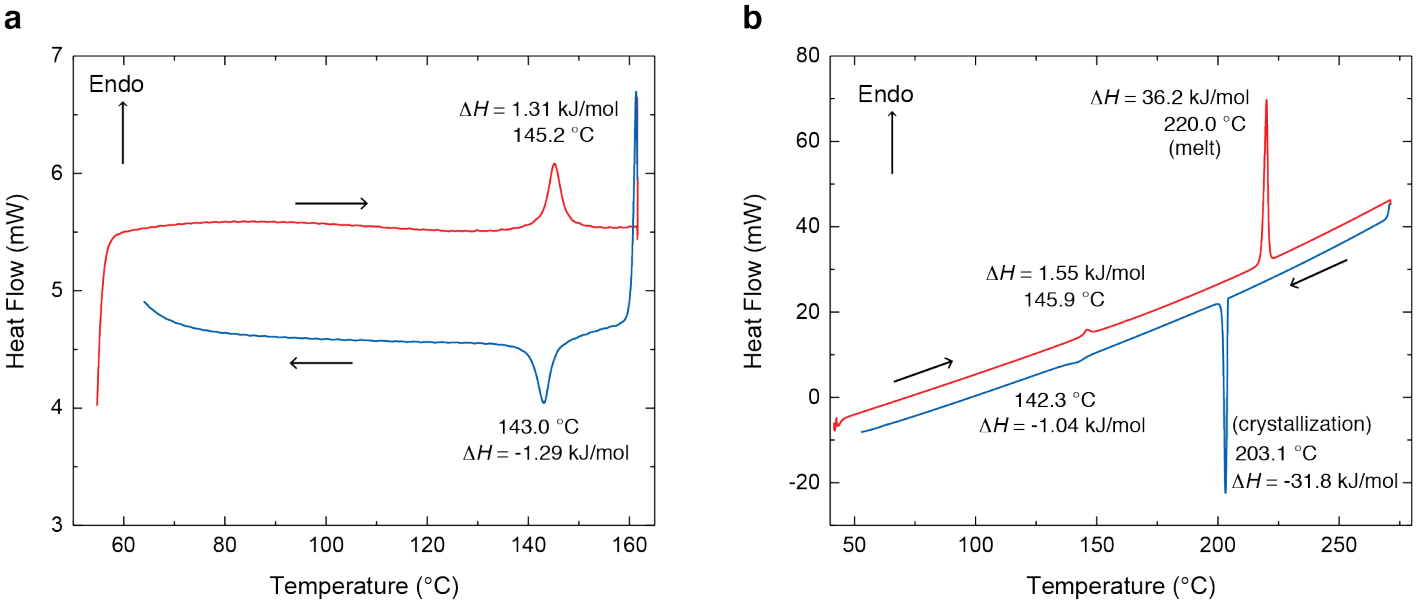

Figure 3.2 Differential scanning calorimetry (DSC) curve measured in the temperature range of (**a**) 60–160 °C and (**b**) 50–270 °C at a rate of 10 °C min^{-1} for heating and subsequent cooling. Red and blue lines represent heating and cooling, respectively.

Powder XRD profiles of β crystals of *trans*-(*S*)-**1** changed between 140 °C and 150 °C on heating, and then returned to the initial pattern between 150 °C and 140 °C on cooling, showing that the reversible structural phase transition without decreasing crystallinity (Figure 3.3). Here, the crystal structure above the transition temperature is referred to as the γ phase.

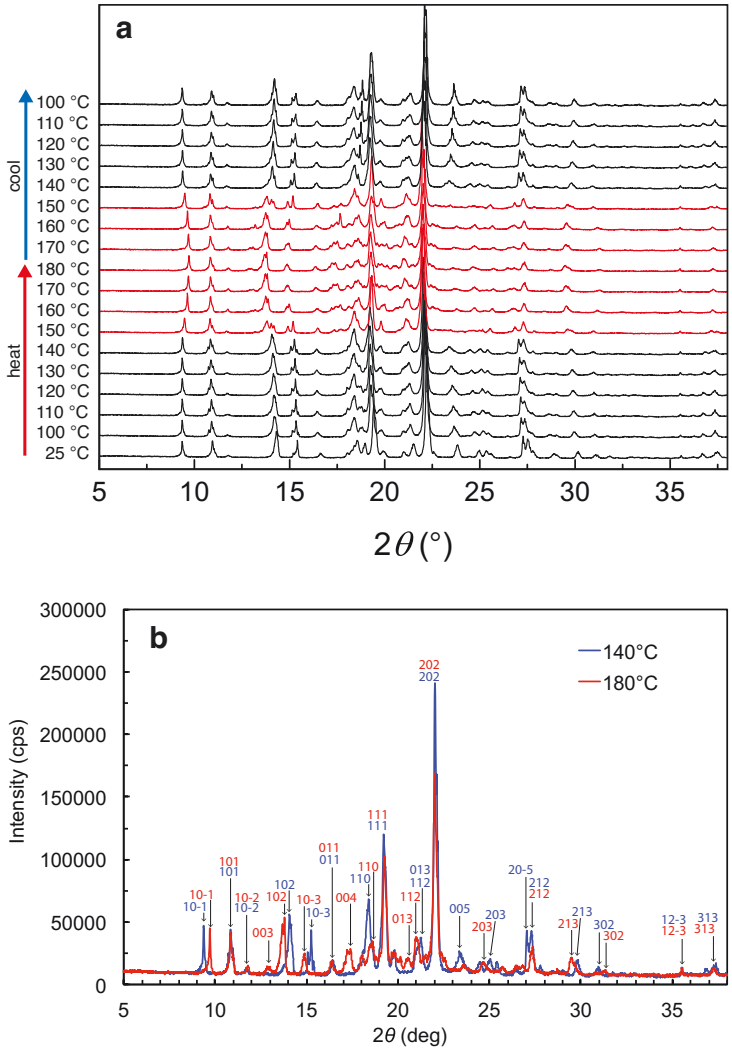

Figure 3.3 a, Powder XRD patterns at 25 °C and over the temperature range of 100–180 °C at 10 °C intervals on heating and then cooling. Black and red lines indicate β and γ phase, respectively. **b,** Comparison of XRD patterns of the β phase at 140 °C and the γ phase at 180 °C.

3.3.2 Crystal structures

X-ray crystallographic analyses of *trans*-(*S*)-**1** crystal were successfully performed at −100, 20, 100, 125, and 160 °C, verifying the structural phase transition from the β- to γ-crystal (Figure 3.4 and Table 3.1). Crystal structures at all temperatures belonged to the same space group, $P2_1$. The lattice constants changed discontinuously at 160 °C due to the phase transition to the γ phase. The lengths of *a*- and *b*-axes shortened, by −4.2% and −0.30%, respectively, between 125 °C and 160 °C; that of the *c*-axis elongated by +7.0% (Figure 3.4a–c).

Crystal structures at 20, 100, 125, and 160 °C were solved as disordered structures, although there was no disorder at −100°C (Figure 3.4e). Here, the molecular conformation at −100°C is defined as conformer A and the other conformation as conformer B. Occupancy of conformer A decreased with temperature rise, and that of B increased, to give 0.62:0.38 at 125°C in the β-crystal, and 0.44:0.56 at 160°C in the γ-crystal (Table 3.2).

These two conformers at 125 and 160 °C are illustrated to compare the molecular conformations (Figure 3.4g, h). The disorder was caused by a pedal motion of the azobenzene moiety. The dihedral angle between the azobenzene plane and the phenyl ring of the side chain, 81.03° of conformer A at 125 °C decreased considerably, to 56.17° at 160°C due to the phase transition (Figure 3.4f). The phenyl ring of the side chain in conformer A rotated by 25° (Figure 3.4g, h). In contrast, the dihedral angles 87.93° (at 125 °C) and 82.88° (at 160 °C) of conformer B did not change significantly before and after the phase transition.

In the β-phase crystal, weak intermolecular NH---O=C hydrogen bond chains form between the amido groups, with distances of 2.603 and 2.728 Å for the A and B conformers along the *b* axis, which is the longitudinal direction of the crystal (Figure 3.4i). After the transition to the γ phase, the phenyl ring of the conformer A becomes almost perpendicular to the *b* axis and parallel

to the *c* axis, leading to a slight shortening of the hydrogen bond distances (2.596 and 2.664 Å) for conformers A and B (Figure 3.4i). This conformational change allows molecules to push away surrounding molecules along the *c* axis and to condense along the *b* axis. However, the changes in molecular conformation and the packing arrangement are very small, which lead to the reversible structural phase transition with the small thermal hysteresis of 2 °C.

Table 3.1 Crystallographic parameters of the β and γ crystals of *trans*-(*S*)-**1**.

Temperature / °C	−100 (β)	20 (β)	100 (β)	125 (β)	160 (γ)
Empirical formula	$C_{23}H_{24}N_4O$	$C_{23}H_{24}N_4O$	$C_{23}H_{24}N_4O$	$C_{23}H_{24}N_4O$	$C_{23}H_{24}N_4O$
Formula weight	372.47	372.47	372.47	372.47	372.47
Crystal system	Monoclinic	Monoclinic	Monoclinic	Monoclinic	Monoclinic
Space group	$P2_1$	$P2_1$	$P2_1$	$P2_1$	$P2_1$
a / Å	9.7488(6)	9.7660(3)	9.7655(6)	9.7523(16)	9.345(7)
b / Å	5.3916(3)	5.5160(2)	5.5633(4)	5.5687(9)	5.552(4)
c / Å	18.8176(11)	18.9256(6)	19.0436(12)	19.131(3)	20.474(15)
β / °	100.605(7)	100.7202(17)	100.547(2)	100.432(6)	98.416(19)
V / Å^3	972.19(10)	1001.70(6)	1017.12(11)	1021.8(3)	1050.9(13)
Z	2	2	2	2	2
ρ_{calc} / g cm^{-3}	1.272	1.235	1.216	1.211	1.177
R_1 [$I > 2\sigma(I)$]	0.0694	0.0365	0.1051	0.0681	0.1190
wR_2 [$I > 2\sigma(I)$]	0.1552	0.0876	0.2999	0.1864	0.3059
GOF	1.062	1.207	1.159	0.886	0.743

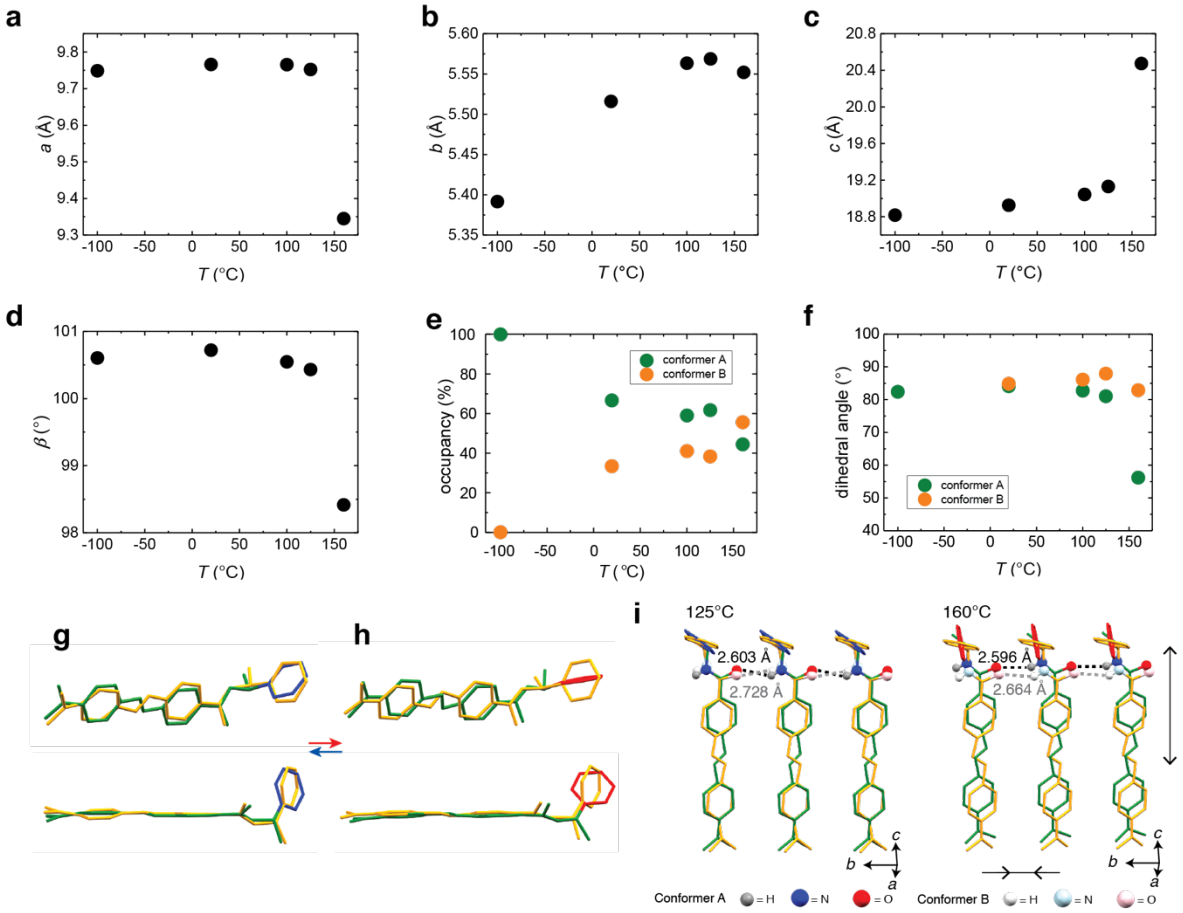

Figure 3.4 Characterization of the single-crystal-to-single-crystal phase transition. **a**–**d** Temperature dependence of lattice constants (−100, 20, 100, 125, and 160 °C); lengths of (**a**) *a*, (**b**) *b*, (**c**) *c* axes, and (**d**) angle *β*. **e** Occupancies of two conformers A and B. **f** Dihedral angles between azobenzene plane and the phenyl ring of the side chain in each conformer. **g, h** Conformers A (green) and B (yellow) at (**g**) 125 and (**h**) 160 °C. The phenyl ring of the side chain of conformer A is shown in blue and red at 125 and 160 °C, respectively. **i,** NH---O=C hydrogen bond chains along the *b* axis, which are derived from the two-fold helical molecular packing on the (010) face along the *b* axis. Hydrogen atoms are omitted for clarity.

Table 3.2 Occupancy, dihedral angle between the azobenzene plane and the phenyl ring of the side chain, and intermolecular hydrogen bond distance of each conformer of the disordered molecule.

Temperature / °C	−100 (β)		20 (β)		100 (β)		125 (β)		160 (γ)	
Conformation	A	B	A	B	A	B	A	B	A	B
Occupancy / %	100	0	66.6	33.4	59	41	61.7	38.3	44.4	55.6
Dihedral angle / °	82.38	-	84.09	84.85	82.74	86.11	81.03	87.93	56.17	82.88
NH···O=C hydrogen bond distance / Å	2.379	-	2.557	2.499	2.621	2.546	2.603	2.728	2.596	2.664

3.3.3 Shape changes

When a piece of the plate-like β-crystal (length 532 μm × width 133 μm × thickness 51.5 μm) was heated and then cooled on a conventional glass plate in the temperature range of 120–160 °C at a rate of 20 °C min^{-1} under a polarized optical microscope, the crystal deformed with no fracture due to the structural phase transition (Figure 3.5). When viewed from the (100) top face of the crystal on heating, the length along the *b* axis shrank (−0.56%), and the width along the *c* axis expanded (+4.5%; Figure 3.5a). The crystal returned reversibly to the initial shape on subsequent cooling. The shape change of the crystal was nearly consistent with the changes in the unit cell lengths of the *b* axis (−0.30%) and c axis (+7.0%) at the phase transition. When viewed from the (010) cross-section face, the width along the *c* axis expanded (+4.5%), and the thickness along the *a* axis contracted (−2.9%) on heating and then returned to the initial shape on cooling (Figure 3.5c).

When viewed from the (001) side face on heating, the plate-like crystal bent slightly along the *b* axis, and then became straight, with slight shortening (−0.56%) of the length along the *b* axis (Figure 3.5d). On subsequent cooling, the crystal bent again, and then returned to the initial shape.

This bending motion is caused by a temperature gradient to the thickness direction of the crystal. On heating, the phase transition, from β to γ phase, begins from the lower surface of the plate-like β-crystal, which contacts the glass plate; thus, the crystal shrinks near the lower part, along the longitudinal axis, inducing the bending motion, as understood from the molecular arrangement change on the (001) side face (Figure 3.5d). Then, the crystal becomes straight when the phase transition to the γ phase proceeds through the whole crystal. On subsequent cooling, the reverse phase transition, from γ to β phase, begins from the upper surface due to cooling by the surrounding air, and the crystal bends due to the elongation of the length. Then, the crystal returns to the initial straight shape when the transition to the β phase proceeds throughout the whole crystal.

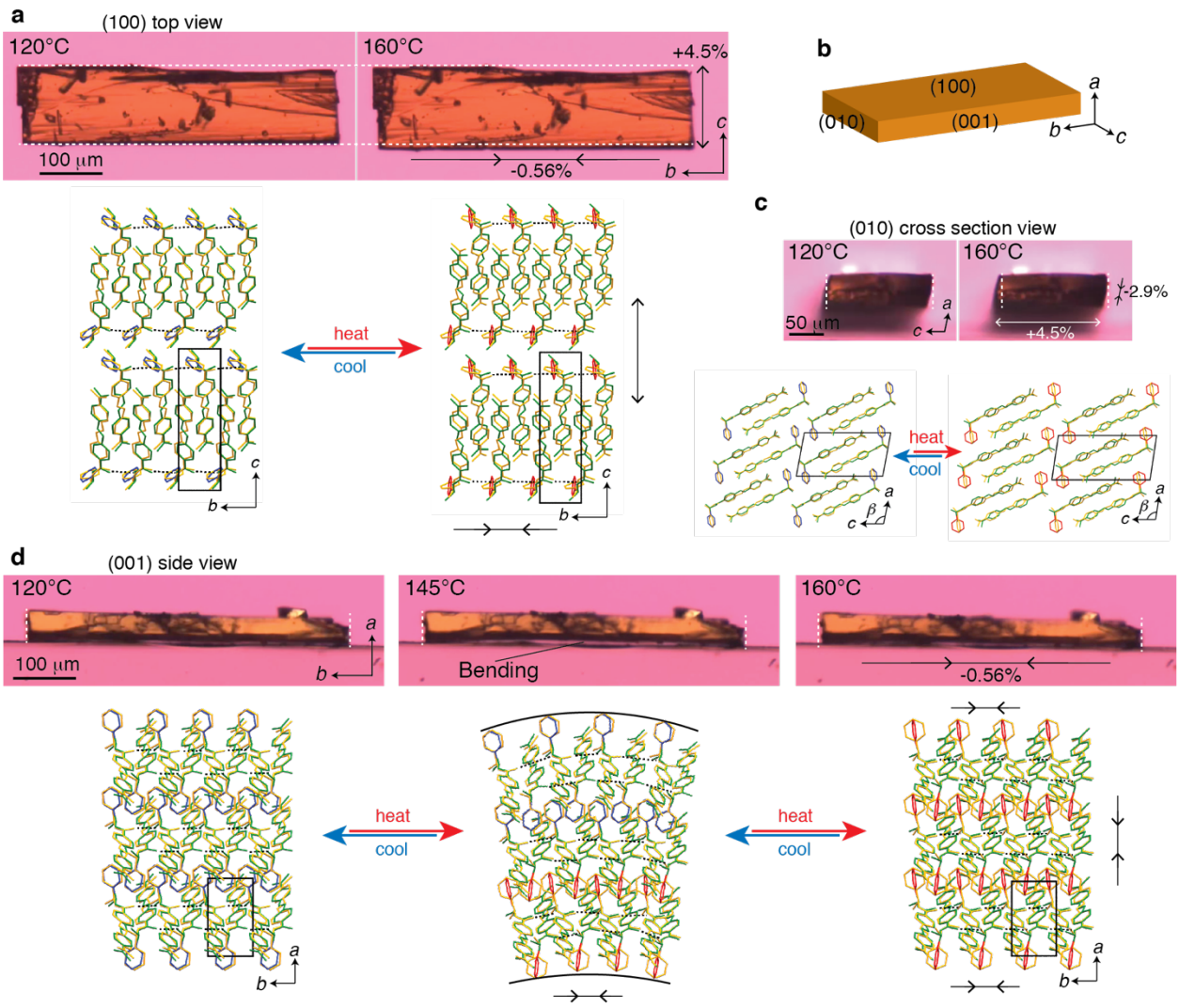

Figure 3.5 Changes of crystal shape and molecular arrangement under heating and cooling. **a,** (100) Top view before and after phase transition, and molecular packing on (100) face. **b,** Face indices of a plate-like crystal. **c,** (010) cross-section view and molecular packing on (100) face. **d,** (001) side view and molecular packing on (001) face. In each panel, dotted lines in the pictures (drawn in white) indicate the initial size of the β crystal. In packing diagrams, dotted lines (drawn in black) represent NH---O=C intermolecular hydrogen bonds along the *b* axis. Hydrogen atoms are omitted for clarity.

A longer, thinner crystal (2100 × 50 × 25 μm^3), the left edge of which was fixed with glue, bent more largely on heating and subsequent cooling, to reach a maximum bending angle, $\theta = 15°$ (Figure 3.6a, b). This reversible bending was observed over 200 cycles of alternating heating and cooling (Figure 3.6c).

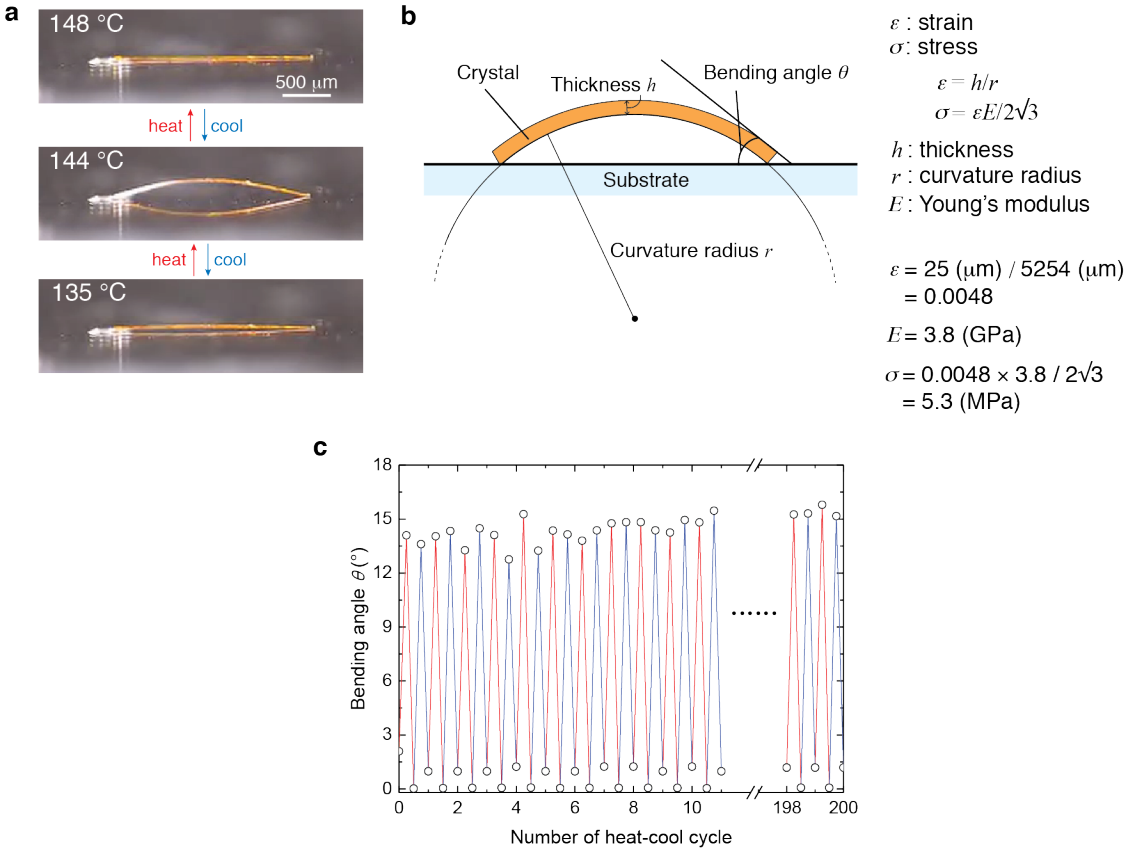

Figure 3.6 Bending of a thin, long plate-like crystal and mechanical properties of bending. **a,** Bending motion of a *trans*-(*S*)-**1** crystal, the left tip of which was fixed with glue to prevent locomotion. The motion was recorded with an optical microscope from the side. The mirror image was reflected on the glass surface. **b,** Definition of bending angle θ and calculation of strain and stress. The value of stress (5.3 MPa) was calculated by using the Young's modulus (3.8 GPa). **c,** Reversibility of bending motion. When the bending reached a maximum in each process of heating or cooling, the bending angle θ was calculated using the movie analysis software ImageJ.

3.3.4 Inchworm-like walking

When a long plate-like crystal (length 8.5 mm, width 200 μm, one end thickness 190 μm, and other end thickness 55 μm) with a thickness gradient in the longitudinal direction was repeatedly heated and cooled between 139 and 154 °C at speeds of 0.6 and 1.0 °C s^{-1}, respectively, on a silanized glass, surprisingly, the crystal walked slowly to the right along the long axis (*b* axis), like an inchworm, with repeated slight bending and straightening (Figure 3.7a). The walking distance reached 1.5 mm after 30 min (walking speed 3.0 mm h^{-1}). The average stroke on heating and cooling, estimated from the time profiles was 34 μm, which corresponds to 0.4% of the crystal length (Figure 3.8).

To further examine the mechanism of the inchworm-like walk, the surface temperature distribution of the crystal was monitored with an infrared (IR) thermography camera from the top of the crystal, and the crystal motion was observed simultaneously with a digital optical microscope from the side; the set-up and the combined video are shown in Figure 3.7b and. The speeds of heating and cooling between 132 and 150°C were slowed to 0.2 and 0.4 °C s^{-1}, respectively, for simultaneous observation. Figures 3.7c and 3.7d show the snapshots of the crystal motion and the surface temperature distribution. The temperatures measured at the selected points were displayed on the crystal (left, middle, and right) and the silanized glass with cross marks (Figure 3.7d).

On heating, the crystal remained straight until the surface temperature of the glass plate reached 140 °C (0 s, 45 s, Figure 3.7c, d). Then, the crystal bent gradually with fluctuation (45–98 s) and the thicker left edge tended to move slightly (47 μm) to the right during this bending, as shown in the enlarged picture (80 s, Figure 3.7c). At this time, the surface temperature of middle became lower (142 °C) than those of the left (144 °C) and right (146 °C) sides due to rising up

from the glass surface via bending (80 s, Figure 3.7d, e), and then the temperature difference increased until the surface temperature of middle reached 145 °C at almost 98 s (Figure 3.7e).

The bending ended suddenly at 98 s, and simultaneously the right edge hopped up, like a spring (98 s, Figure 3.7c), keeping the lifted shape until 105 s. At this time, the surface temperature of right decreased, to 144 °C, while those of left and middle became 148–149 °C (98 s, Figure 3.7d, e), and then the glass surface reached its maximum temperature (150 °C) on further heating (105 s, Figure 3.7e). Next cooling finished the lifting up at the right edge at 118 s, and then crystal bending began again (120 s, Figure 3.7c), decreasing the surface temperature rapidly in the middle, to ~141 °C (120 s, Figure 3.7d, e). Then, the crystal bending decreased gradually with the decrease in the crystal surface temperature, and finally returned to the initial straight shape with movement (42 μm) of the right edge to the right (150 s, Figure 3.7c).

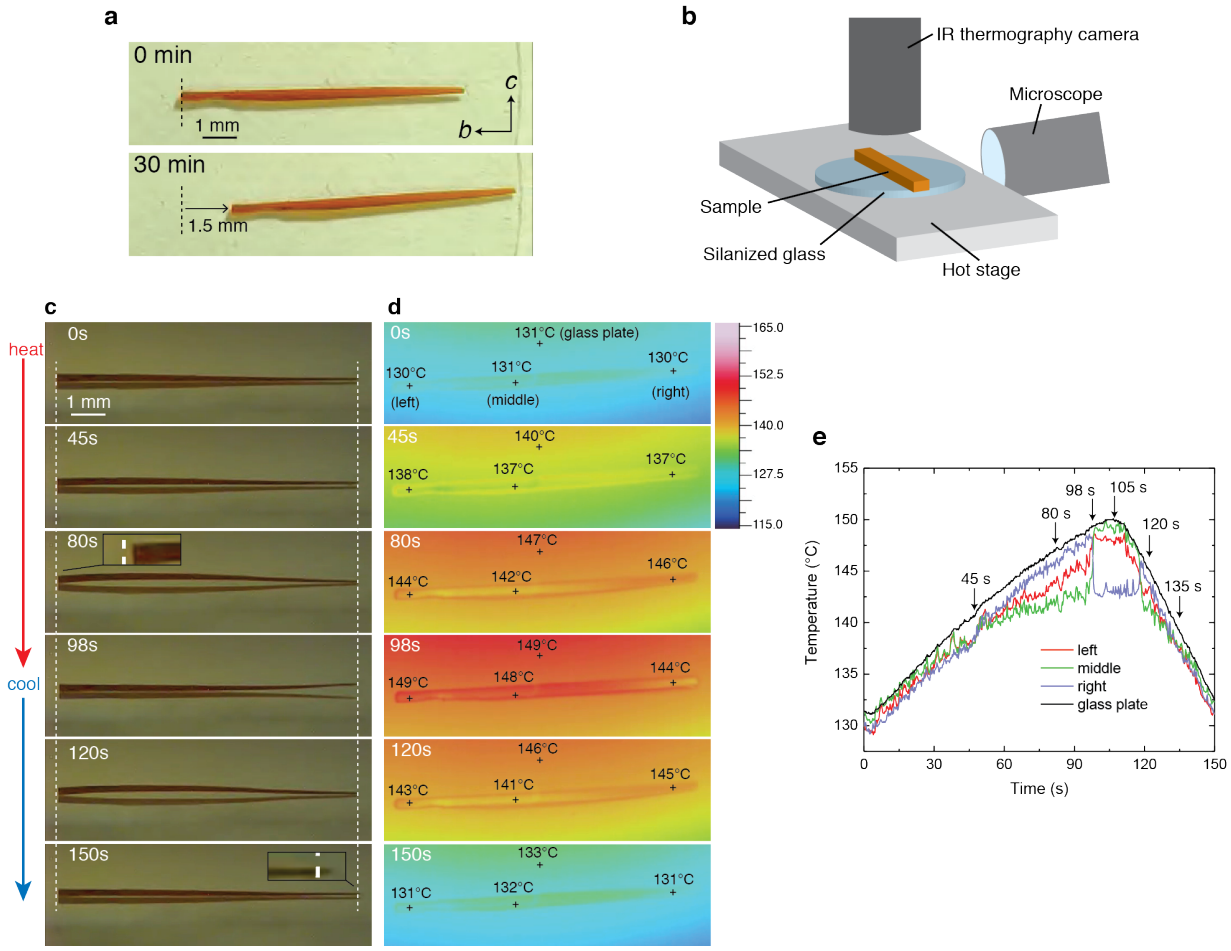

Figure 3.7 Inchworm-like walking of a long plate-like crystal with a thickness gradient. **a,** Inchworm walking by repeated heating and cooling cycles. **b,** Experimental setup for simultaneous observation by microscope and infrared (IR) thermography camera. **c, d,** Sequential snapshots during inchworm walk on heating and cooling, by optical microscope (**c**) and IR thermography (**d**). Dotted white lines in c indicate initial positions of the left and right edges. **e,** Time dependence of surface temperatures at the selected points on the crystal and the glass plate, shown as a cross mark in **d**.

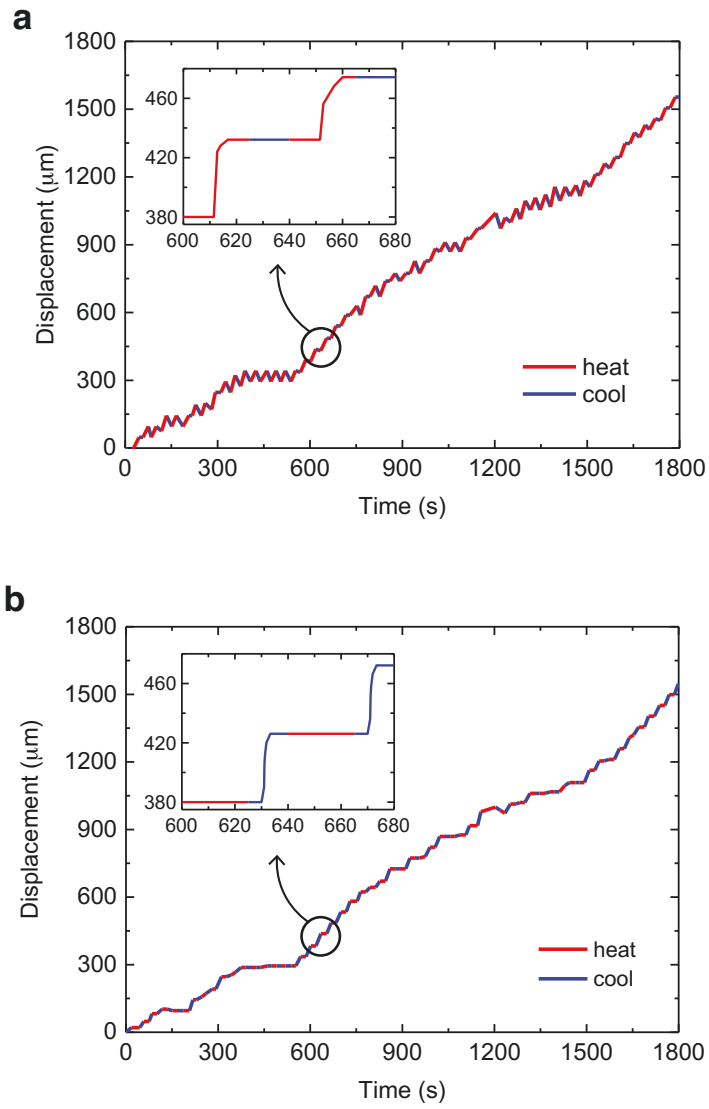

Figure 3.8 Time dependence of inchworm-like walking. **a, b**, Distances of left (**a**) and right (**b**) edges from initial positions of the crystal shown in Figure 3.7. On heating, the thicker left edge tended to move to the right, and the thinner right edge tended to stop. On cooling, the thicker left edge tended to stop or move slightly to the left, and the thinner right edge tended to move to the right.

The walking speed was estimated to be 1.0 mm h^{-1} at the slowed heating (0.2 °C s^{-1}) and cooling (0.4 °C s^{-1}) rate, which was three times slower than that (3.0 mm h^{-1}) at the heating (0.6 °C s^{-1}) and cooling (1.0 °C s^{-1}) rate in Figure 3.7a, showing that the walking speed is almost proportional to the heating and cooling rate. On a glass without surface treatment, the same crystal moved 1.1 mm in 30 min (walking speed 2.2 mm h^{-1}) to the right direction at the same heating and cooling rate in Figure 3.7a (Figure 3.9), which was slower than the speed 3.0 mm h^{-1} on a silanized glass.

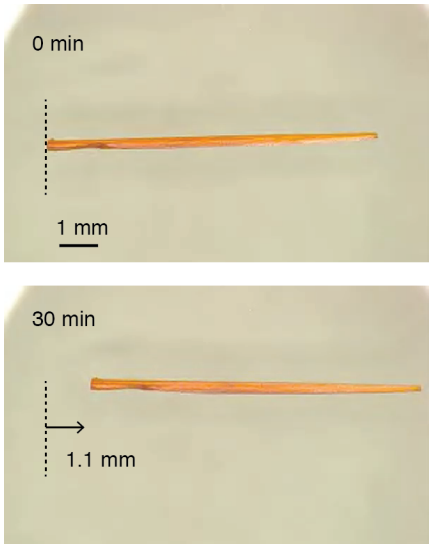

Figure 3.9 Inchworm-like walking on a glass without surface treatment. On a glass without surface treatment, the same crystal with Figure 3.7 moved 1.1 mm to the right direction in 30 min (walking speed 2.2 mm h^{-1}) under the same heating and cooling rate in Figure 3.7a, which was slower than the walking speed 3.0 mm h^{-1} on a silanized glass.

To check the relationship between the crystal shape and the motion, we observed walking motion of a shorter plate-like crystal (length 4.1 mm) with a thickness gradient, of which length and thickness were around half of the crystal (length 8.5 mm) in Figure 3.7 (Figure 3.10). When the shorter crystal was repeatedly heated and cooled on a silanized glass at the same temperature rate in Figure 3.7a, the crystal moved 0.89 mm in 30 min (walking speed 1.8 mm h^{-1}), giving around half speed of the longer crystal (walking speed 3.0 mm h^{-1}).

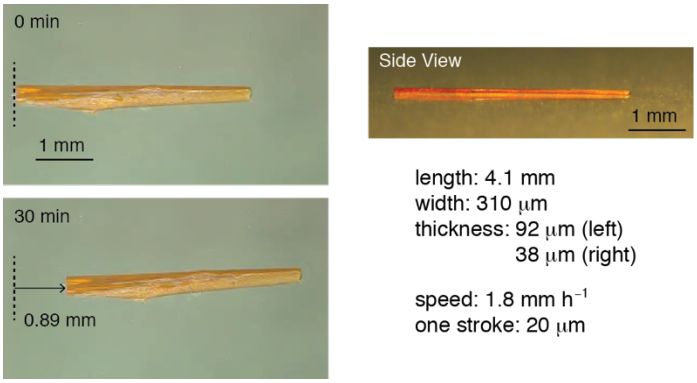

Figure 3.10 Inchworm-like walking of plate-like crystal with thickness gradient. A shorter plate-like crystal with a thickness gradient was heated and cooled on a silanized glass with the same temperature rate in Figure 3.7a. The crystal moved 0.89 mm in 30 min (walking speed 1.8 mm h^{-1}). The average one stroke was 20 μm.

3.3.5 Fast rolling locomotion

More surprisingly, the crystal rolled very fast under only one process of heating or cooling. When a long, thin plate-like crystal (length 9.6 mm × left width 115 μm and right width 210 μm × thickness 70 μm) with a width gradient was heated on a silanized glass from 134 to 147 °C (at 1 °C s^{-1}), the crystal began to bend with fluctuation at ~137 °C. Then, the crystal rolled with repeating flip at 141 °C, and finally stopped at ~142 °C (Figure 3.11a). The locomotion distance reached 3.7 mm in only 0.8 s; the speed was thus 4.6 mm s^{-1}. This rolling locomotion was much faster than inchworm-like walking.

In one process of cooling of the same crystal, similar rolling was observed as easily understood from the snapshots (Figure 3.11b). First, large bending occurred at ~140 °C; the bending was tilted, as detectable from the top view (28 ms, Figure 3.11b). This tilted bending lost the balance to rotate the crystal by 90°, returning to almost straight shape (44 ms, Figure 3.11b). Then, the first flip was completed by rotating another 90° due to momentum (52 ms, Figure 3.11b). Subsequently, a smaller second bending with some tilt occurred (68 ms, Figure 3.11b), and the crystal flipped again in a shorter time (28 ms) than the first flip (52 ms; at 80 ms, Figure 3.11b). After the second flip (first rolling), the crystal continued to roll without noticeable bending, taking, on average, 38 ms for each roll and reaching a distance of 3.1 mm after 192 ms, showing that the rolling speed 16 mm s^{-1} was approximately 20,000 times faster than that of the inchworm walk.

The snapshots taken from the slant upper side on cooling from 140 °C (at 1 °C s^{-1}) showed visually and more clearly the fast rolling locomotion. The first flip occurred in 30 ms, the second flip in 12 ms, and 5 consecutive rollings required, on average, 30 ms for each rolling (Figure 3.11c). The moving distance reached 3.5 mm in 204 ms (rolling speed 17 mm s^{-1}).

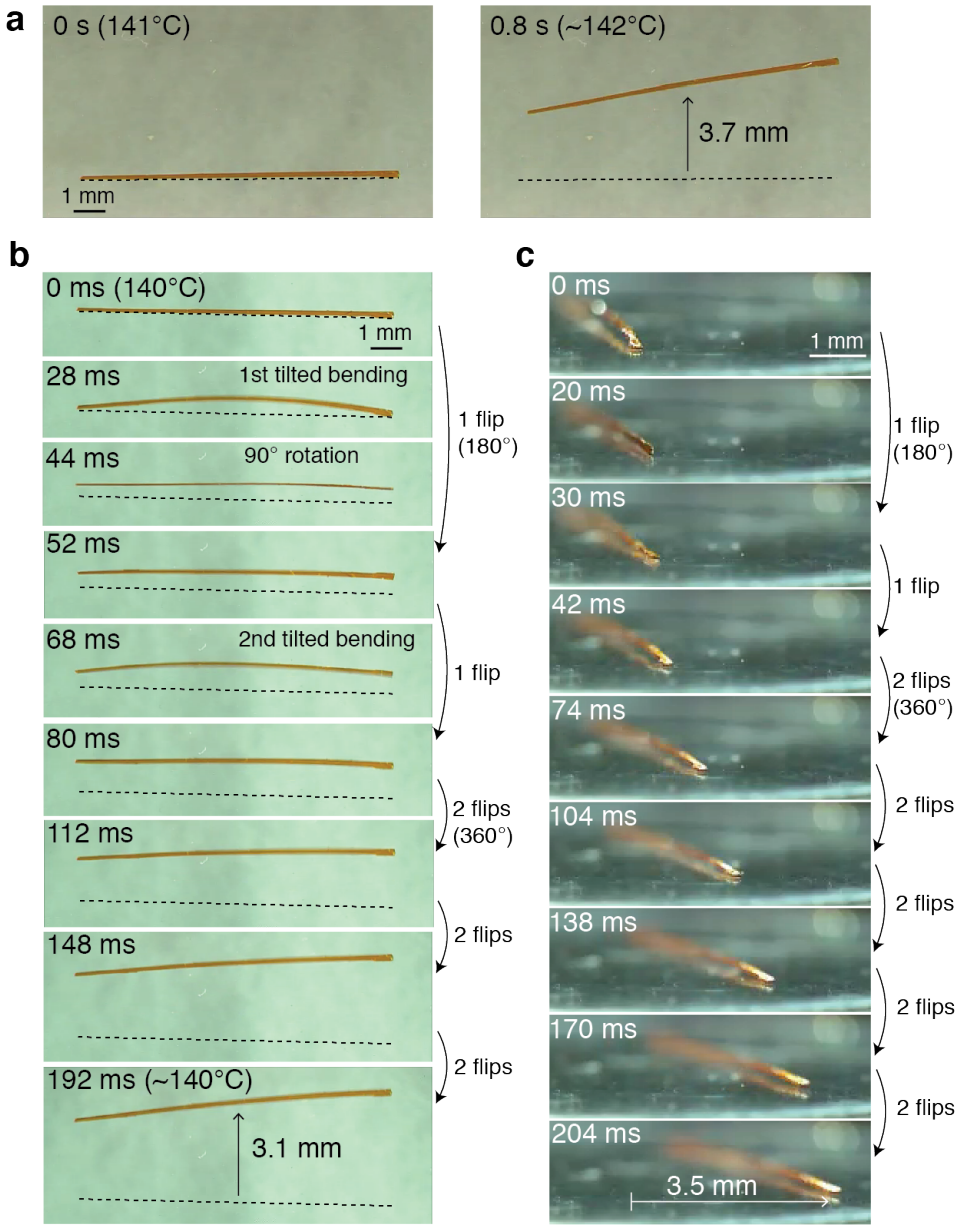

Figure 3.11 Fast rolling locomotion of a long, thin plate-like crystal. **a,** Rolling of a long, thin plate-like crystal with a width gradient on heating. **b,** Sequential snapshots during the rolling locomotion on cooling. Dotted lines indicate the initial position. **c,** Slant upper side view of rolling locomotion of the same crystal on cooling.

When the right and left of the crystal were reversed on the silanized glass under the same cooling condition, the crystal rolled to the lower direction, which was opposite to the direction in Figure 3.11b (Figure 3.12), suggesting that the direction of rolling locomotion depended on the unsymmetrical shape of the crystal. On a glass without surface treatment, the crystal rolled repeatedly and moved 4.1 mm in 256 ms (rolling speed: 16 mm s^{-1}) (Figure 3.13), showing similar speed (16 mm s^{-1}) on a silanized glass.

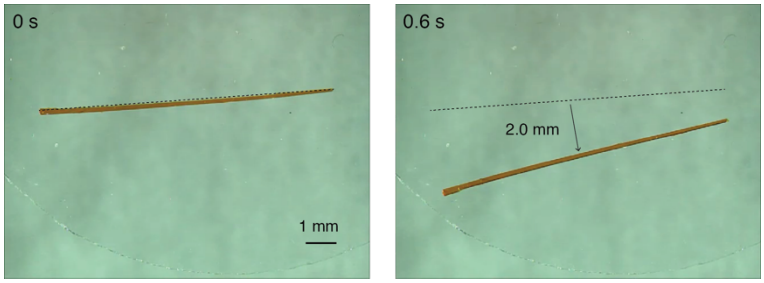

Figure 3.12 Fast rolling locomotion of a long, thin plate-like crystal on cooling. When the right and left of the crystal were reversed on a silanized glass with the same temperature condition, the crystal rolled to the lower direction, which was the opposite direction to that in Figure 3.11. The result suggests that the direction of rolling locomotion depends on the unsymmetrical crystal shape.

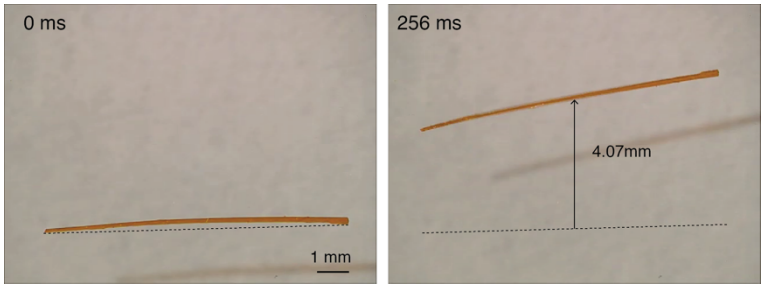

Figure 3.13 Fast rolling locomotion of a long, thin plate-like crystal on a glass without surface treatment upon heating. On a glass without surface treatment, the same crystal in Figure 3.11 flipped repeatedly and moved 4.1 mm in 256 ms (rolling speed: 16 mm s^{-1}).

The fast rolling locomotion was observed in several long, thin plate-like crystals of unsymmetrical shape (Figure 3.14). The crystals flipped to the direction where the angle of the crystal corner is an obtuse angle. In contrast, shorter, thicker crystals tended to move much more slowly, without rolling; the example is shown in Figure 3.15. A correlation diagram between crystal shape (length and thickness) and locomotion with and without rolling is illustrated in Figure 3.16. The crystals of aspect ratio (thickness/length) 0.002~0.008 caused flipping. In contrast, the crystals of that 0.006~0.027 did not flip. Namely, shorter, thicker crystals cannot flip due to the small bending.

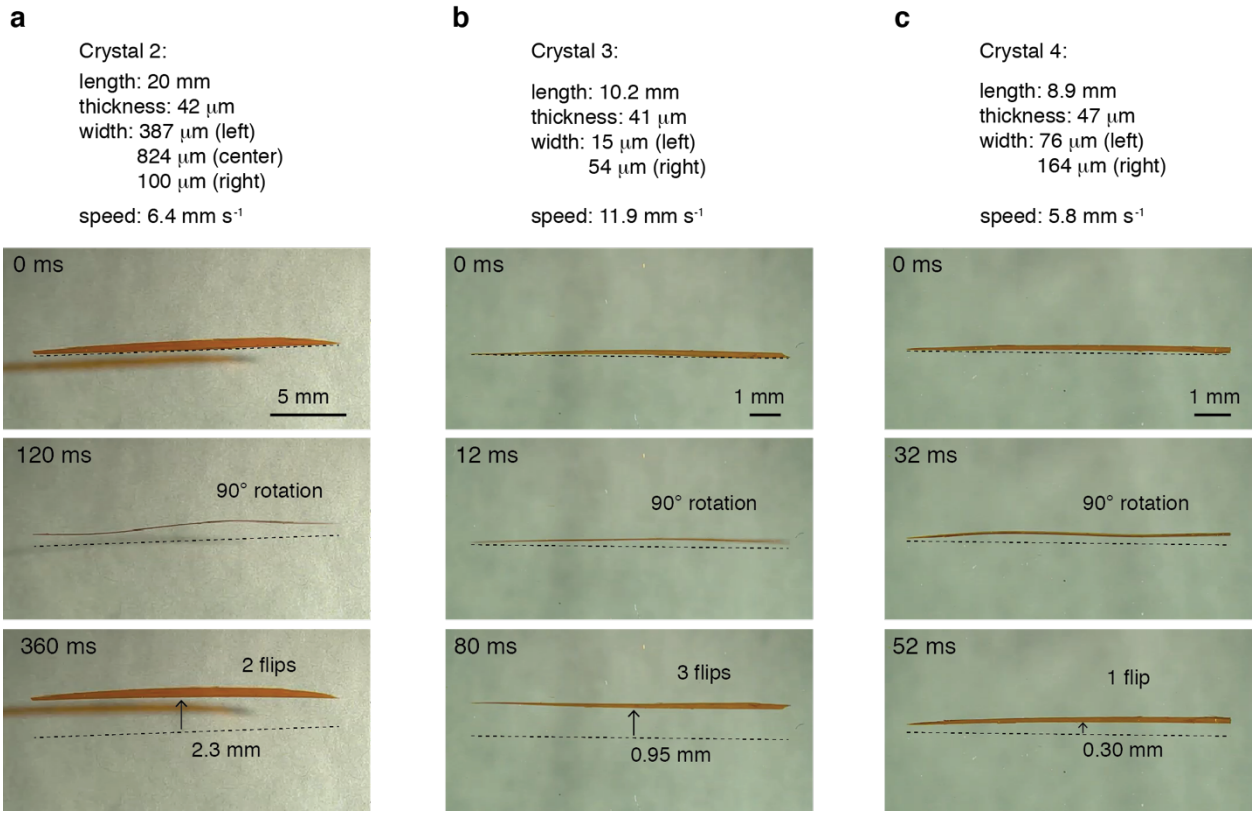

Figure 3.14 Fast rolling locomotion of long, thin plate-like crystals with unsymmetrical shape on cooling. Dotted lines indicate the initial position. Each crystal was numbered as the reference for Figure 3.16. Crystal 2 was observed on a glass without surface treatment, and crystals 3 and 4 were observed on silanized glass plates. The longer, wider crystal 2 needed longer time to cause the

flipping than those of the shorter, narrower crystals 3 and 4. The crystals flipped to the direction where the angle of the crystal corner is obtuse angle.

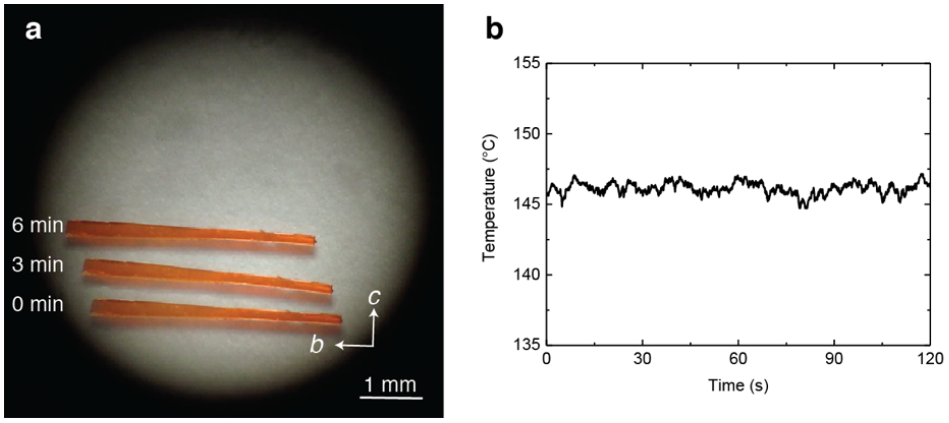

Figure 3.15 Slow locomotion of a short, thick plate-like crystal without rolling. **a,** Locomotion of a crystal (3990 × 240 × 108 μm^3) on a silanized glass by repeated heating and cooling near the transition point, 145°C. **b,** Temperature fluctuation of the silanized glass, measured with an IR thermometer. The crystal moved very slowly in a direction almost perpendicular to the long axis, with repeating the small bending and straightening; the moving distance was only 1.5 mm after 6 min (moving speed 0.0042 mm s^{-1}).

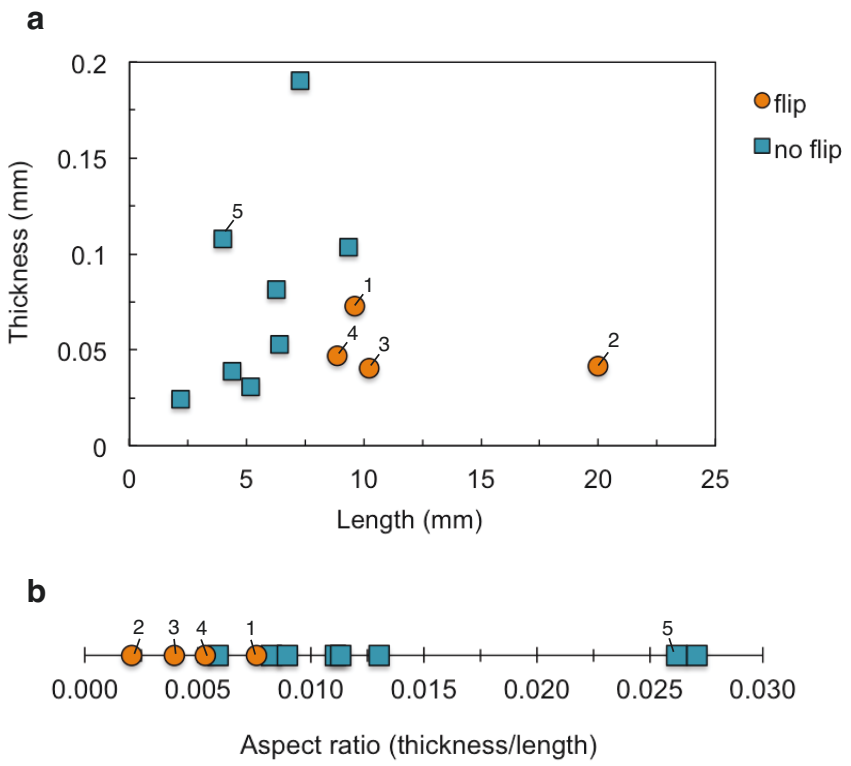

Figure 3.16 Relationship between crystal shape (length and thickness) and locomotion with and without rolling (**a**), and that between aspect ratio (thickness/length) and locomotion (**b**).

Numbers in the graph indicate different crystals.

1: the crystal in Figure 3.11, 3.12, and 3.13

2,3,4: the crystals in Figure 3.14

5: the crystal in Figure 3.15

The crystals of aspect ratio (thickness/length) 0.002~0.008 caused flipping. In contrast, the crystals of that 0.006~0.027 did not flip.

3.3.6 Locomotion mechanism

The schematic diagram of the possible mechanism of the inchworm-like walk is shown in Figure 3.17. On heating, a plate-like β-crystal with a thickness gradient bent due to the phase transition to the γ phase from the lower part (II, Figure 3.17a). The larger bending in the thicker left part necessarily leads to movement to the right. When the phase transition to the γ phase proceeded throughout the whole crystal, the thicker left part became suddenly straight, and simultaneously the thinner right edge was lifted up like a spring, due to the relaxation of some strain generated by suddenly finishing bending (III, Figure 3.17a).

On subsequent cooling, the thicker part started to bend again due to the phase transition from the γ to β phase near the crystal top surface due to cooling by the surrounding air (IV, Figure 3.17a). When the whole crystal had finished the phase transition to the β phase, the thinner right edge moved largely to the right, by slipping on the silanized glass surface (V, Figure 3.17a), because the thinner right part was lighter and thus the friction was less than in the thicker left part. In fact, the time profiles (Figure 3.8) support that the thicker left part moved largely during bending on heating, and then the thinner right edge moved largely on cooling, inducing the locomotion to the right, like an inchworm walk. The reason why the walking speed (2.2 mm h^{-1}) on a glass without surface treatment was slower than that (3.0 mm h^{-1}) on a silanized glass at the same heating and cooling rate, is most probably due to the stronger interaction between the hydrophilic glass surface and the crystal surface (Figure 3.7a and 3.9). Namely, the unsymmetrical crystal shape with the thickness gradient is the driving force of the inchworm-like walk.

A possible mechanism for the fast rolling locomotion is proposed (Figure 3.17b), based on the observations in Figure 3.10. When a long, thin plate-like crystal of the β phase is heated, the crystal bends with some tilt, due to the phase transition to the γ phase. The tilting autonomously

occurs by the unsymmetrical crystal shape with the width gradient, to the direction where the angle of the crystal corner is an obtuse angle, leading to loss of balance and the first flip; the incline of the center of gravity induces the driving force of the flipping. During the first flip, the whole crystal returns to the β phase due to cooling by the surrounding air. Then, the crystal turned inside out is again heated and bends with tilting due to the phase transition to the γ phase, to the direction where the angle of the crystal corner is acute angle likely due to the remaining momentum, leading to the second flip. When the whole crystal reaches the γ phase with further heating, the locomotion stops. Under cooling, the same explanation can be applied to the rolling locomotion (Figure 3.17b).

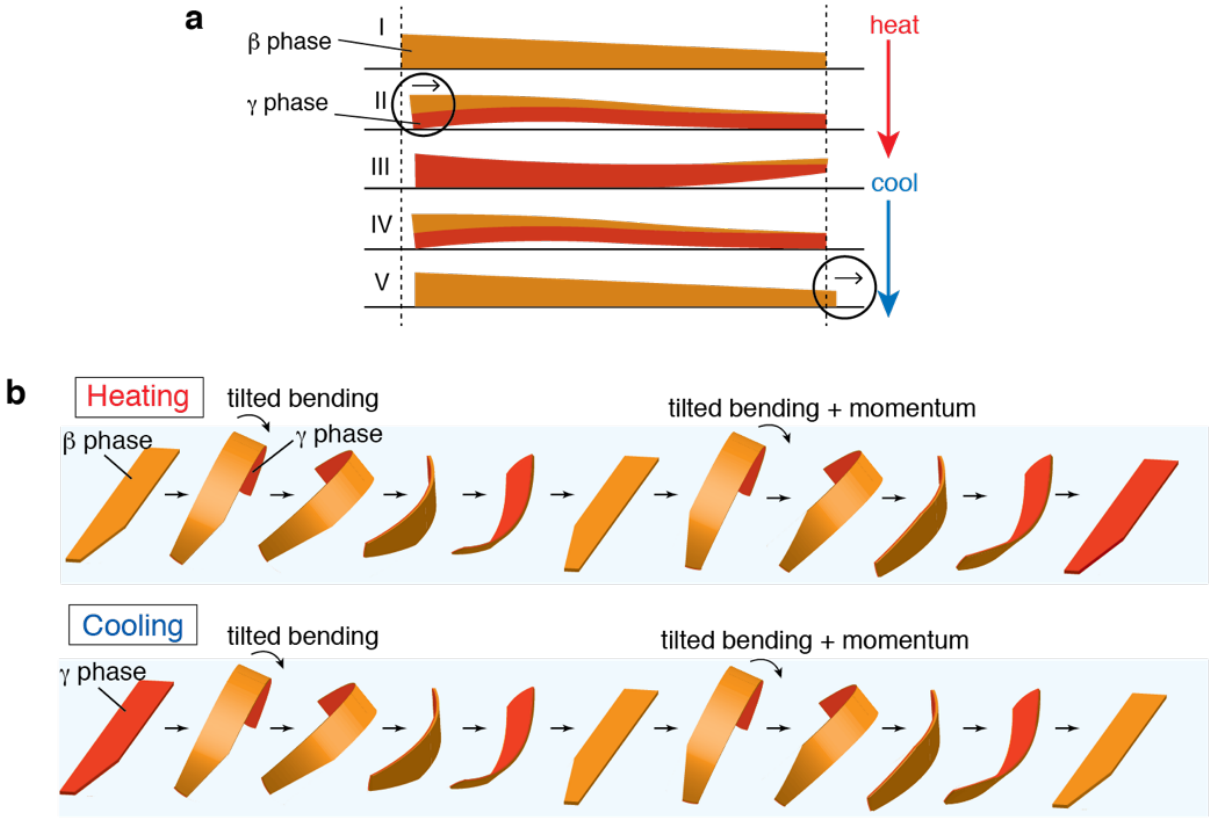

Figure 3.17 Schematic diagrams of the possible mechanisms of locomotion. **a,** Inchworm-like walking of a long crystal with a thickness gradient by repeated heating and cooling cycles. Displacement to the right is indicated by the circle. **b,** Rolling locomotion of a thin, long crystal with a width gradient under only one process of heating or cooling.

Finally, some mechanical properties were evaluated; Young's modulus of the β phase crystal, measured with a manual cantilever-bending test, showed 3.8 GPa (Figure 3.18), roughly comparable to several organic crystals.[18–20] The maximum strain and stress at the bending were estimated to be 0.48% (shrinkage) and 5.3 MPa, respectively (Figure 3.6b). The smooth following of the bending motion for the temperature change might be due to the small thermal hysteresis (2 °C) and the small enthalpy (1.3 kJ mol^{-1}) at the structural phase transition. During the bending and rolling, the plate-like crystal was elastic like a spring. The weak NH---O=C hydrogen bond chains in the β and γ crystals should contribute to the spring-like behavior. In summary, it is concluded that the driving force of both the directional locomotion, the inchworm-like walking and the fast rolling, is generated from the unsymmetrical shape of a crystal.

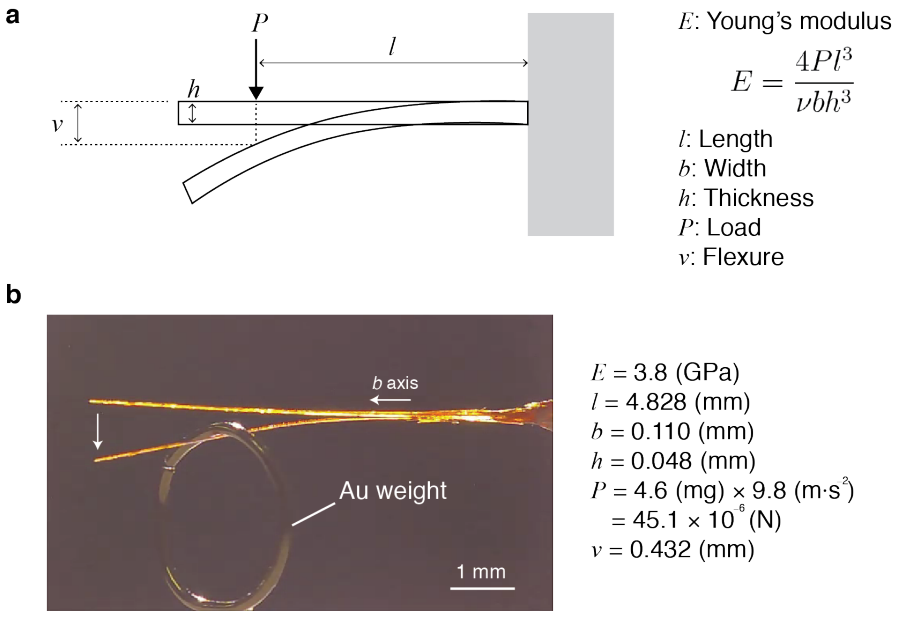

Figure 3.18 Cantilever-bending test to measure Young's modulus of the β-crystal. **a,** Schematic illustration of cantilever-bending test. **b,** Experimentally obtained data. A long plate-like crystal of *trans*-(*S*)-**1** (6889 × 110 × 48 μm^3) was fixed with glue at the right tip. A gold weight (4.6 mg) was placed manually on the (100) face of the crystal, and flexure was then measured. The picture shows before and after applying the load.

3.4 Conclusion

Long plate-like crystals with a thickness gradient in the longitudinal direction walk slowly, like an inchworm, by repeated bending and straightening under heating and cooling cycles near the transition temperature. Furthermore, thinner, longer plate-like crystals with a width gradient roll much faster by tilted bending and then flipping under only one process of heating or cooling. The length of the crystal is shortened above the transition temperature, which induces bending due to the temperature gradient to the thickness direction. The bending motion is necessarily converted to the walking and rolling locomotion due to the unsymmetrical shape of the crystal. This finding of the crystal locomotion can lead to a field of crystal robotics.

3.5 References

1. Maeda, S., Hara, Y., Sakai, T., Yoshida, R., Hashimoto, S. Self-walking gel. *Adv. Mater.* **19**, 3480–3484 (2007).
2. Yamada, M., Kondo, M., Miyasato, R., Naka, Y., Mamiya, J., Kinoshita, M., Shishido, A., Yu, Y., Barrett, C. J., Ikeda, T. Photomobile polymer materials - various three-dimensional movements. *J. Mater. Chem.* **19**, 60–62 (2009).
3. Kohlmeyer, R. R., Chen, J. Wavelength-selective, IR light-driven hinges based on liquid crystalline elastomer composites. *Angew. Chem. Int. Ed.* **52**, 9234–9237 (2013).
4. Wie, J. J., Shankar, M. R., White, T. J. Photomotility of polymers. *Nat. Commun*. **7**, 13260 (2016).
5. Gelebart, A. H., Mulder, D. J., Varga, M., Konya, A., Vantomme, G., Meijer, E. W., Selinger, R. L. B., Broer, D. J. Making waves in a photoactive polymer film. *Nature* **546**, 632–636 (2017).
6. Ge, F., Zhao, Y. A new function for thermal phase transition-based polymer actuators: autonomous motion on a surface of constant temperature. *Chem. Sci.* **8**, 6307–6312 (2017).
7. Dong, L., Tong, X., Zhang, H., Chen, M., Zhao, Y. Near-infrared light-driven locomotion of a liquid crystal polymer trilayer actuator. *Mater. Chem. Front.* **2**, 1383–1388 (2018).
8. Hu, W., Lum, G. Z., Mastrangeli, M., Sitti, M. Small-scale soft-bodied robot with multimodal locomotion. *Nature* **554**, 81–85 (2018).
9. Uchida, E., Azumi, R., Norikane, Y. Light-induced crawling of crystals on a glass surface. *Nat. Commun.* **6**, 7310 (2015).
10. Rus, D., Tolley, M. T. Design, fabrication and control of soft robots. *Nature* **521**, 467–475 (2015).

11. Taniguchi, T., Fujisawa, J., Shiro, M., Koshima, H., Asahi, T. Mechanical motion of chiral azobenzene crystals with twisting upon photoirradiation. *Chem. Eur. J.* **22**, 7950–7958 (2016).
12. Katritzky, A. R., He, H. Y., Suzuki, K. *N*-Acylbenzotriazoles: neutral acylating reagents for the preparation of primary, secondary, and tertiary amides. *J. Org. Chem*. **65**, 8210–8213 (2000).
13. Katritzky, A. R., Chen, Q. Y., Tala, S. R. Convenient preparations of azo-dye labeled amino acids and amines. *Org. Biomol. Chem.* **6**, 2400–2404 (2008).
14. Sheldrick, G. M. A short history of SHELX. *Acta Crystallogr*. A **64**, 112–122 (2008).
15. CrystalStructure v.4. 2. 2 (Rigaku Corporation, Tokyo, Japan, 2016).
16. Hübschle, C. B., Sheldrick, G. M., Dittrich, B. ShelXle: a Qt graphical user interface for SHELXL. *J. Appl. Cryst.* **44**, 1281–1284 (2011).
17. POV-Ray v.3. 7. 0 (Persistence of Vision Raytracer Pty. Ltd., Victoria, Australia, 2013).
18. Danno, T., Kajiwara, T., Inokuchi, H. Dynamic mechanical behaviour of organic molecular crystals. I. *Bull. Chem. Soc. Jpn*. **40**, 2793–2795 (1967).
19. Morimoto, M., Irie, M. A diarylethene cocrystal that converts light into mechanical work. *J. Am. Chem. Soc.* **132**, 14172–14178 (2010).
20. Koshima, H., Matsuo, R., Matsudomi, M., Uemura, Y., Shiro, M. Light-driven bending crystals of salicylidenephenylethylamines in enantiomeric and racemic forms. *Cryst. Growth Des.* **13**, 4330–4337 (2013).

Chapter 4

Photo-triggered phase transition and stepwise bending

4.1 Introduction

As described in chapters 2 and 3, I have found that chiral azobenzene crystal bends with twisting upon photoirradiation,[1] and that walks or rolls on a glass plate upon heating and cooling due to the structural phase transition at 145 °C.[2] From these findings, I come up with an idea that a crystal will exhibit several actuation patterns by a combination of photoisomerization and structural phase transition if both phenomena undergo in the crystal. In fact, it is reported that a diarylethene crystal exhibits a unique bending behavior induced by photochromic reaction and phase transition.[3] However, the phase transition temperature of chiral azobenzene crystal is relatively high for the manipulation at experiment and application. Thus, there was a need to find a structural phase transition of a new photo-responsive crystal.

Here, I clarify the importance to find a structural phase transition. It is well known that structural phase transitions control not only actuation but also other physical properties of the solid induced by external stimuli such as temperature, pressure, electromagnetic fields, and light. For instance, ferroelectrics and ferromagnets undergo the structural phase transition at the material-specific Curie temperature, and significantly change the electrical and magnetic behaviors.[4–7] Shape memory alloys exhibit the shape recovering effect due to martensitic transition upon heating.[8,9] Photo-induced phase transition is known that a new crystal phase appears by light irradiation and changes electrical and magnetic properties very rapidly.[10–13] In addition, other external stimuli such as electromagnetic fields and solvents also induce structural phase transition.[14–16] The phase transition mechanisms are widely utilized in memory, switch, and actuation materials.[17,18] Thus, the discovery of a structural phase transition has great potential to expand both academic and application fields.

This chapter describes photo-triggered phase transition and stepwise bending of a photochromic crystal. The photo-triggered phase transition, which is different from previously known structural phase transitions, is discovered in the crystal of (*S*)-*N*-3,5-*di*-*tert*-butylsalicylidene-1-(1-naphthyl)ethylamine in the enol form [enol-(*S*)-**2**], which undergoes enol–keto photoisomerization (Figure 4.1). The enol-(*S*)-**2** crystal exhibits structural phase transition between trimorphic α, β, and γ phases due to temperature change. Upon ultraviolet (UV) light irradiation, the crystal at β phase changes to the γ phase due to the photo-triggered phase transition. The γ phase achieved by the photo-triggered phase transition forms a unique molecular conformation that cannot be reached by thermal phase transition. The manifestation mechanism of the photo-triggered phase transition is considered to originate from the strain due to the *trans*-keto molecules produced by photoisomerization. The photo-triggered phase transition enables thin enol-(*S*)-**2** crystals to bend in stepwise by only light irradiation. This finding of photo-triggered phase transition has the potential to extend functions of photo-responsive solid materials as a new phase transition mechanism.

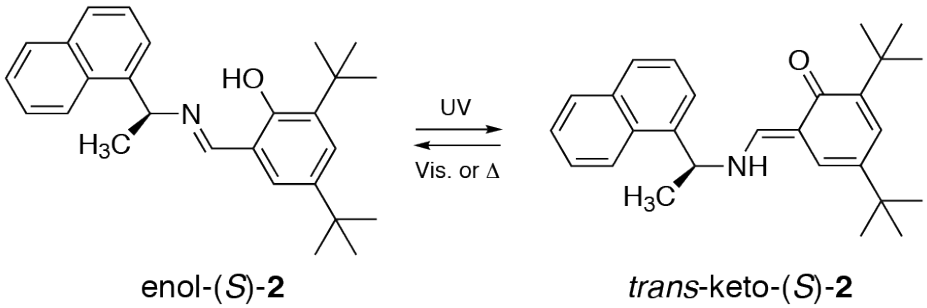

Figure 4.1 Enol–keto photoisomerization of salicylidenenaphthylethylamine enol-(*S*)-**2**.

4.2 Experimental section

4.2.1 Material preparation.

Enol-(*S*)-**2** compound was synthesized using a microwave (Monowave 300, Anton Paar) according to the literature.[19] Plate-like single crystals of enol-(*S*)-**2** were obtained by evaporation of 2-propanol or acetonitrile solution at ambient temperature.

4.2.2 Thermal analysis.

DSC measurements were performed with a differential scanning calorimeter (Thermo plus EVO2 DSCvesta, Rigaku) at a speed of 5 °C min^{-1} in the temperature range from −100 °C to 60 °C. Another calorimeter (DSC 8500, PerkinElmer) was also employed for measurements in the range of 30–130 °C. The molar transition enthalpy ΔH was calculated based on the peak area in DSC curve from the baseline.

4.2.3 UV-vis absorption measurement.

Absorption spectra of an enol-(*S*)-**2** crystal were measured with a transmittance method.[20] A thin plate-like crystal prepared by solvent evaporation was fixed on a Cu plate with a pinhole of diameter approximately 0.5 mm. Transmitted light intensity through the sample was measured between 250–680 nm at 2 nm resolution. Transmitted light intensity through the Cu plate without sample was also measured in the same wavelength range for blank. UV-vis absorption spectra were calculated according to the Beer-Lambert-Bouguer law, and then divided by crystal thickness to obtain absorption coefficient for standardization. Sample temperature was regulated by Peltier thermostat. Diffuse reflectance spectrometer (Lambda 650, PerkinElmer) was also employed to measure spectral behavior upon visible light irradiation (λ = 488 nm, FOLS-2, Sawaki Kobo).

4.2.4 X-ray crystallographic analysis.

Single-crystal XRD data of enol-(*S*)-**2** crystals without UV light at variant temperatures were collected using an R-AXIS RAPID diffractometer (Rigaku) equipped with monochromatic Mo-Kα radiation (λ = 0.71075 Å) at 50 kV and 40 mA. The temperature of the sample was regulated using an N_2 gas flow cryostat and calibrated with a thermocouple. Unit cell parameters before, under, and after UV light irradiation were also measured with this apparatus. The light irradiation was performed by UV-LED lamp (λ =365 nm, UV-400, Keyence) and LD light source (λ =488 nm, FOLS-2, Sawaki Kobo). Crystal structures before and under UV light irradiation at −50 and 50 °C were determined by using a XtaLAB Synergy diffractometer (Rigaku) equipped with monochromatic Cu-Ka radiation (λ = 1.54187 Å). The crystal structures were solved using a direct method with SHELXS2013[21] or SHELXD2013[21], and then refined on F^2 using the full-matrix least-squares method of SHELXL[21]. Calculations were performed using the Rigaku crystal structure software package[22] and a graphical interface, ShelXle[23].

4.2.5 Observation of transformation and bending behavior of crystals.

Shape change upon heating and cooling was observed using a temperature control stage (Japan High Tech) and a digital high-speed microscope (VHX-500, Keyence). Shape change and bending behavior of enol-(*S*)-**2** crystals upon UV light irradiation (λ =365 nm, UV-400, Keyence) were observed at room temperature using the digital high-speed microscope. Surface temperature change upon UV light irradiation was measured with an IR thermography camera (FSV-2000, Apiste) in a super dry room. The substrate temperature of the glass plate was regulated with a Peltier thermo-controller (Tokai Hit).

4.3 Results and Discussion

4.3.1 Thermal phase transition

Differential scanning calorimetry (DSC) measurement of enol-(*S*)-**2** crystals was performed in the temperature range from −100 °C to 60 °C at a rate of 5 °C min^{-1} with heating and then cooling (Figure 4.2). On heating, the DSC curve showed two endothermic peaks at −72.5 and 39.6 °C with the enthalpies ΔH of 1.23 and 0.20 kJ mol^{-1}, respectively. On subsequent cooling, the DSC curve also had two exothermic peaks at −81.1 and 31.9 °C with the enthalpies ΔH of −1.03 and −0.24 kJ mol^{-1}, respectively. The thermal hysteresis of each phase transition was 8.6 °C at the low-temperature phase transition α ↔ β, and 7.7 °C at the high-temperature phase transition β ↔ γ. The enthalpy at the phase transition β ↔ γ was approximately one-fifth of that at the transition α ↔ β, both of which were much smaller than that required for melting (ΔH = 20.0 kJ mol^{-1}).

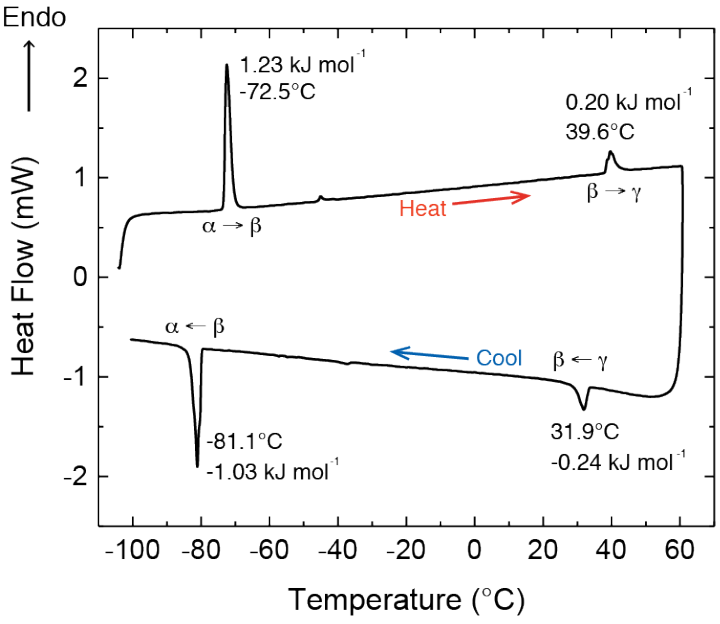

Figure 4.2 DSC measurement of enol-(*S*)-**2** crystals. Differential scanning calorimetry (DSC) curve measured in the temperature range from −100 °C to 60 °C at a rate of 5 °C min^{-1} on heating and subsequent cooling.

X-ray crystallographic analyses of an enol-(*S*)-**2** crystal were performed at variant temperatures in the range from −100 °C to 60 °C, verifying the reversible phase transitions between α, β, and γ phases (Figure 4.3 and Table 4.1). The crystal structures at α and β phases belonged to the same space group *P*1. Due to the low-temperature phase transition α → β, lengths of *a*- and *c*-axes changed by +1.8 and −1.3% (Figure 4.3a, c), and the α, β, and γ angles decreased by 9°, 5°, and 2.5°, respectively (Figure 4.3d–f). In contrast to the α and β phases, the crystal structure at γ phase belonged to the space group $P2_1$. Although lengths of *a*-, *b*-, and *c*-axes changed very slightly, +0.5, −0.05, and +0.2%, respectively (Figure 4.3a–c), lattice angles changed more clearly; α and γ angles became 90° due to crystal system change from triclinic to monoclinic, and β angle changed by +10° at the high-temperature phase transition β → γ (Figure 4.3d–f).

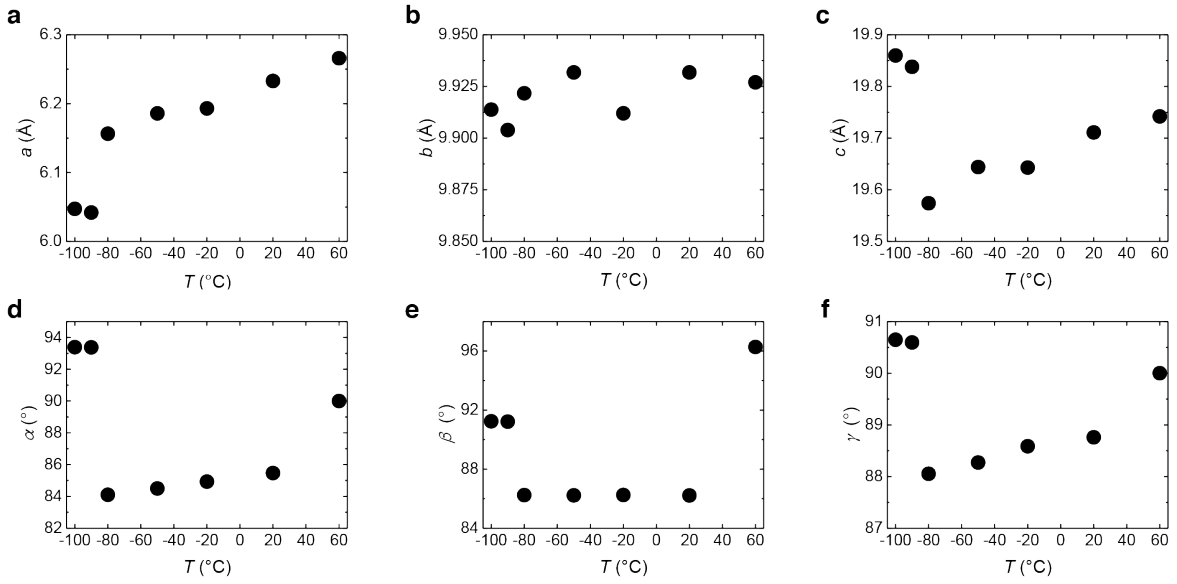

Figure 4.3 Crystal structures of enol-(*S*)-**2** crystal at variant temperatures. **a–f,** Unit cell parameters of (**a**) *a*, (**b**) *b*, (**c**) *c* axes, (**d**) α, (**e**) β, and (**f**) γ angles.

Table 4.1 Crystallographic parameters depending on temperature.

Temp. / °C	−100 (α)	−90 (α)	−80 (β)	−50 (β)	−20 (β)	20 (β)	60 (γ)
Crystal system	Triclinic	Triclinic	Triclinic	Triclinic	Triclinic	Triclinic	Monoclinic
Space group	*P*1	*P*1	*P*1	*P*1	*P*1	*P*1	$P2_1$
a / Å	6.0473(9)	6.0427(8)	6.1564(8)	6.1859(8)	6.1931(10)	6.2330(12)	6.266(2)
b / Å	9.9138(14)	9.9039(11)	9.9217(10)	9.9318(12)	9.9120(13)	9.9318(17)	9.927(3)
c / Å	19.860(3)	19.838(2)	19.574(2)	19.644(3)	19.643(3)	19.711(4)	19.742(6)
α / °	93.385(7)	93.375(7)	84.099(6)	84.496(6)	84.930(6)	85.466(6)	90
β / °	91.242(6)	91.219(6)	86.241(6)	86.226(6)	86.249(6)	86.216(6)	96.276(8)
γ / °	90.647(6)	90.595(6)	88.053(6)	88.270(6)	88.586(6)	88.759(6)	90
V / Å^3	1188.2(3)	1184.8(2)	1186.3(2)	1198.4(3)	1198.3(3)	1213.6(4)	1220.7(6)
Z	2	2	2	2	2	2	2
ρ_{calc} / g·cm^{-3}	1.083	1.086	1.085	1.074	1.074	1.061	1.054
R_1 [$I > 2\sigma(I)$]	0.0588	0.0550	0.0488	0.0508	0.0538	0.593	0.0526
wR_2 [$I > 2\sigma(I)$]	0.1763	0.1520	0.1380	0.1436	0.1761	0.1719	0.1435
GOF	1.054	1.047	0.905	1.045	0.805	1.127	0.902

In order to compare molecular conformation between α, β, and γ phases, independent molecules in a unit cell at each phase are shown (Figure 4.4a–f). Two independent molecules drawn in green and yellow exist in a lattice at α phase (Figure 4.4a, d). Here, we call these molecules as molecule 1 (green) and molecule 2 (yellow). Molecules 1 and 2 form slightly different dihedral angles between salicylidene and naphthyl planes, of 54.54° and 52.71° at −90 °C (Figure 4.4g). *Tert*-butyl substituent groups of molecules 1 and 2 at α phase are not disordered, forming conformation A drawn in magenta (Figure 4.4a, d, h).

The molecules 1 and 2 at β phase became different conformation from those at α phase due to the transition α → β (Figure 4.4b, e). At −80 °C, the dihedral angles of molecules 1 and 2 were 47.78° and 48.26°, respectively (Figure 4.4g). Both of them continuously decreased to 46.40° and 47.58°, respectively, with the increase of temperature to 20 °C (Figure 4.4g). Another difference from α phase is that *tert*-butyl substituent groups of molecules 1 and 2 at β phase are disordered with two conformations A (magenta) and B (blue) (Figure 4.4b). The conformation B is the orientation rotating almost 60° from conformation A. The different orientations of *tert*-butyl substituent groups in molecules 1 and 2 can be clearly seen from the view parallel to the salicylidene plane (Figure 4.4e). As to the occupancy of the disordered *tert*-butyl group, the conformation A is major for molecule 1, and in contrast, the conformation B is major for molecule 2 at β phase (Figure 4.4e). The occupancy of conformation A continuously decreased for molecule 1, and increased for molecule 2 with temperature rise at β phase (Figure 4.4h).

At γ phase, one independent molecule exists in a lattice (Figure 4.4c, f). The independent molecule forms the dihedral angle of 46.49° and has conformation A as major occupancy for the disordered *tert*-butyl group (Figure 4.4g, h). This molecular conformation at γ phase is relatively similar to the molecule 1 at β phase, suggesting that the conformation of molecule 2 at β phase changed to the same conformation with molecule 1 due to the phase transition β → γ.

Although there were distinct differences in molecular conformations between α, β, and γ phases, molecular arrangements were very similar (Figure 4.5). Molecular packings on (100) face at α, β, and γ phases show that the phase transitions α ↔ β and β ↔ γ process with slight displacement of each molecule along the *b* axis, inducing the change of α angle (Figure 4.5a). The molecular packings on (010) and (001) faces were also similar between three phases (Figure 4.5b,c). This similarity of molecular arrangements between α, β, and γ phases affords structural

phase transitions α ↔ β and β ↔ γ with the small transition enthalpies. Due to the structural phase transitions, a plate-like crystal viewed from (010) face deformed reversibly without any disintegration upon heating and cooling (Figure 4.6).

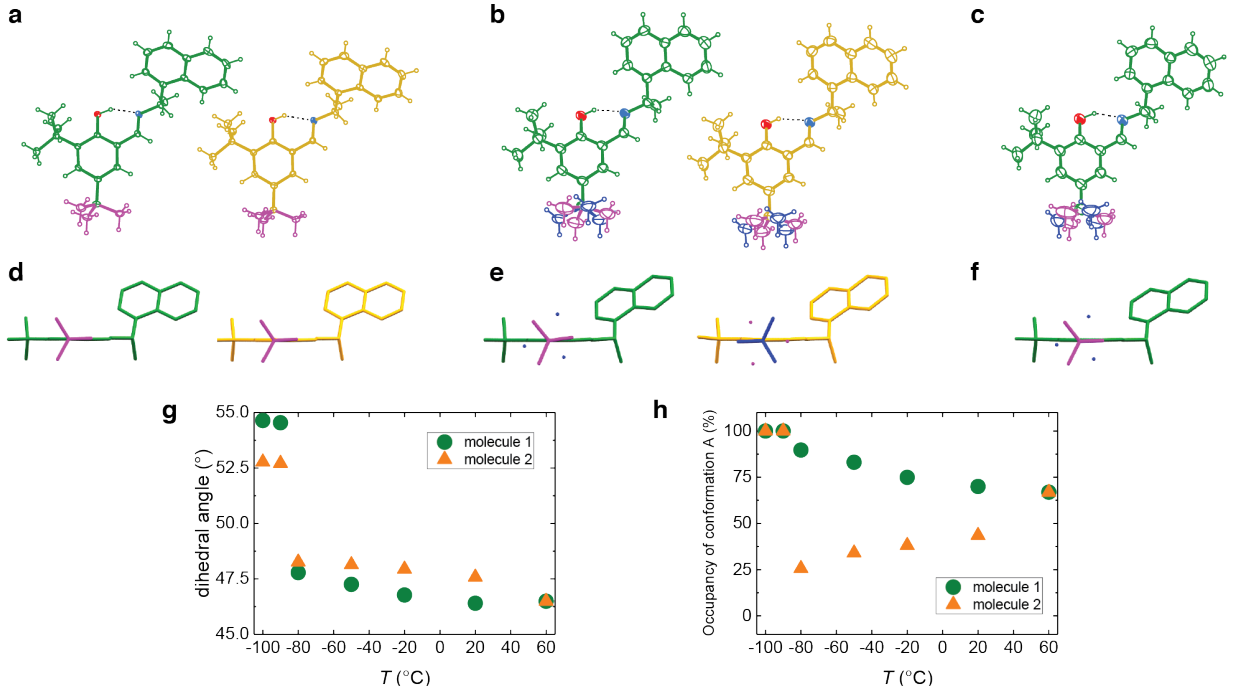

Figure 4.4 Molecular conformations of independent molecules at (**a,d**) α, (**b,e**) β, and (**c,f**) γ phases. **a–c,** The ORTEP figures are drawn by thermal ellipsoids with 25% probability. Two independent molecules at α and β phases are shown in green (molecule 1) and yellow (molecule 2), and an independent molecule at γ phase is drawn in green due to the similarity to molecule 1. The conformations of disordered *tert*-butyl substituents are shown in magenta (conformation A) and blue (conformation B). **d–f,** Molecular conformations viewing parallel to the salicylidene plane. Hydrogen atoms and *tert*-butyl bonds with minor occupancy are omitted for clarity. **g,** Dihedral angle between naphthyl plane and salicylidene plane. **h,** Occupancy of conformation A of disordered *tert*-butyl substituents.

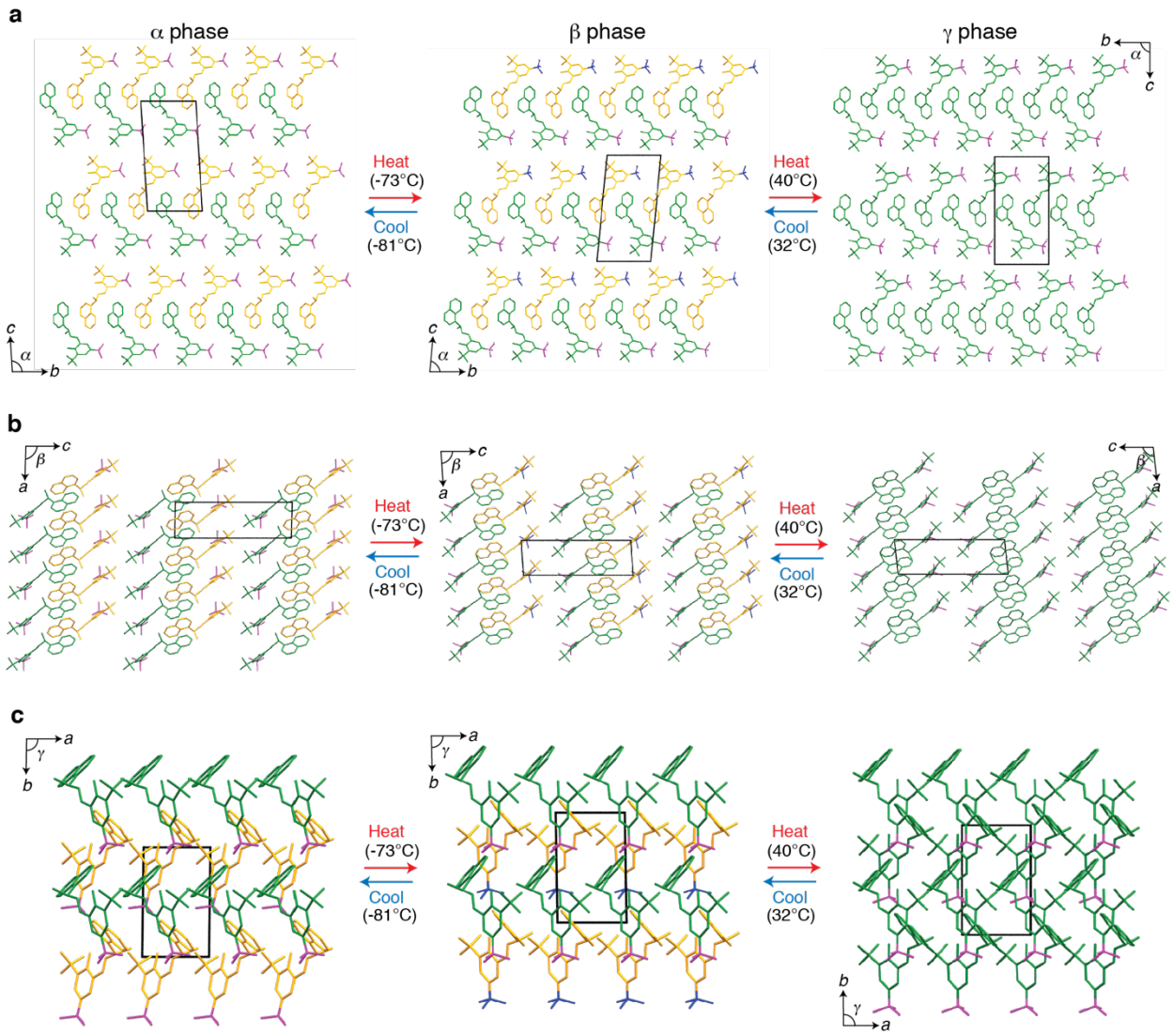

Figure 4.5 Molecular arrangements at α, β, and γ phases. **a,** (100) plane views. **b,** (010) or $(0\bar{1}0)$ plane views. **c,** (001) or $(00\bar{1})$ plane views. Disordered *tert*-butyl substituents with minor occupancies and hydrogen atoms are omitted for clarity.

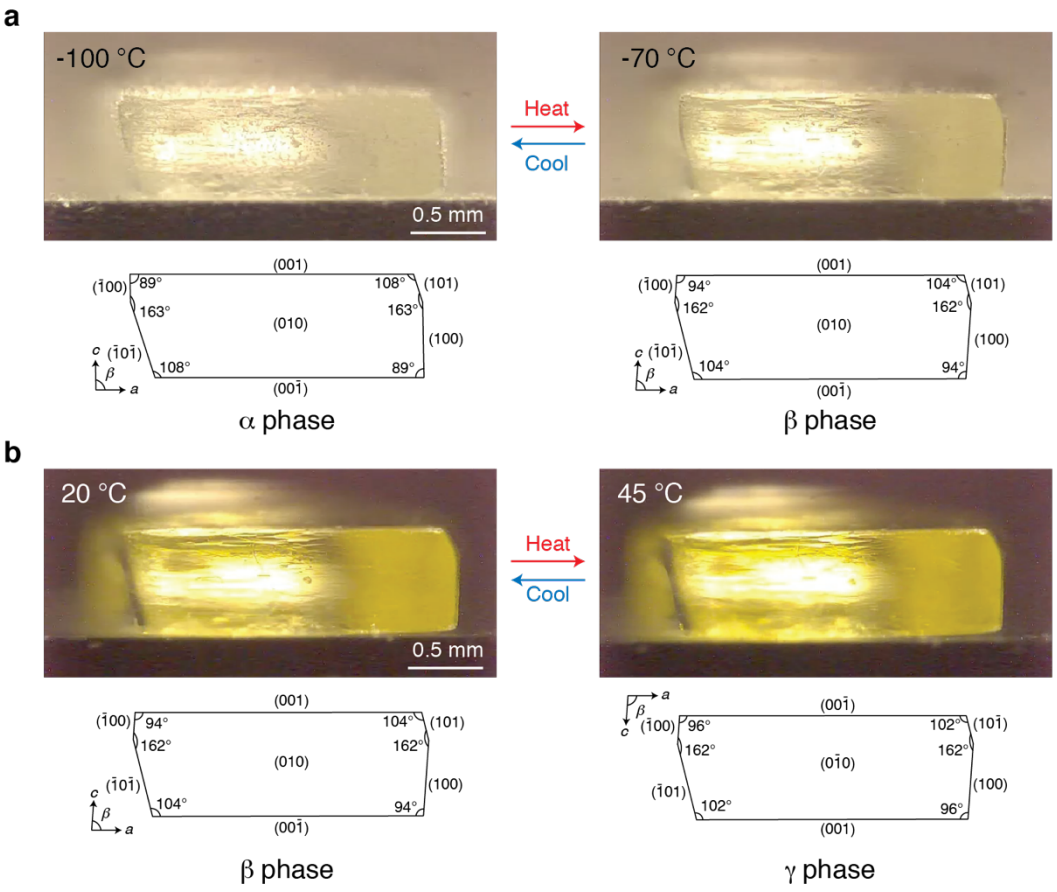

Figure 4.6 Shape change upon heating and cooling. **a,** Reversible transformation due to the phase transition α ↔ β upon heating and cooling in the range from −100 °C to −70 °C. **b,** Reversible transformation due to the phase transition β ↔ γ upon heating and cooling in the range of 20–45 °C.

4.3.2 Photoisomerization

UV-vis absorption spectra were measured with a transmittance method to reveal the photochromic nature of an enol-(*S*)-**2** crystal (20 μm thick) at β and γ phases. Without UV light irradiation at 20 °C, the spectrum of the crystal at β phase had a large peak at 300 nm, and almost no absorption above 400 nm (Figure 4.7a). Upon weak UV light irradiation (365 nm, 5 mW cm^{-2}), a new peak appeared at 450 nm due to photoisomerization from enol form to *trans*-keto form, accompanying crystal color change from yellow into orange (Figure 4.7a). The difference spectrum, which was obtained by subtracting the spectrum before UV irradiation from that under UV irradiation, clarified that the absorption increased in the range of 375–550 nm with the peak wavelength at 450 nm (Figure 4.7c). The half-life of the thermal relaxation from *trans*-keto form to enol form was calculated to be 86.2 s based on the decay curve of the peak intensity at 450 nm after stopping UV irradiation (Figure 4.7d). The half-life of back-photoisomerization from *trans*-keto to enol form by visible light (488 nm, 1.4 mW cm^{-2}) was calculated to be 9.9 s using a diffuse reflectance spectrometer (Figure 4.8). The spectral behavior indicates that back-photoisomerization processes much faster than thermal back-isomerization.

At 50 °C, the spectrum of the crystal at γ phase under UV irradiation did not almost change from that before UV irradiation (Figure 4.7b). Although the difference spectrum was also not noticeable to identify a new peak in the range of 375–550 nm, the time dependence at 450 nm indicated that absorption intensity upon UV irradiation increased very slightly from that before UV light, suggesting enol to *trans*-keto photoisomerization with considerably lower conversion at γ phase than that at β phase (Figure 4.7c, d).

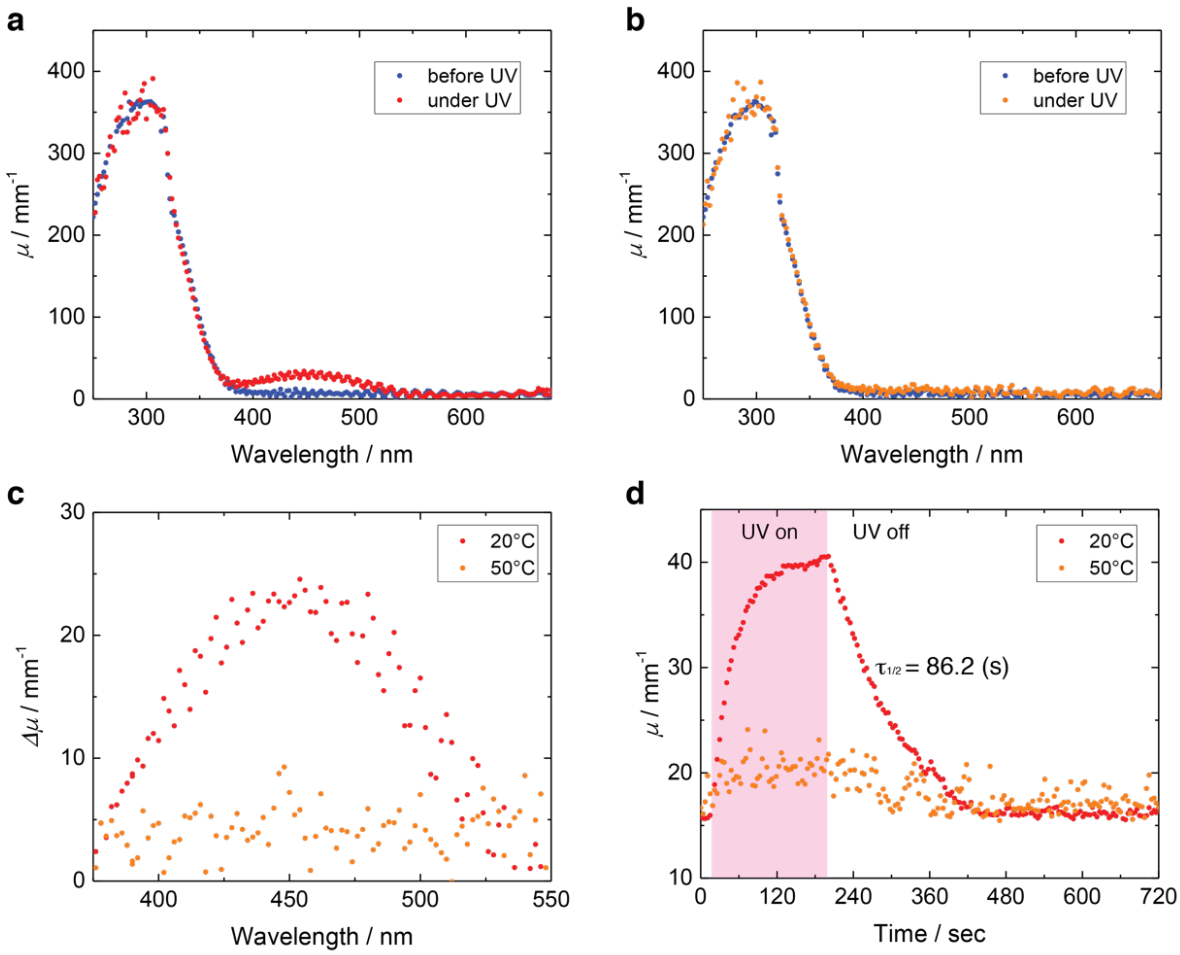

Figure 4.7 a,b, UV-vis absorption spectra of a enol-(*S*)-**2** crystal (thickness: 20 μm) on the (001) top face before and under UV light (365 nm, 5 mW cm^{-2}) irradiation at (**a**) 20, and (**b**) 50 °C. **c,** Difference spectra at 20 and 50 °C obtained by subtracting the spectrum before UV light irradiation from the spectrum under UV light irradiation. **d,** Time dependence of the absorption at 450 nm on and off UV light irradiation at 20 and 50 °C. In each panel, the absorption was expressed in absorption coefficient for normalization.

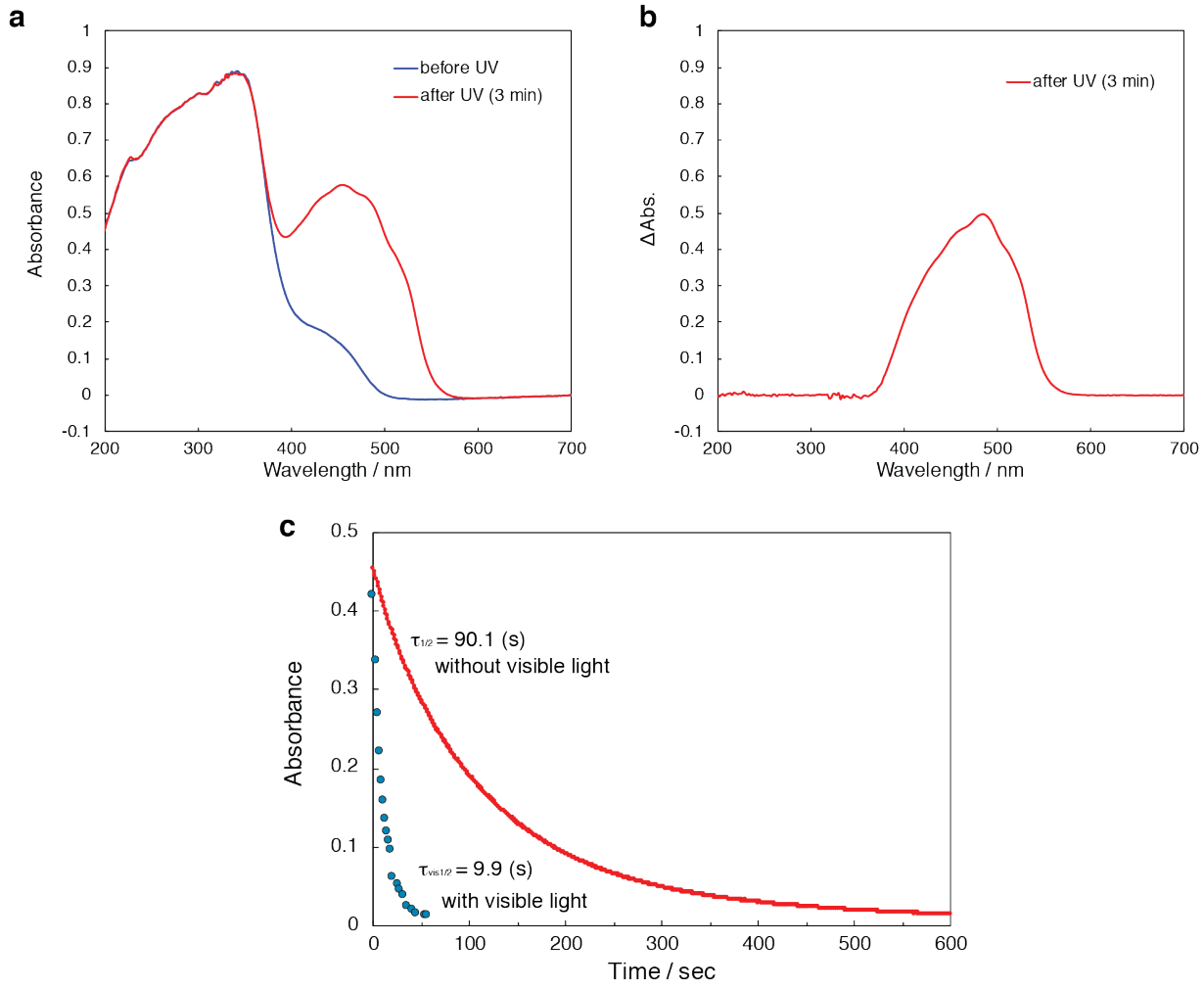

Figure 4.8 Diffuse reflectance spectra of enol-(*S*)-**2** crystals at 20 °C. **a,** Diffuse reflectance spectra before and after UV light irradiation. **b,** Difference spectrum subtracting the spectrum before UV light from that after UV light. **c,** Time dependence of the absorption change at 520 nm after stopping UV irradiation. After stopping UV irradiation, the absorption at 520 nm continuously decreased due to thermal back-isomerization with the half-life of 90.1 s, which is almost same with that obtained by a transmittance method. By visible light (488 nm, 1.4 mW cm^{-2}) irradiation, the absorption at 520 nm decreased much faster due to back-photoisomerization with the half-life of 9.9 s. The scan wavelength 520 nm was selected to avoid contamination with 488 nm visible light.

4.3.3 Photo-triggered phase transition

Surprisingly, when unit cell parameters of an enol-(*S*)-**2** crystal (0.4 × 0.4 × 0.08 mm^3) were measured during UV irradiation (365 nm, 60 mW cm^{-2}), the unit cell at β phase changed to that at γ phase (Figure 4.9). Here, the change of α angle is described as an indicator of photo-triggered phase transition because the α angle changes the most at the transition α → β and becomes 90° at the transition β → γ. The α angle at β phase changed into 90° under UV irradiation at variant temperatures of −50, −20, 0, and 20 °C (Fig. 6a). In contrast to the change at β phase, the α angle measured at −120 °C (α phase) and 60 °C (γ phase) did not change under UV irradiation (Figure 4.9a). The β and γ angles also became the angles corresponding to γ phase, accompanying slight length change of *a*-, *b*-, and *c*-axes (Figure 4.9b). These results suggest that UV light irradiation triggers the phase transition from β to γ phase but does not trigger the phase transition from α to β phase.

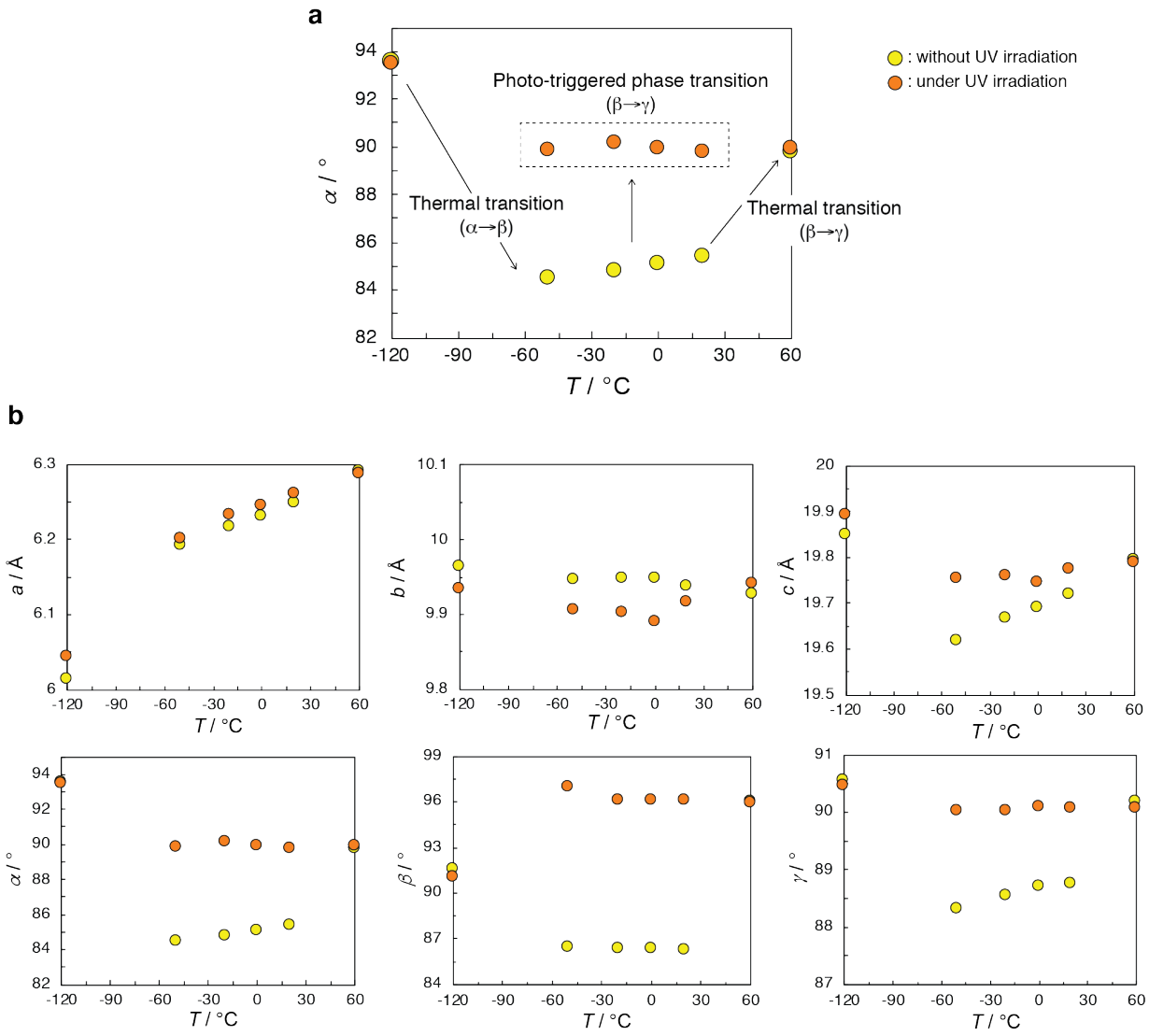

Figure 4.9 Lattice change upon UV light irradiation at variant temperatures. **a,** Photo-triggered phase transition based on α angle change. **b,** Unit cell parameters of *a*-, *b*-, *c*-axes, and α, β, γ angles. The yellow and orange circles indicate the results without and under UV irradiation, respectively.

Interestingly, when a thick enol-(*S*)-**2** crystal (2010 × 1235 × 737 μm^3) was irradiated by UV light (365 nm, 80 mW cm^{-2}) at room temperature (β phase), we could clearly see the phase transition β ↔ γ under a microscope as follows. The crystal started to transform from the irradiated (001) surface upon UV irradiation and then the habit plane propagated to the opposite direction (Figure 4.10a). The angle between (001) and (012) faces at the upper right edge changed from 47° to 45° (Figure 4.10a, c). The transformation continuously propagated to lower direction within 1 s, and the angle between $(0\bar{1}\bar{1})$ and $(00\bar{1})$ at the lower left edge changed from 67° to 63° (Figure 4.10a, c). The deformed shape after UV irradiation corresponds with the crystal shape at γ phase (Figure 4.10c). The propagation speed of the habit plane was calculated to be 920 μm s^{-1} at 80 mW cm^{-2} UV light intensity. The propagation speed became slower with the decrease of light intensity, and the deformation did not complete at a weak light intensity, 20 mW cm^{-2} (Figure 4.11). These results show that there is the threshold of UV light intensity to complete the photo-triggered phase transition.

After stopping UV irradiation, the crystal maintained the deformed shape for 50 s. At the next moment, the habit plane appeared with the return of the angle at the lower left edge from 63° to 67° (50 s, Figure 4.10b). The habit plane gradually progressed to the upper direction (70 s, Figure 4.10b), and then the whole crystal returned to the initial shape at β phase (110 s, Figure 4.10b) The propagation speed of the reverse deformation is roughly consistent with the speed of thermal back- isomerization from *trans*-keto to enol form.

In order to clarify the photothermal effect by UV light, the surface temperature on an enol-(*S*)-**2** crystal was monitored with an infrared (IR) thermography camera (Figure 4.10d–g). When the crystal was irradiated with UV light (365 nm, 80mW cm^{-2}) for 5 s, the temperature on the irradiated surface increased from 23 °C to around 45 °C (Figure 4.10d). Time course of the

temperature change indicates that it took approximately 2.5 s to reach the phase transition temperature of 40 °C (Figure 4.10e). In contrast, the photo-triggered transformation started within 0.2 s, and completed in 1 s (Figure 4.10a). At the time scale, surface temperature increased to around 32 °C, meaning that the photo-triggered transformation completed before reaching the thermal phase transition temperature.

After stopping UV irradiation, the surface temperature decreased to the initial temperature in 10 s (Figure 4.10e). The time scale of temperature decrease is much faster than the crystal shape recovery (Figure 4.10b). These results suggest that the photo-triggered phase transition $\beta \rightarrow \gamma$ is triggered by enol-keto photoisomerization and the reverse transition $\gamma \rightarrow \beta$ occurs due to back-isomerization. When the surface temperature was measured at 2 °C controlled with a Peltier thermostat, the crystal surface temperature rose up to 22 °C upon UV irradiation (Figure 4.10f, g), verifying that the surface temperature measured at low temperature did not rise to 40 °C.

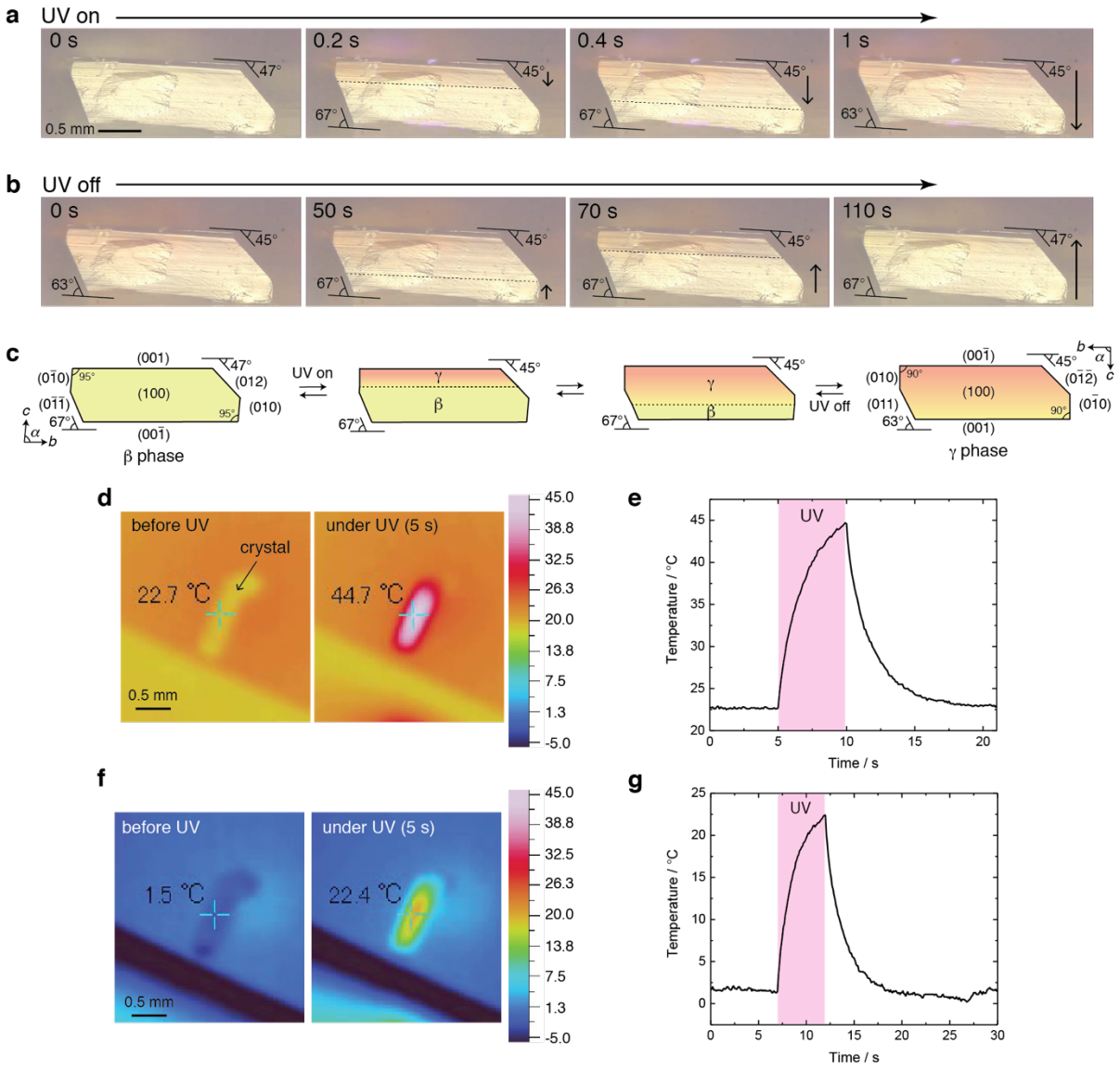

Figure 4.10 Photo-triggered transformation and surface temperature measurement. **a, b,** Photo-triggered transformation of a thick plate-like crystal of enol-(*S*)-**2** (**a**) upon UV light irradiation and (**b**) after stopping the irradiation. Dotted lines indicate the propagation of the habit plane. **c,** Schematic illustration of the photo-triggered transformation. **d, f,** Crystal surface temperature change upon UV light irradiation for 5 s monitored by IR thermography camera. **e, g,** Time dependence of the temperature change.

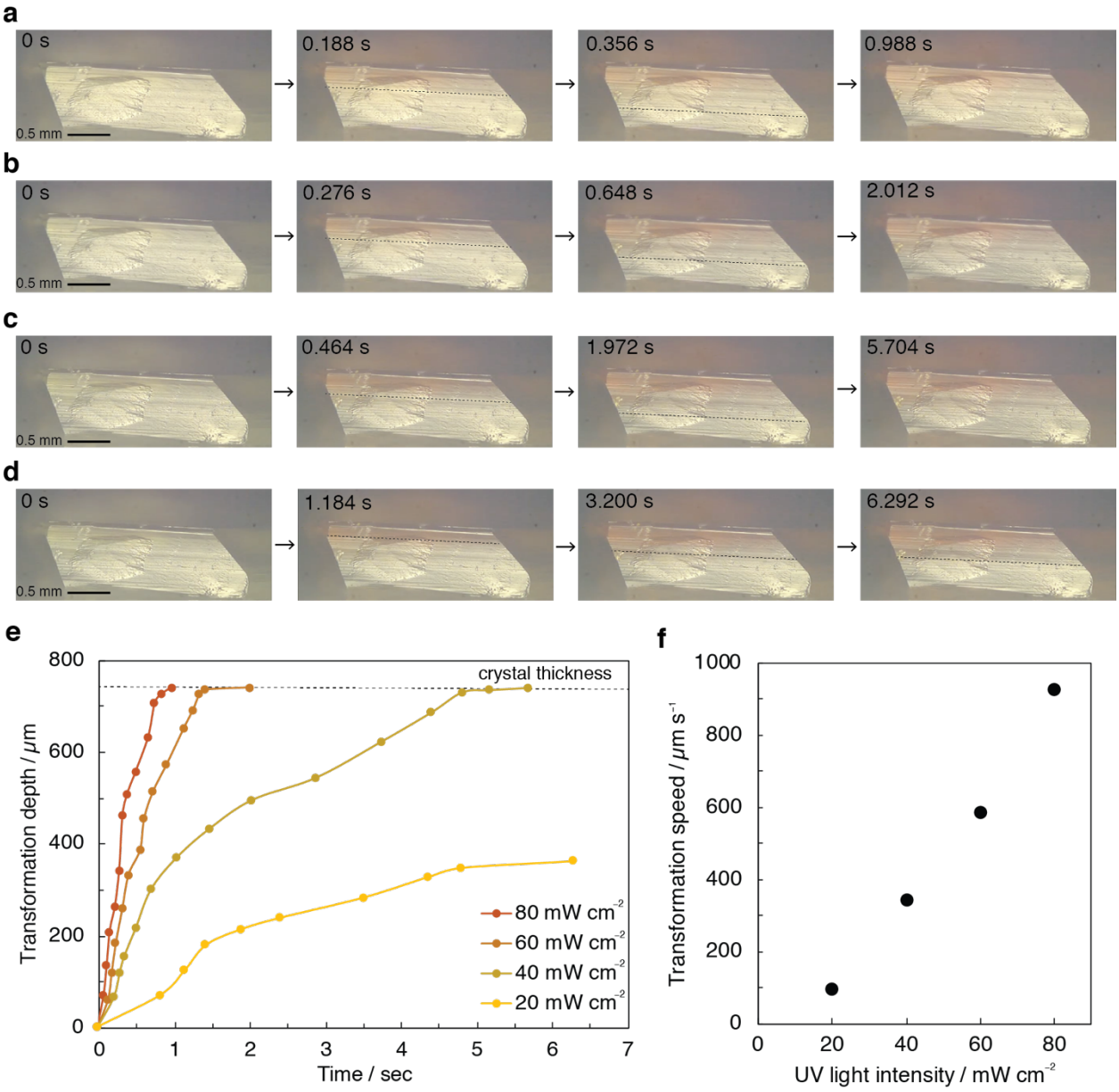

Figure 4.11 UV light strength dependence of photo-triggered transformation. The enol-(*S*)-**2** crystal was irradiated by UV light at the intensities of (**a**) 80, (**b**) 60, (**c**) 40, and (**d**) 20 mW cm^{-2}. Dotted lines indicate the habit plane. **e,** Temporal profile of the transformation depth along the thickness. **f,** Transformation speed calculated from slope until reaching plateau state.

4.3.4 Crystal structure change upon UV irradiation

For elucidation of the structure change due to the photo-triggered phase transition, the crystal structures of an enol-(*S*)-**2** crystal were determined before and under UV irradiation at −50 and 50 °C (Figure 4.12 and Table 4.2). The crystal structures at β and γ phases without UV irradiation were described in detail in a previous section. Under UV light irradiation at −50 °C, the crystal structure at β phase changes to that at γ phase, and *trans*-keto molecule is not found, probably due to insufficient quantities for structure determination. However, the enol-(*S*)-**2** molecule at γ phase achieved by photo-triggered phase transition has slightly different conformation from that at γ phase achieved by simple heating. The molecule under UV irradiation at −50 °C forms the dihedral angle of 47.4°, and the occupancy of the disordered *tert*-butyl group is A: B = 90: 10 (Figure 4.12b). In contrast, the molecule without UV light at 50 °C forms the dihedral angle of 46.6°, and the occupancy of the disordered *tert*-butyl group is A: B = 71: 29 (Figure 4.12c). The conformational difference reflects on the temperature difference because the dihedral angle decreases to 46.6° and the occupancy of the disorder approaches to A: B = 71: 29 depending on temperature rise. The molecular conformation under UV light at 50 °C did not change from that before UV irradiation (Figure 4.12c, d). Thus, the γ phase achieved by the photo-triggered phase transition is a unique state with respect to molecular conformation, which cannot be achieved by thermal phase transition. To our best knowledge, this kind of photo-triggered phase transition is the first finding.

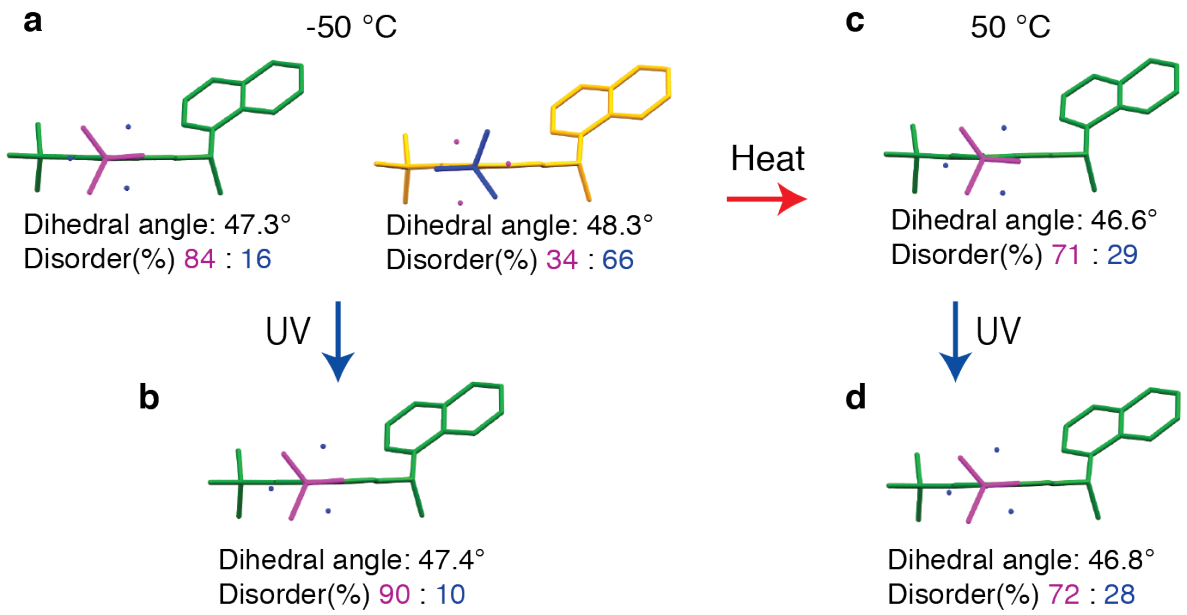

Figure 4.12 Crystal structure change before and under UV light irradiation at −50 and 50 °C. Two independent molecules at β phase are shown in green (molecule 1) and yellow (molecule 2), and an independent molecule at γ phase is drawn in green due to the similarity to molecule 1 at β phase. Hydrogen atoms and tert-butyl bonds with minor occupancy are omitted for clarity.

Table 4.2 Crystallographic parameters without and under UV light irradiation.

Temp. / °C	−50 (β)	−50 (γ)	50 (γ)	50 (γ)
UV	OFF	ON	OFF	ON
Crystal system	Triclinic	Monoclinic	Monoclinic	Monoclinic
Space group	$P1$	$P2_1$	$P2_1$	$P2_1$
a / Å	6.1748(7)	6.1899(3)	6.2700(7)	6.280(2)
b / Å	9.9126(6)	9.8715(5)	9.9262(8)	9.898(3)
c / Å	19.6020(17)	19.7418(14)	19.747(2)	19.713(8)
α / °	84.484(6)	90	90	90
β / °	86.208(8)	96.946(6)	96.206(12)	96.12(3)
γ / °	88.252(7)	90	90	90
V / Å^3	1191.28(19)	1197.44(12)	1221.8(2)	1218.4(7)
Z	2	2	2	2
ρ_{calc} / g·cm^{-3}	1.080	1.075	1.053	1.056
R_1 [$I > 2\sigma(I)$]	0.0889	0.0731	0.0751	0.1291
wR_2 [$I > 2\sigma(I)$]	0.2306	0.1917	0.1847	0.3030
GOF	0.976	0.966	0.913	1.070

Subsequently, the time dependence of unit cell changes after stopping UV light was measured at −50 °C (Figure 4.13 and 4.14). For instance, the α angle, which becomes 90° due to the photo-triggered phase transition β → γ, maintained 90° at least 80 min after stopping the irradiation (Figure 4.13). In contrast, when the crystal was irradiated by visible light (488 nm, 10 mW cm^{-2}) just after stopping UV light, the α angle returned to 85° at β phase in 20 min (Figure 4.14). Faster returning of the unit cell under visible light corresponds to back-photoisomerization much faster than thermal back-isomerization (Figure 4.8). These lattice change behaviors with and without visible light verify that the phase transition γ → β is triggered by back-isomerization from *trans*-keto to enol form.

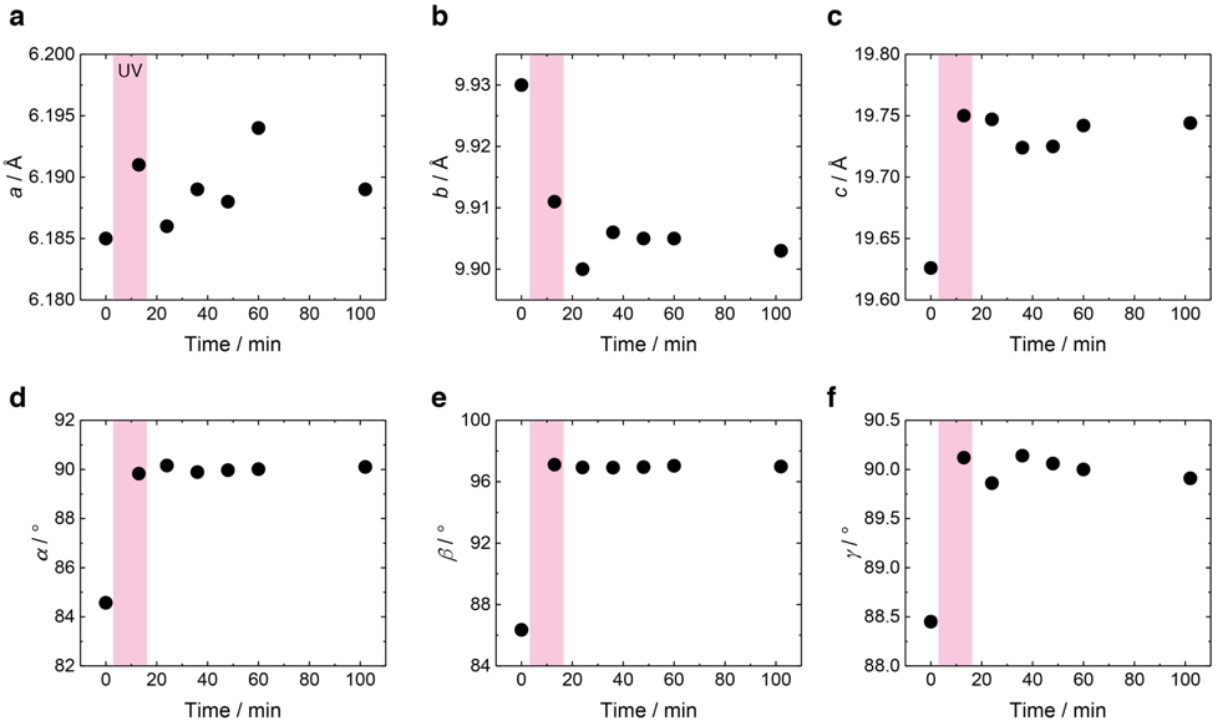

Figure 4.13 Unit cell changes after stopping UV light irradiation at −50 °C. Unit cell parameters of (a–c) *a*-, *b*-, *c*-axes, and (d–f) α, β, γ angles. The sample (0.4 × 0.4 × 0.08 mm^3) was irradiated by UV light (365 nm, 60 mW cm^{-2}) during the second measurement.

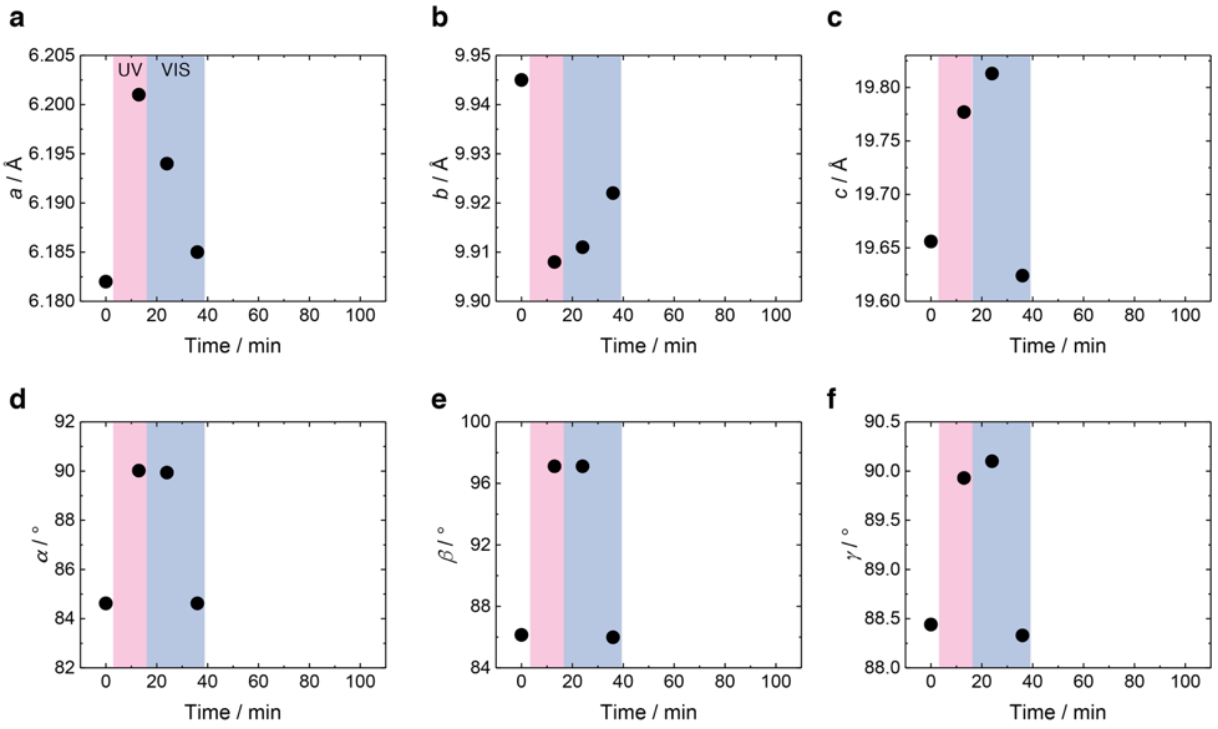

Figure 4.14 Unit cell changes upon visible light irradiation just after stopping UV light at −50 °C. Unit cell parameters of (a–c) *a*-, *b*-, *c*-axes, and (d–f) α, β, γ angles. The sample (0.4 × 0.4 × 0.08 mm^3) was irradiated by UV light (365 nm, 60 mW cm^{-2}) during the second measurement, and then by visible light (488 nm, 10 mW cm^{-2}) during subsequent measurements.

4.3.5 Stepwise bending

From the perspective of actuation behavior, the photo-triggered phase transition should lead to stepwise bending (Figure 4.15). When the (001) face of a thin plate-like enol-(*S*)-**2** crystal (4072 × 940 × 36 μm^3) at β phase was irradiated from the left with UV light (365 nm, 60 mW cm^{-2}) at room temperature, the crystal bent towards the light source with twisting motion in 0.2 s, accompanied by color change from yellow into orange (Figure 4.15a, b). In the next moment, the bent crystal suddenly released the twisting motion (Figure 4.15c). Then, the crystal continued to

bend towards the light source without twisting under prolonged UV irradiation (Figure 4.15d). After stopping light irradiation, the bending gradually returned without a twist in 45 s (Figure 4.15e). The bent crystal started to twist slowly, and then became the most twisted shape in 70 s (Figure 4.15f). The bending with a twist gradually relaxed, and then the crystal became the initial straight shape with color returning to yellow (Figure 4.15g).

The bending behavior in photo process is divided into three steps: (1) bending with twisting due to enol-keto photoisomerization at β phase, (2) the disappearance of the twist due to the photo-triggered phase transition β → γ, and (3) bending without twist due to enol-keto photoisomerization at γ phase. The motion at each step was confirmed by applying weak UV light and IR light heating separately (Figure 4.16). Thermal relaxation behavior of the bending can be explained by the reverse process. Bending relaxation without twist occurs due to thermal back-isomerization at γ phase. Then, twisting motion gradually appears due to the progress of the phase transition γ → β triggered by thermal back-isomerization. The bending with a twist returns to the initial unbent shape due to thermal back-isomerization at β phase.

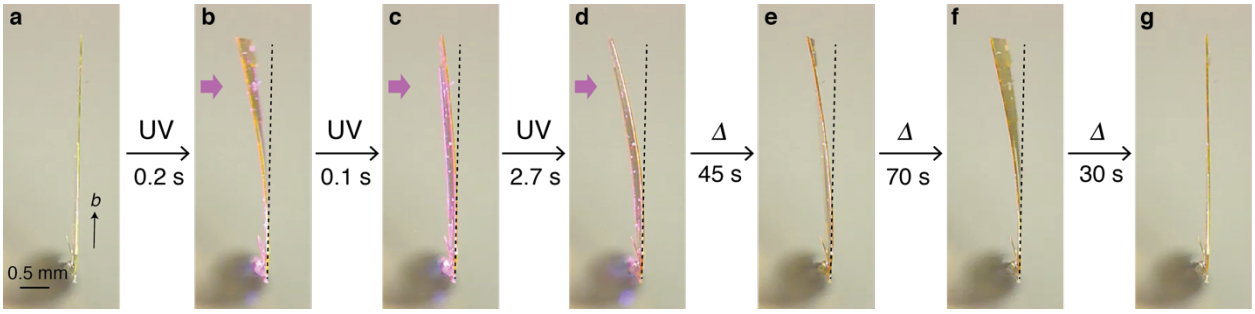

Figure 4.15 Stepwise bending of a thin plate-like crystal of enol-(*S*)-**2** upon photoirradiation. **a–g,** Snapshots of the stepwise bending from the side view of the plate-like crystal. **a, b,** Fast bending with twisting at β phase upon UV light irradiation. **c,** Sudden disappearance of the twist due to the

photo-triggered phase transition β → γ. **d,** Bending without twist at γ phase under UV light. **e,** Thermal relaxation of the bending without twist at γ phase. **f,** Gradual appearance of twist due to the reverse phase transition γ → β. **g,** Returning to the initial shape at β phase.

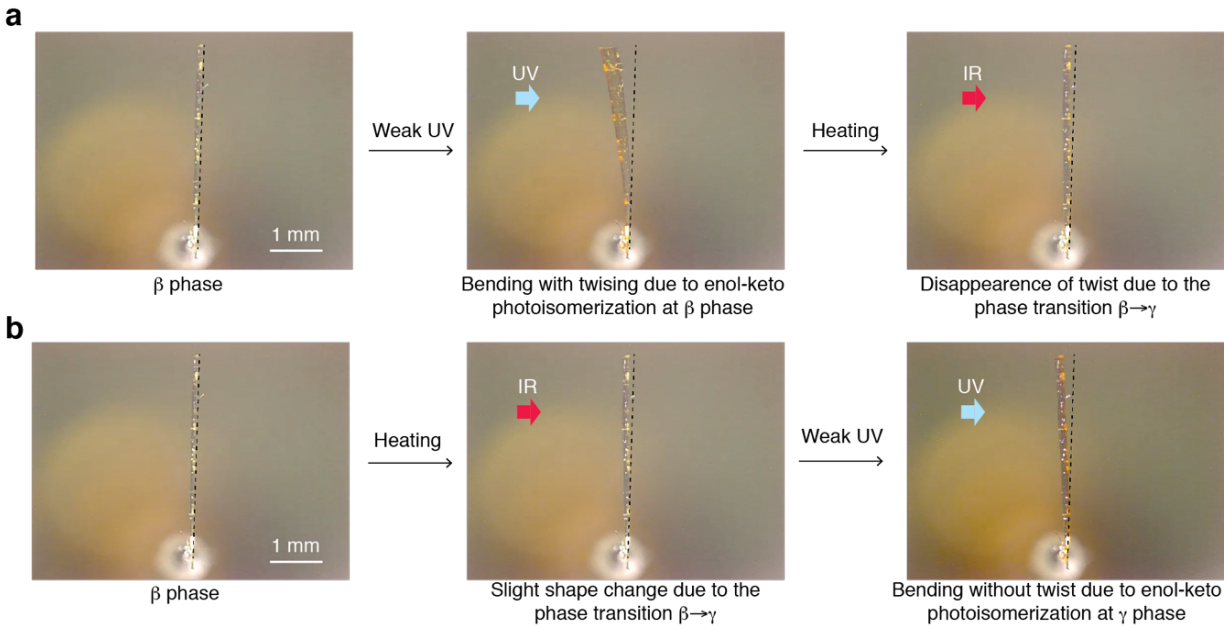

Figure 4.16 Bending behaviors separately induced by light and heat. **a,** Bending behavior of a thin enol-(*S*)-**2** crystal (4072 × 940 × 36 μm^3) induced firstly by weak UV light (365 nm, 5 mW cm^{-2}), and secondly by heating with IR light. **b,** Bending behavior of the crystal induced firstly by heating with IR light, and secondly by weak UV light. Upon weak UV irradiation, the crystal bent with twisting due to enol-keto photoisomerization at β phase. The twisted shape disappeared due to the phase transition β → γ upon subsequent heating with IR light. When the crystal was firstly heated with IR light, the crystal shape slightly changed due to the phase transition β → γ, and then the crystal bent slightly without twist due to enol-keto photoisomerization at γ phase upon weak UV irradiation.

4.3.6 Possible mechanism of photo-triggered phase transition

In order to consider the structural change due to photoisomerization, the structures of enol, *trans*-keto, and *cis*-keto forms were optimized by density functional theory calculation at the theory level of B3LYP/6-31G (Figure 4.17a).[24] The optimized structure of enol-(*S*)-**2** with dihedral angle 56° is almost consistent with the X-ray crystallographic result of enol-(*S*)-**2** crystal, and *cis*-keto-(*S*)-**2** is similar to enol-(*S*)-**2**. In contrast, the structure of *trans*-keto-(*S*)-**2** is relatively different from enol-(*S*)-**2**, forming dihedral angle 85°. This structural difference between enol and *trans*-keto forms suggests that photoisomerization from enol to *trans*-keto form undergoes by pedal motion in a limited space[25] and generates strain in the crystal (Figure 4.17b).

The photoisomerization should lead to the photo-triggered phase transition (Figure 4.17c–e). The enol-(*S*)-**2** crystal before photoirradiation is β phase (Figure 4.17c). Upon UV irradiation, *trans*-keto molecules are produced due to photoisomerization at the irradiated surface, generating strain in the crystal (Figure 4.17d). The strain due to *trans*-keto molecules will induce conformational changes of surrounding molecules. Then, the conformation change will further influence on the next surrounding molecules like a domino, triggering crystal structure change from β to γ phase (Figure 4.17e). When *trans*-keto molecules are produced at a certain low ratio, the whole crystal complete the phase transition into γ phase. When the light irradiation is stopped, thermal back-isomerization from *trans*-keto to enol form undergoes in the crystal, triggering the reverse phase transition γ → β (Figure 4.17d).

This transition mechanism indicates that γ phase reached by photo-triggered phase transition requires *trans*-keto molecules to maintain the crystal phase. In fact, phase transition γ → β under visible light irradiation processed faster than that without visible light because the half-

life of back-photoisomerization from *trans*-keto to enol form is much shorter than that of thermal back-isomerization.

The manifestation of the photo-triggered phase transition should be correlated with the enthalpy, which is the energy barrier required for the phase transition. The enthalpy at the phase transition $\beta \rightarrow \gamma$ (0.2 kJ mol^{-1}) is one fifth smaller than that at the phase transition $\alpha \rightarrow \beta$ (1 kJ mol^{-1}). The difference of these transition enthalpies supports that enol–keto photoisomerization triggers the phase transition $\beta \rightarrow \gamma$, but does not trigger the phase transition $\alpha \rightarrow \beta$ due to larger enthalpy. The enthalpy at the phase transition $\beta \rightarrow \gamma$ is also smaller than other structural phase transition of molecular crystals.[2, 3, 26–30]

Additionally, the enthalpy at the transition $\beta \rightarrow \gamma$ is 10–200 times larger than energy densities of superelastic and ferroelastic molecular crystals, which can deform with the creation of new crystalline phase or twin domain by manually applying shear stress.[31–34] This suggests that it will be difficult to create γ phase by shear stress in enol-(*S*)-**2** crystal at β phase. In fact, we did not see any crystal deformation of an enol-(*S*)-**2** crystal when manually applied stress under a microscope.

Finally, we would like to discuss the difference between the photo-triggered phase transition in this paper and the photo-induced phase transition in the literatures.[10–13] The crystal phase due to photo-induced phase transition appears only by light irradiation, which changes electric or magnetic properties in femto- or pico-seconds. In the case of photo-triggered phase transition, the crystal phase triggered by light is identical to that triggered by heating, but unique with respect to molecular conformation. Thus, the photo-triggered phase transition may lead a new strategy to broaden the ability of photo-responsive solids as a new mechanism.

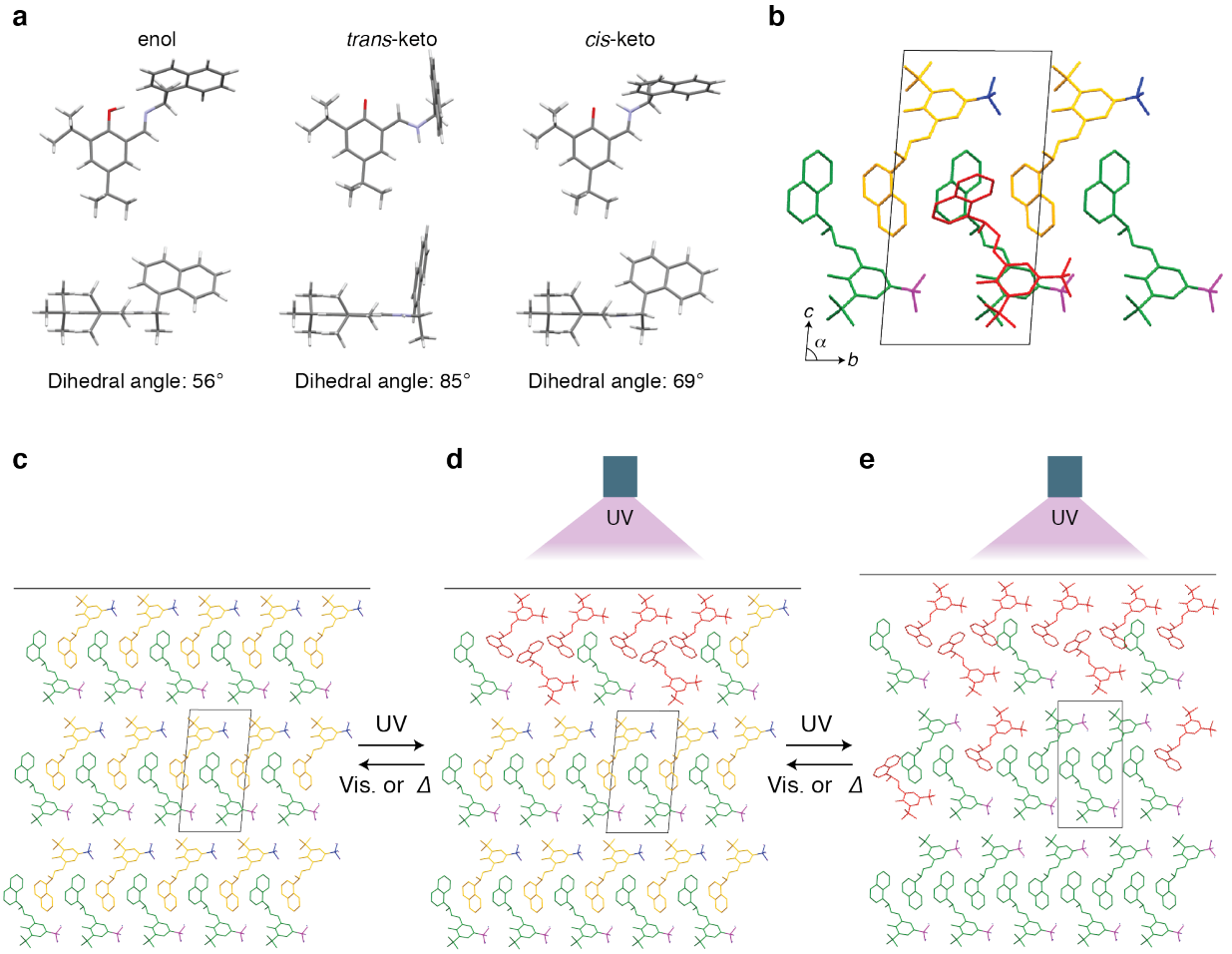

Figure 4.17 Possible mechanism of photo-triggered phase transition. **a,** Molecular structure of enol, *trans*-keto, and *cis*-keto molecules viewed perpendicular and parallel to the salicylidene plane obtained by density functional theory calculation. **b,** Overlay of a *trans*-keto molecule on (001) face of enol-(*S*)-**2** crystal at β phase. Two independent molecules at β phase drawn in yellow and green, and *trans*-keto molecule is drawn in red. **c,** (001) plane view at β phase before UV irradiation. **d,** Photoisomerization in the crystal at β phase. **e,** Photo-triggered phase transition β → γ due to the strain of *trans*-keto molecules.

4.4 Conclusion

The photo-triggered phase transition of an enol-(*S*)-**2** crystal was discovered as a new structural phase transition mechanism. X-ray crystallographic analysis under light irradiation elucidated that the photo-triggered phase transition changed crystal structure with a unique molecular conformation, which cannot be achieved by thermal structural phase transition. The photo-triggered phase transition originated from strain due to *trans*-keto molecules produced by enol–keto photoisomerization and a small energy barrier of the structure change. For a function accompanied by the structural phase transition, photo-triggered phase transition enabled thin crystals to bend in stepwise by light irradiation. This phase transition mechanism has the potential to broaden the functions of photo-responsive solid materials.

4.5 References

1. Taniguchi, T., Fujisawa, J., Shiro M., Koshima, H., Asahi, T. Mechanical motion of chiral azobenzene crystals with twisting upon photoirradiation. *Chem. Eur. J.* **22**, 7950–7958 (2016).
2. Taniguchi, T., Sugiyama, H., Uekusa, H., Shiro, M., Asahi, T., Koshima, H. Walking and rolling of crystals induced thermally by phase transition. *Nat. Commun.* **9**, 538 (2018).
3. Kitagawa, D., Kawasaki, K., Tanaka, R., Kobatake, S. Mechanical behavior of molecular crystals induced by combination of photochromic reaction and reversible single-crystal-to-single-crystal phase transition. *Chem. Mater*. **29**, 7524–7532 (2017).
4. Cohen, R. E. Origin of ferroelectricity in perovskite oxides. *Nature* **358**, 136–138 (1992).
5. Smith, M. B., Page, K., Siegrist, T., Redmond, P. L., Walter, E. C., Seshadri, R., Brus, L. E., Steigerwald, M. L. Crystal structure and the paraelectric-to-ferroelectric phase transition of nanoscale $BaTiO_3$. *J. Am. Chem. Soc.* **130**, 6955–6963 (2008).
6. Wu, Z., Cohen, R. E. Pressure-induced anomalous phase transitions and colossal enhancement of piezoelectricity in $PbTiO_3$. *Phys. Rev. Lett.* **95**, 037601 (2005).
7. Maat, S., Thiele, J. U., Fullerton, E. E. Temperature and field hysteresis of the antiferromagnetic-to-ferromagnetic phase transition in epitaxial FeRh films. *Phys. Rev. B* **72**, 214432 (2005).
8. Pons, J., Chernenko, V. A., Santamarta, R., Cesari, E. Crystal structure of martensitic phases in Ni–Mn–Ga shape memory alloys. *Acta Mater.* **48**, 3027–3038 (2000).
9. Otsuka, K., Ren, X. Physical metallurgy of Ti–Ni-based shape memory alloys. *Prog. Mater. Sci.* **50**, 511–678 (2005).
10. Koshihara, S., Tokura, Y., Takeda, K., Koda, T. Reversible photoinduced phase transitions in single crystals of polydiacetylenes. *Phys. Rev. Lett*. **68**, 1148–1151 (1992).

11. Fukazawa, N., Shimizu, M., Ishikawa, T., Okimoto, Y., Koshihara, S., Hiramatsu, T., Nakano, Y., Yamochi, H., Saito, G., Onda, K. Charge and structural dynamics in photoinduced phase transition of $(EDO\text{-}TTF)_2PF_6$ examined by picosecond time-resolved vibrational spectroscopy. *J. Phys. Chem. C* **116**, 5892–5899 (2012).

12. Gao, M., Lu, C., Jean-Ruel, H., Liu, L. C., Marx, A., Onda, K., Koshihara, S., Nakano, Y., Shao, X., Hiramatsu, T., Saito, G., Yamochi, H., Cooney, R. R., Moriena, G., Sciaini, G., Miller, D. R. J. Mapping molecular motions leading to charge delocalization with ultrabright electrons. *Nature* **496**, 343–346 (2013).

13. Morrison, V. R., Chatelain, R. P., Tiwari, K. L., Hendaoui, A., Bruhács, A., Chaker, M., Siwick, B. J. A photoinduced metal-like phase of monoclinic VO_2 revealed by ultrafast electron diffraction. *Science* **346**, 445–448 (2014).

14. Kuwahara, H., Tomioka, Y., Asamitsu, A., Moritomo, Y., Tokura, Y. A first-order phase transition induced by a magnetic field. *Science* **270**, 961–963 (1995).

15. Jeong, J., Aetukuri, N., Graf, T., Schladt, T. D., Samant, M. G., Parkin, S. S. Suppression of metal-insulator transition in VO_2 by electric field–induced oxygen vacancy formation. *Science* **339**, 1402–1405 (2013).

16. Maji, T. K., Mostafa, G., Matsuda, R., Kitagawa, S. Guest-induced asymmetry in a metal-organic porous solid with reversible single-crystal-to-single-crystal structural transformation. *J. Am. Chem. Soc*. **127**, 17152–17153 (2005).

17. Scott, J. F. Applications of modern ferroelectrics. *Science* **315**, 954–959 (2007).

18. Song, G., Ma, N., Li, H. N. Applications of shape memory alloys in civil structures. *Eng. Struct.* **28**, 1266–1274 (2006).

19. Smith, H. E., Cook, S. L., Warren, M. E., Jr. Optically active amines. II. The optical rotatory dispersion curves of the N-benzylidene and substituted N-benzylidene derivatives of some open-chain primary amines. *J. Org. Chem*. **29**, 2265–2272 (1964).
20. Takanabe, A., Tanaka, M., Johmoto, K., Uekusa, H., Mori, T., Koshima, H., Asahi, T. Optical activity and optical anisotropy in photomechanical crystals of chiral salicylidenephenylethylamines. *J. Am. Chem. Soc.* **138**, 15066–15077 (2016).
21. Sheldrick, G. M. A short history of SHELX. *Acta Crystallogr.* A **64**, 112–122 (2008).
22. CrystalStructure v.4. 2. 2. (Rigaku Corporation, Tokyo, Japan, 2016).
23. Hübschle, C. B., Sheldrick, G. M. & Dittrich, B. ShelXle: a Qt graphical user interface for SHELXL. *J. Appl. Cryst.* **44**, 1281–1284 (2011).
24. Frisch, M. J. *et al*. *Gaussian* 09, *Rev.* B.01, Gaussian, Inc., Wallingford, USA, CT (2010).
25. Harada, J., Uekusa, H., Ohashi, Y. X-ray analysis of structural changes in photochromic salicylideneaniline crystals. Solid-state reaction induced by two-photon excitation. *J. Am. Chem. Soc.* **121**, 5809–5810 (1999).
26. Yao, Z. S., Mito, M., Kamachi, T., Shiota, Y., Yoshizawa, K., Azuma, N., Miyazaki, Y., Takahashi, K., Zhang, K., Nakanishi, T., Kang, S., Kanegawa, S., Sato, O. Molecular motor-driven abrupt anisotropic shape change in a single crystal of a Ni complex. *Nat. Chem*. **6**, 1079–1083 (2014).
27. Shima, T., Muraoka, T., Hoshino, N., Akutagawa, T., Kobayashi, Y., Kinbara, K. Thermally driven polymorphic transition prompting a naked-eye-detectable bending and straightening motion of single crystals. *Angew. Chem. Int. Ed.* **53**, 7173–7178 (2014).
28. Takanabe, A., Katsufuji, T., Johmoto, K., Uekusa, H., Shiro, M., Koshima, H., Asahi, T. Reversible single-crystal-to-single-crystal phase transition of chiral

salicylidenephenylethylamine. *Crystals* **7**, 7 (2016).

29. Nath, N. K., Severa, L., Kunetskiy, R. A., Císařová, I., Fulem, M., Růžička, K., Koval, D., Kašička, V. Teplý, F. Naumov, P. Single-crystal-to-single-crystal transition in an enantiopure [7] helquat salt: the first observation of a reversible phase transition in a helicene-like compound. *Chem. Eur. J.* **21**, 13508–13512 (2015).
30. Dharmarwardana, M., Welch, R. P., Kwon, S., Nguyen, V. K., McCandless, G. T., Omary, M. A., Gassensmith, J. J. Thermo-mechanically responsive crystalline organic cantilever. *Chem. Commun*. **53**, 9890–9893 (2017).
31. Takamizawa, S., Miyamoto, Y. Superelastic organic crystals. *Angew. Chem. Int. Ed.* **53**, 6970–6973 (2014).
32. Takamizawa, S., Takasaki, Y. Superelastic shape recovery of mechanically twinned 3,5-difluorobenzoic acid crystals. *Angew. Chem. Int. Ed.* **54**, 4815–4817 (2015).
33. Mir, S. H., Takasaki, Y., Engel, E. R., Takamizawa, S. Ferroelasticity in an organic crystal: a macroscopic and molecular level study. *Angew. Chem. Int. Ed*. **56**, 15882–15885 (2017).
34. Engel, E. R., Takamizawa, S. Versatile Ferroelastic deformability in an organic single crystal by twinning about a molecular zone axis. *Angew. Chem. Int. Ed*. **57**, 11888–11892 (2018).

Chapter 5

Summary and Future prospects

5.1 Summary

Previous three chapters have described the diversification of actuation besides monotonous bending (Table 5.1). In chapter 2, chiral azobenzene *trans*-(*S*)-**1** crystals bent with a slight twist upon UV irradiation. The twisting motion was estimated to be induced by the elongation along the diagonal direction at the irradiated surface due to *trans–cis* photoisomerization. In chapter 3, the *trans*-(*S*)-**1** crystals walked or rolled due to a structural phase transition at 145 °C upon heating and cooling. The thermal locomotion originated from unsymmetrical crystal shape. Chapter 4 mentioned the discovery of a photo-triggered phase transition and stepwise bending of enol-(*S*)-**2** crystals. The photo-triggered phase transition originated from the strain of *trans*-keto molecules produced by enol–keto photoisomerization owing to the small transition enthalpy. This photo-triggered phase transition enabled thin enol-(*S*)-**2** crystals to bend in stepwise.

Table 5.1 Summary of mechanical crystals in this thesis.

Material	Stimulus	Mechanism	Actuation Mode
Trans-(*S*)-**1**	Light (Chapter 2)	*Trans–cis* photoisomerization	Bending with twist
	Temperature (Chapter 3)	Structural phase transition	Bending Locomotion
Enol-(*S*)-**2**	Light (Chapter 4)	Enol–keto photoisomerization & Photo-triggered phase transition	Stepwise bending with twist
	Temperature (Chapter 4)	Structural phase transition	Transformation

Based on these findings, here is describing several strategies to vary actuation mode of molecular crystals. At first, chirality in a crystal should be an easy way to induce twisting motion. The twist motion probably originates from that irradiated surface of a chiral crystal elongates or contracts along the diagonal direction. A chiral environment in the crystal should play a role in twisting motion although it has been difficult to reveal the actual correlation between twist direction and chirality handedness.

The second strategy is to engineer crystal shape. Crystals are grown naturally as they like, but when unsymmetrical crystals are obtained, the motion such as bending should lead to locomotion. If the crystal shape is controlled more precisely and diversely, it will be possible not only to tune speed and direction of locomotion, but also to exhibit more complicated motion.

The third one is to utilize a structural phase transition. Since a structural phase transition is a change of molecular alignment, it can be combined with a molecular-level change such as photochromic reaction, triggering stepwise actuation. In addition, the amount of transition enthalpy required for the structure change should be paid attention because it indicates an energy barrier at the structural phase transition. When the transition enthalpy is quite low (0.2 kJ mol^{-1} in the case of chapter 4), the photo-triggered phase transition in other crystals will be discovered.

Thus, this thesis has described molecular crystals' actuation besides bending, and proposed promising strategies to diversify mechanical motion.

5.2 Future prospects

The recent development of soft robots, biomedical medical devices, 3D and 4D printers requires actuation organic materials owing to their inherent features of lightweight and softness. Active polymers and gels are being applied to those devices, and the number of examples is increasing exponentially due to the demand from the highly informative and super-aging society. As such situation, the time has come for mechanical crystals to stand on the application-aimed stage.

For the purpose, there are currently two major difficulties in mechanical crystals. One is to increase the maximum force at actuation, and the other is to fabricate the desired shape. As to the maximum force, mechanically responsive molecular crystals typically generate maximum stress in the range of 1–50 MPa at actuation. These values are generally 10–100 times larger than maximum stress of typical human muscle (0.3 MPa). However, the maximum force of molecular crystals is limited to μN–mN order, which is much smaller than muscles and metallic materials. This limitation of molecular crystals should originate from the small deflection and the difficulty to control size/shape. Thus, difficulties to increase force and fabricate desired shape are sometimes correlated in molecular crystals.

In order to exceed these limitations, hybridization of crystal and polymer is a promising approach. When molecular crystals are incorporated in a connective polymer, the hybrid material will be more flexible and easier to control size/shape than molecular crystals due to the advantage of the polymer. In addition, such hybrid materials should response faster and generate larger force than polymers owing to the advantage of molecular crystals. Thus, this hybrid strategy will increase the maximum force and improve the fabrication process. Finally, it is expected that hybrid actuation materials using mechanical crystals work in some devices in the future.

Acknowledgements

First of all, I would like to express my sincere gratitude to my supervisor Prof. Toru Asahi for his continuous support of my laboratory work. His guidance and motive suggestions have helped me in all the time of research and lab work in spite of his super-busyness since 2012 when I joined to Asahi laboratory. Also, owing to his organization and management of some programs and workshops including Leading Graduate Program at Waseda University, I have been to several foreign countries for presentations and collaborative researches. The experiences at abroad have inspired me to make connections all over the world. These experiences, connections, and knowledge will be absolutely effective to my academic carrier.

Besides him, I would like to thank Prof. Hideko Koshima for the continuous support of my doctoral research. Her guidance and suggestions have led me to improve research skills to analyze data, to make scientific presentations, to write academic papers, to pass competitive research grant, and so on. Owing to her informative and strict advice, I have advanced one step an academic field through my doctoral research.

I also thank my other thesis committee: Prof. Yukio Furukawa, Prof. Atsushi Shimojima, and Dr. Hiromi Takahashi. Their multilateral comments from fundamental science and application perspective have refined my doctoral thesis. In addition, I thank Prof. Furukawa for his acceptance of my lab rotation in 2014. Also, I thank Dr. Takahashi for his support to use the optical waveguide spectrometer and his kindness at scientific conferences.

My sincere thank also goes to Prof. Hidehiro Uekusa and Dr. Motoo Shiro for their supports of X-ray diffraction analysis. Owing to their informative advice and discussions with them, I have acquired the skills to obtain reliable diffraction data and analyze complicated crystal structures such as disorders.

I also thank Assoc. Prof. Panče Naumov and Dr. Ejaz Ahmed at New York University Abu Dhabi (NYUAD) where I spent two months in 2017. They helped me to experience my first long stay at abroad. Through the stay at NYUAD and the research on photosalient crystals, I have made the connection with them and understood photoreactive crystals more deeply.

I also thank Prof. Shuji Hashimoto for his advice from the perspective of robotics and engineering. I spend a short time in Hashimoto laboratory as lab rotation in 2016 owing to his kind acceptance. During the lab rotation, I have learned the importance of actuation materials, and understood specifications of them to apply robots.

I also thank Assoc. Prof. Pierre Lambert and Mr. Loïc Blanc at Université Libre de Bruxelles (ULB) where I spent two months in 2018. Through the collaborative research on active materials, I have understood how to fabricate materials with desired shapes and optimize parameters. Their perspective from robotics has strongly helped me to rethink more deeply about how actuation materials should be constructed. Owing to their advice and frequent discussions with them, I have successfully progressed the research on hybrid materials.

I also thank Mr. Ryosuke Shibato and Ms. Hitomi Suto at academist, Inc. where I experienced an internship. The internship has led me to improve logical writing skill and broaden my value of research and academic.

I also thank other faculties and lab members at Asahi lab. Their advice and discussions in weekly seminars and daily life have promoted and helped me to progress doctoral research.

Last but not the least, I am really grateful to my father Hirokazu and mother Minako. They have supported me to survive in all ways since the birth of me. In particular, they supported financially my university life. I also thank my brother, sister, dog, relatives, and ancestors for the existence of me.

Academic Achievements

Publications

○ 1. Takuya Taniguchi, Hiroyasu Sato, Yuki Hagiwara, Toru Asahi, Hideko Koshima, "Photo-triggered phase transition of a crystal", *Communications Chemistry*, accepted.

2. Takuya Taniguchi, Ayumi Kubota, Tatsuya Moritoki, Toru Asahi, Hideko Koshima, "Two-step photomechanical motion of a dibenzobarrelene crystal", *RSC Advances*, **8**, 34314–34320 (2018).

○ 3. Takuya Taniguchi, Haruki Sugiyama, Hidehiro Uekusa, Motoo Shiro, Toru Asahi, Hideko Koshima, "Walking and rolling of crystals induced thermally by phase transition", *Nature Communications*, **9**, article number: 538 (2018).

○ 4. Takuya Taniguchi, Juri Fujisawa, Motoo Shiro, Hideko Koshima, Toru Asahi, "Mechanical Motion of Chiral Azobenzene Crystals with Twisting upon Photoirradiation", *Chemistry - A European Journal*, **22**, 7950–7958 (2016).

5. Hideko Koshima, Hidetaka Uchimoto, Takuya Taniguchi, Jun Nakamura, Tsuyoshi Asahi, Toru Asahi, "Mechanical Motion of Molecular Crystals induced by [4+4] Photodimerisation", *CrystEngComm*, **18**, 7305–7310 (2016).

Presentations

(International, Oral)

1. Takuya Taniguchi, Hideko Koshima, "Photomechanical and Thermomechanical Molecular Crystals", 31st European Crystallographic Meeting, MS34-O2, 22–27 August 2018, Oviedo, Spain.

2. Takuya Taniguchi, Hideko Koshima, Toru Asahi, "Photomechanical Motion of Crystals of Anthracene Derivative", The 12th Japan-China Joint Symposium on Conduction and Photoconduction in Organic Solids and Related Phenomena, EN5, 16–18 October 2016, Tokyo, Japan.

(International, Poster)

1. Takuya Taniguchi, Haruki Sugiyama, Hidehiro Uekusa, Motoo Shiro, Hideko Koshima, Toru Asahi, "Thermal Locomotion of Chiral Crystals by Phase Transition", 4th Molecular Chirality Asia, P-34, 3–6 July 2018, Harbin, China.
2. Takuya Taniguchi, Haruki Sugiyama, Hidehiro Uekusa, Motoo Shiro, Hideko Koshima, Toru Asahi, "Walking and Running of Chiral Azobenzene Crystals", Toyota Riken International Workshop on Chirality, P32, 24–26 November 2017, Nagoya, Japan.
3. Takuya Taniguchi, Haruki Sugiyama, Hidehiro Uekusa, Motoo Shiro, Hideko Koshima, Toru Asahi, "Directional Locomotion of Chiral Azobenzene Crystals", 29th International Symposium on Chirality (Chirality 2017), P-012, 9–12 July 2017, Tokyo, Japan.
4. Takuya Taniguchi, Haruki Sugiyama, Hidehiro Uekusa, Motoo Shiro, Hideko Koshima, Toru Asahi, "Directional Locomotion of Chiral Azobenzene Crystals by Phase Transition", The 23rd International Conference on the Chemistry of the Organic Solid State (ICCOSS XXIII), P-53, 2–7 April 2017, Stellenbosch, South Africa.
5. Takuya Taniguchi, Motoo Shiro, Hideko Koshima, Toru Asahi, "Photomechanical Bending with Twisting of Chiral Azobenzene Crystals", 26th IUPAC International Symposium on Photochemistry, 2P40, 3–8 April 2016, Osaka, Japan.

6. Takuya Taniguchi, Motoo Shiro, Hideko Koshima, Toru Asahi, "UV-visible spectral analysis of azobenzene crystals with optical waveguide spectrometer", Pacifichem 2015, ANLY 959, 15–20 December 2015, Honolulu, USA.
7. Takuya Taniguchi, Motoo Shiro, Hideko Koshima, Toru Asahi, "Photomechanical bending of chiral and racemic crystals of azobenzene derivatives", Pacifichem 2015, MTLS 978, 15–20 December 2015, Honolulu, USA.
8. Takuya Taniguchi, Juri Fujisawa, Hideko Koshima, Toru Asahi, “Photomechanical Bending of Chiral and Racemic Azobenzene Crystals”, The 22nd International Conference on the Chemistry of the Organic Solid State (ICCOSS XXII), P27, 12–17 July 2015, Niigata, Japan.
9. Takuya Taniguchi, Kazuhiko Ishikawa, Kenta Nakagawa, Masahito Tanaka, Toru Asahi, "Measurement of chiroptical properties of nickel sulfate hexahydrate with G-HAUP", 23rd Congress and General Assembly of the International Union of Crystallography (IUCr 2014), PF.P02.B688, 5–12 August 2014, Montreal, Canada.
10. Takuya Taniguchi, Kazuhiko Ishikawa, Masahito Tanaka, Toru Asahi, "Measurement of Optical Properties of Nickel Sulfate Hexahydrate with Generalized HAUP", 29th International Symposium on Chirality (Chirality 2013), P-016, 7–10 July 2013, Shanghai, China.

(Domestic, Oral)

1. 谷口卓也, 杉本良太, 小宮潤, 佐藤寛泰, 小島秀子, 朝日透, "Thermal and Photo-triggered Phase Transition of Chiral Salicylidenenaphthylethylamine Crystal", 日本化学会第 98 春季年会, 1I3-19, 2018 年 3 月 20–23 日, 千葉.

2. 谷口卓也, 久保田あゆみ, 守時達也, 朝日透, 小島秀子, "ジベンゾバレレン結晶の光屈曲", 日本化学会第 98 春季年会, 2F6-10, 2018 年 3 月 20–23 日, 千葉.
3. 小宮潤, 谷口卓也, 山中大樹, 古部昭広, 杉山晴紀, 植草秀裕, 佐藤寛泰, 小島秀子, 朝日透, "サリチリデンアニリン結晶における光屈曲の高速化", 日本化学会第 98 春季年会, 3I3-33, 2018 年 3 月 20–23 日, 千葉.
4. 小宮潤, 谷口卓也, 山中大樹, 古部昭広, 小島秀子, 朝日透, "光と熱によるアミノサリチリデンアニリン結晶の屈曲挙動", 第 26 回有機結晶シンポジウム, O-22, 2017 年 11 月 3–5 日, 米沢.
5. 谷口卓也, 杉本良太, 小宮潤, 小島秀子, 朝日透, "Photo- and Thermal-induced Mechanical Motion of Chiral Salicylideneaniline Crystals", 2017 年光化学討論会, 1D01, 2017 年 9 月 4–6 日, 仙台.
6. 谷口卓也, 杉山晴紀, 植草秀裕, 城始勇, 小島秀子, 朝日透, "熱によって動き回るキラルアゾベンゼン結晶", 日本化学会第 97 春季年会, 1E7-19, 2017 年 3 月 16–19 日, 横浜.
7. 谷口卓也, 杉山晴紀, 植草秀裕, 城始勇, 小島秀子, 朝日透, "キラルアゾベンゼン結晶の構造相転移による移動現象", 第 25 回有機結晶シンポジウム, O-16, 2016 年 9 月 18–19 日, 京都.
8. 谷口卓也, 城始勇, 小島秀子, 朝日透, "Enantiomeric Motion of Photomechanical Chiral Azobenzene Crystals", 日本化学会第 96 春季年会, 2E7-36, 2016 年 3 月 24–27 日, 京都.

9. 谷口卓也, 杉山晴紀, 植草秀裕, 城始勇, 小島秀子, 朝日透, "キラルアゾベンゼンの結晶相熱転移", 第 24 回有機結晶シンポジウム, O-6, 2015 年 11 月 1–3 日, 広島.
10. 谷口卓也, 藤澤珠里, 小島秀子, 朝日透, "キラルなアゾベンゼン誘導体結晶のフォトメカニカル屈曲", 日本化学会第 95 春季年会, 2A7-54, 2015 年 3 月 26–29 日, 船橋.
11. 谷口卓也, 石川和彦, 中川鉄馬, 田中真人, 朝日透, "G-HAUP 法による硫酸ニッケル 6 水和物結晶のキラル光学的性質の測定",日本化学会第 94 春季年会, 3D3-08, 2014 年 3 月 27–30 日, 名古屋.

(Domestic, Poster)

1. 谷口卓也, 杉山晴紀, 植草秀裕, 城始勇, 小島秀子, 朝日透, "キラルアゾベンゼン結晶の熱相転移と移動現象", 第 54 回熱測定討論会, P66, 2018 年 10 月 31–11 月 2 日, 横浜.
2. 萩原佑紀, 谷口卓也, 小島秀子, 朝日透, "サリチリデンアニリン結晶の光異性化と熱相転移によるメカニカルな動き", 第 27 回有機結晶シンポジウム, P-62, 2018 年 10 月 27–28 日, 大阪.
3. 谷口卓也, 佐藤寛泰, 小島秀子, 朝日透, "サリチリデンナフチルエチルアミン結晶の光トリガー相転移", 2018 年光化学討論会, 3P073, 2018 年 9 月 5–7 日, 西宮.
4. 萩原佑紀, 谷口卓也, 小島秀子, 朝日透, "Mechanical Motions of Salicylideneaniline Crystals Induced by Light and Heat", 2018 年光化学討論会, 1P086, 2018 年 9 月 5–7 日, 西宮.

5. 谷口卓也, 杉本良太, 小宮潤, 小島秀子, 朝日透, "光および熱によるサリチリデンナフチルエチルアミン結晶の形状変化", 第 26 回有機結晶シンポジウム, P-34, 2017 年 11 月 3–5 日, 米沢.
6. 谷口卓也, 内本英孝, 石橋禎大, 久保田あゆみ, 高橋浩三, 小島秀子, 朝日透, "アントリルメチレンインダノン結晶の *E-Z* 光異性化による光屈曲", 2016 年光化学討論会, 1P094, 2016 年 9 月 6–8 日, 東京.
7. 谷口卓也, 城始勇, 小島秀子, 朝日透, "キラルなアゾベンゼン誘導体結晶の光屈曲", シンポジウム モレキュラー・キラリティー 2015, PP-73A, 2015 年 6 月 12–13 日, 東京.
8. 谷口卓也, 藤沢珠里, 小島秀子, 朝日透, "キラルなアゾベンゼン結晶のフォトメカニカル機能", 2014 年光化学討論会, 1P006, 2014 年 10 月 11–13 日, 札幌.
9. 谷口卓也, 藤澤珠里, 小島秀子, 朝日透, "キラルなアゾベンゼン結晶のフォトメカニカル機能の探索", 第 23 回有機結晶シンポジウム, P-3, 2014 年 9 月 15–17 日, 船橋.
10. 谷口卓也, 石川和彦, 田中真人, 朝日透, "G-HAUP 法による硫酸ニッケル 6 水和物の光学的性質の測定", 日本化学会第 93 春季年会, 3PC-120, 2013 年 3 月 22–25 日, 草津.

Others

（解説）

1. 小島秀子, 谷口卓也, 朝日透, "解説：世界初！歩き回るロボット結晶が誕生––まったく新しいソフトロボット実現への可能性", 化学（化学同人）, 2018 年 9 月号.

（特許）

1. 特願 2017-501544, 「光駆動装置」, 池滝慶記, 小島秀子, 朝日透, 高鍋彰文, 谷口卓也.

（受賞）

1. Poster Presentation Award, Takuya Taniguchi, Haruki Sugiyama, Hidehiro Uekusa, Motoo Shiro, Hideko Koshima, Toru Asahi, "Directional Locomotion of Chiral Azobenzene Crystals", 29th International Symposium on Chirality (Chirality 2017), P-012, 9–12 July 2017, Tokyo, Japan.
2. Poster Prize, Takuya Taniguchi, Haruki Sugiyama, Hidehiro Uekusa, Motoo Shiro, Hideko Koshima, Toru Asahi, "Directional Locomotion of Chiral Azobenzene Crystals by Phase Transition", The 23rd International Conference on the Chemistry of the Organic Solid State (ICCOSS XXIII), P-53, 2–7 April 2017, Stellenbosch, South Africa.
3. 優秀講演賞, 谷口卓也, 杉山晴紀, 植草秀裕, 城始勇, 小島秀子, 朝日透, "キラルアゾベンゼン結晶の構造相転移による移動現象", 第 25 回有機結晶シンポジウム, O-16, 2016 年 9 月 18–19 日, 京都.
4. Outstanding Poster Presentation Award, Takuya Taniguchi, Juri Fujisawa, Hideko Koshima, Toru Asahi, “Photomechanical Bending of Chiral and Racemic Azobenzene Crystals”, The 22nd International Conference on the Chemistry of the Organic Solid State (ICCOSS XXII), P27, 12–17 July 2015, Niigata, Japan.

5. ポスター賞, 谷口卓也, 城始勇, 小島秀子, 朝日透, "キラルなアゾベンゼン誘導体結晶の光屈曲", シンポジウム モレキュラー・キラリティー 2015, PP-73A, 2015 年 6 月 12–13 日, 東京.